Precise intensity monitoring at CRYRING@ESR: On designing a Cryogenic Current Comparator for FAIR

D I S S E R T A T I O N

zur Erlangung des Doktorgrades
der Naturwissenschaften

vorgelegt beim Fachbereich Physik
der Johann Wolfgang Goethe-Universität
in Frankfurt am Main

von

David Haider
aus Linz (Österreich)

Frankfurt am Main, 2023
(D 30)

vom Fachbereich Physik der
Johann Wolfgang Goethe-Universität als Dissertation angenommen.
Datum der Disputation: 3. 7. 2023

Dekan:
Prof. Dr. Roger Erb

Gutachter:
PD Dr. Peter Hülsmann
Prof. Dr. Holger Podlech

Abstract

In the field of today's beam intensity diagnostic there is a significant gap in the non-interceptive, calibrated measurement of the absolute intensity of continuous (unbunched) dc beams with current amplitudes below 1 µA. At the Facility for Antiproton and Ion Research (FAIR) low-intensity DC beams will occur during slow extraction from the synchrotrons as well as for coasting beams of highly-charged or exotic nuclei in the storage rings. The lack of adequate beam instrumentation limits the experimental program as well as the accuracy of experimental results.

The Cryogenic Current Comparator (CCC) can close the diagnostic gap with a high-precision dc current reading independent of ion-species and of beam parameters. However, the established detector design based on a core with high magnetic permeability and on a radial shield geometry has well-known weaknesses concerning magnetic shielding efficiency and intrinsic current noise. To eliminate these weaknesses, a novel coreless CCC with a co-axial shield was constructed and combined with a high-performance SQUID contributed by the Leibniz-Institute of Photonic Technology (Leibniz-IPHT Jena). The new axial CCC model was compared to a radial CCC with the established design provided by the Friedrich-Schiller-University Jena. According to numerical simulations prepared at TU Darmstadt and test measurements of the detectors in the laboratory, the new design offered a significant improvement of the shielding factor – from 75 dB to 207 dB at the required dimensions – and eliminated all noise contributions from the core material, promising an improved current resolution. Although the lower inductance of the pickup coil reduced the coupling to the beam significantly, the noise properties of the new CCC type were comparable to the classical version with a high-permeability core. However, the expected decrease of the low-frequency noise and thus an increase of the current resolution could not be observed at this stage of development.

Consequently, the classical CCC based on the radial shielding and high-permeability core had to be installed in CRYRING@ESR to provide best possible intensity measurements for the upcoming experimental campaign. In CRYRING the CCC was operated with beam currents between 1 nA and 20 µA and with different ion species (H, Ne, O, Pb, U). It was shown that the CCC provides

a noise-limited current resolution of better than $3.2\,\mathrm{nA_{rms}}$ at a bandwidth of 200 kHz as well as a noise level below $40\,\mathrm{pA}/\sqrt{\mathrm{Hz}}$ above 1 kHz. During the operation, the main noise sources of the accelerator environment had to be identified and suitable mitigation strategies were developed. Temperature and pressure fluctuations were suppressed with a newly-designed cryogenic support system based on a 70 l helium bath cryostat, developed and built in collaboration with the Institut für Luft- und Kältetechnik Dresden, in combination with a helium re-liquefier. The cryogenic operating time was restricted to around 7 days, which must be expanded significantly in the future. Digital filters were developed to remove the perturbations of the helium liquefier and of the neighboring dipole magnets. Given the promising results the CCC system can be considered as a prototype for future CCCs at FAIR.

Kurzfassung

Die Facility for Antiproton and Ion Research (FAIR) ist das Zukunftsprojekt und die Erweiterung der bestehenden Beschleunigeranlage der GSI, dem Helmholtzzentrum für Schwerionenforschung in Darmstadt. Für das experimentelle Programm bei FAIR kommen Teilchenströme unterschiedlicher Ionenspezies und Zeitstruktur zur Anwendung. Neben kurz gepulsten, schnell aus den Synchrotronen extrahierten Strahlen hoher Intensität spielen für zahlreiche Experimente (mit kontinuierlicher Detektion am Target) langsam extrahierte Strahlen mit der damit einhergehenden niedrigen Intensität eine wichtige Rolle. Ebenso liegen im Bereich der hochgeladenen und exotischen Ionen in den Speicherringen kontinuierliche Strahlen niedriger Intensität vor. Eine genaue Kenntnis der Strahlintensität ist von elementarer Wichtigkeit für die Bestimmung von Reaktionsraten und Wirkungsquerschnitten. Unter einer Schwelle von rund 1 µA stößt die heute verfügbare Strahldiagnose bei der zerstörungsfreien, kalibrierten Messung der absoluten Strahlintensität an ihre Grenzen.

Der Einsatz eines kryogenen Stromkomparators (Cryogenic Current Comparator – CCC) verspricht hier eine signifikante Verbesserung der Messgenauigkeit. Im Rahmen dieser Arbeit wurde ein CCC Intensitätsmonitor am Schwerionen-Speicherring CRYRING@ESR bei FAIR installiert und bei kleinen Strömen (1 nA – 20 µA) für eine Vielzahl von Ionensorten (H, Ne, O, Pb, U) mit gängigen Strahldiagnose-Instrumenten verglichen. Mit einer rauschlimitierten Auflösung von 3,2 $\mathrm{nA_{rms}}$ bei einer Bandbreite von 200 kHz konnte der CCC in vielen Anwendungsfällen die verfügbare Messgenauigkeit um drei Größenordnungen verbessern. Dabei lag das Rauschniveau des CCCs bei Frequenzen über 1 kHz unter einer Schwelle von $40\,\mathrm{pA}/\sqrt{\mathrm{Hz}}$.

Für die Anwendung am CRYRING@ESR stellte die Friedrich-Schiller-Universität Jena einen radialen CCC zur Verfügung. Die Stromauflösung dieses etablierte Detektor-Designs mit einem radial aufgebauten magnetischen Schirm und einem magnetisch hochpermeablen Kern ist jedoch durch externe Störeinflüsse und durch das niederfrequente Stromrauschen des Kerns beschränkt. Daher wurde ein neuartiger kernloser CCC-Prototyp mit einer koaxialen Schirmgeometrie konstruiert und mit einem hochpräzisen SQUID des Leibniz-Institut für Photonische Technologien (Leibniz-IPHT Jena) verbunden.

Es konnte sowohl anhand von Simulationen der TU Darmstadt als auch bei der Vermessung im Labor gezeigt werden, dass für die geforderten Dimensionen die neue Geometrie den Abschirmfaktor von 75 dB auf 207 dB steigert. Obwohl die Induktivität der Messspule und somit die Kopplung zum Ionenstrahl durch den fehlenden Kern stark reduziert ist, wurde ein ebenso niedriges effektives Rauschniveau erreicht. Der erwartete Rückgang des niederfrequenten Rauschens und die damit einhergehende höhere effektive Stromauflösung konnten bisher jedoch nicht bestätigt werden. Aufgrund der geringfügig besseren Messgenauigkeit im Labor wurde schließlich der etablierte CCC mit Kern und klassischer radialer Schirmgeometrie für die Messungen am CRYRING@ESR eingesetzt.

Beim Betrieb des CCCs am CRYRING@ESR sorgte eine neue kryogene Messplattform für eine stabile Messumgebung. Diese basierte auf einem 70 l Heliumbad-Kyrostat, der vom Institut für Luft- und Kältetechnik Dresden nach den Vorgaben von GSI gebaut wurde und mit einem lokalen Helium-Verflüssiger verbunden war. Verbliebene Störeinflüsse durch den Helium-Verflüssiger und durch den benachbarten Dipol-Magnet wurden durch digitale Filterroutinen beseitigt. Nach der erfolgreichen Messkampagne steht das Detektor-System nun als Grundlage für den nächsten Schritt zur Serienproduktion des CCC bei FAIR zur Verfügung.

Acknowledgment

Throughout my studies I have had the support of many encouraging people. They have made my time at the GSI research campus a wonderful period of my life and without them it would not have been possible for me to complete this thesis in the form it has today. In the following, I would like to say thank you to all who have accompanied me on my way and highlight those who made it a particular effort to help me finish this work.

First of them all are my wonderful girlfriend and my loving parents and with their endless support for my studies. They guided me when I had doubts and gave me the energy to keep going.

Furthermore, I would like to thank my academic supervisor at University Frankfurt Peter Hülsmann – who is enthusiastic about my project every time I meet with him and who can truly share my ambivalent relationship towards unruly ceramic insulator gaps – for his encouraging attitude and support.

In addition, I want to thank , who was my day-to-day supervisor within the Beam Diagnostics Group at GSI, for all the invaluable inputs on the problems that I encountered and for his enthusiasm when there is things to solve in the lab. He made an effort to read though many versions of this thesis and helped me to improve it with an inexhaustible amount of suggestions. Moreover, I am deeply grateful for the company of my fellow PhD students who made sure that the lunch breaks were a highlight of the day and who were there to assure that attempting to obtain a PhD was truly the right decision.

During my studies I was constantly in touch with the colleagues of the CCC collaboration and it was a pleasure to be part of this supportive and welcoming community. Among them I am highly appreciative of
at Leibniz-IPHT Jena who always makes my day with his kindness and his gen-

erosity and who made it a particular effort to share his knowledge when it came to building a new CCC. Moreover, I am thankful of – the head of the department of Quantum Systems at Leibniz-IPHT – for his honest and extraordinarily helpful feedback and practical approach to get things done. Last but not least among the CCC collaboration I am grateful for all the help and practical advice from at Helmholtz-Institute Jena who repeatedly offered his time and his lab to perform measurements and who prepared the detector that I could use for the measurement campaign at CRYRING.

Furthermore, for all the help in the laboratory and during the installation and operation at CRYRING I owe a big thank-you to the most patient precision mechanics I know, and , and to the great team at CRYRING, in particular , , , , and .

Finally, I would like to express my gratitude to and , the head of Beam Diagnostics and the head of its Research Section, as well as to , the mind that created the EU Innovative Training Program (Accelerators Validating Antimatter) which funded the majority of my PhD. They enabled me to work on this exciting project connected to FAIR which will be a hotspot for accelerator physics and who always make sure that the institute is a great place for young students to thrive.

Contents

Introduction **1**

1 Limitations of beam intensity diagnostics **7**

1.1 Bunched beam 8

1.1.1 Integrating AC Current Transformer 9

1.1.2 Capacitive Measurement (Beam Position Monitors & CryRadio) 10

1.1.3 Faraday Cup 13

1.2 Coasting beam 14

1.2.1 Parametric DC Current Transformer 14

1.2.2 Ionization Profile Monitor 17

1.2.3 Schottky monitor 18

1.3 Prospects of the CCC 20

2 Theory of SQUID magnetometry **23**

2.1 Superconductivity 24

2.2 The Josephson Junction 26

2.3 The dc SQUID: Theory and Readout 29

2.3.1 SQUID electronics and FLL mode 32

2.3.2 SQUID radiation hardness 37

3 The Cryogenic Current Comparator **41**

3.1 A CCC for beam intensity monitoring 42

3.2 Superconducting flux transformer 45

3.3 Topology of the superconducting shield 48

3.4 The high-permeability core 50

4 Evaluation of CCC detector systems **55**
4.1 Shield performance . . . 56
4.2 CCC test bench . . . 58
4.3 Radial topology . . . 60
4.3.1 Construction and design . . . 60
4.3.2 SQUID parameter . . . 64
4.3.3 Shielding factor . . . 68
4.3.4 Noise current spectral density . . . 68
4.4 Axial coreless topology . . . 70
4.4.1 Construction and design . . . 72
4.4.2 SQUID parameter . . . 76
4.4.3 Shielding factor . . . 79
4.4.4 Noise current spectral density . . . 80
4.5 Comparison of detector types . . . 82

5 Cryogenic support system **87**
5.1 General design aspects . . . 87
5.2 Design study . . . 88
5.2.1 Mechanical design . . . 92
5.2.2 Insulator gap – beam tubes . . . 95
5.2.3 Cryogenic design . . . 97
5.3 Cryogenic operating performance . . . 101
5.3.1 Helium re-liquefier and self-sufficient operation . . . 101
5.3.2 System stability . . . 104
5.3.3 Perturbation by the beam-line . . . 107

6 The CCC at CRYRING@ESR **109**
6.1 CRYRING@ESR . . . 109
6.2 Experimental setup . . . 110
6.2.1 Data acquisition . . . 112
6.2.2 Calibration source . . . 114
6.2.3 CCC calibration . . . 115
6.2.4 Signal background . . . 117
6.3 Operating environment . . . 119

6.3.1 SQUID performance deterioration 119
6.3.2 Dipole perturbation 121
6.3.3 Noise current spectral density 122
6.3.4 Liquefier perturbation 123
6.4 Intensity measurement with beam 125
6.4.1 Boundary conditions 125
6.4.2 Full bandwidth measurements 126
6.4.3 Small current amplitudes 129
6.4.4 Limitations at large current amplitudes 130
6.4.5 System adaptation 133
6.5 Comparison with standard diagnostics 136
6.5.1 Coasting beam (PCT and IPM) 136
6.5.2 Bunched beam (ICT and BPMs) 139
6.5.3 Schottky measurement 141
6.6 Lifetime measurement 142

Summary and Outlook **145**

Appendix **157**

Introduction

The Cryogenic Current Comparator (CCC) was first documented and used by I. K. Harvey in 1972 as a means to compare electric currents with high precision [1]. Even today it is still used in metrological institutes around the globe to check currents against an international standard with a current resolution of $1\,\mathrm{fA}/\sqrt{\mathrm{Hz}}$ or better [2]. Since then, for accelerator facilities the prospect of a non-destructive diagnostic device that extends the low-intensity detection threshold of standard Beam Current Transformers has been very attractive. Like the Current Transformer, the CCC purely relies on the detection of the magnetic field created by moving electric charges rather than on other secondary, beam-dependent parameters and thus can easily be linked to metrological current standards. An extension of the measurement range is especially important for exotic (e.g. radioactive) low-intensity ion beams stored as a continuous coasting beams in storage rings and during slow extraction, where there exists no suited diagnostics solution.

Soon after the invention of the CCC in 1977, first studies in this research field proved the feasibility of this goal and proposed a topology for a superconducting shield which can solve the main challenge, which lies in the highly selective observation of the magnetic field of the ion beam while strongly attenuating all external electromagnetic perturbations [3, 4]. Some years later, in the 1990s, at the Helmholtz Centre for Heavy Ion Research (GSI) (Germany) and at the Institute for Nuclear Study (INS) (Japan) the idea was picked up and the first promising results operating a CCC as a beam diagnostic device at a beam line and at a storage ring were collected [5, 6]. However, the high manufacturing and operating costs connected to a cryogenic device as well as the significant limitation of the current resolution by perturbations due to electromagnetic

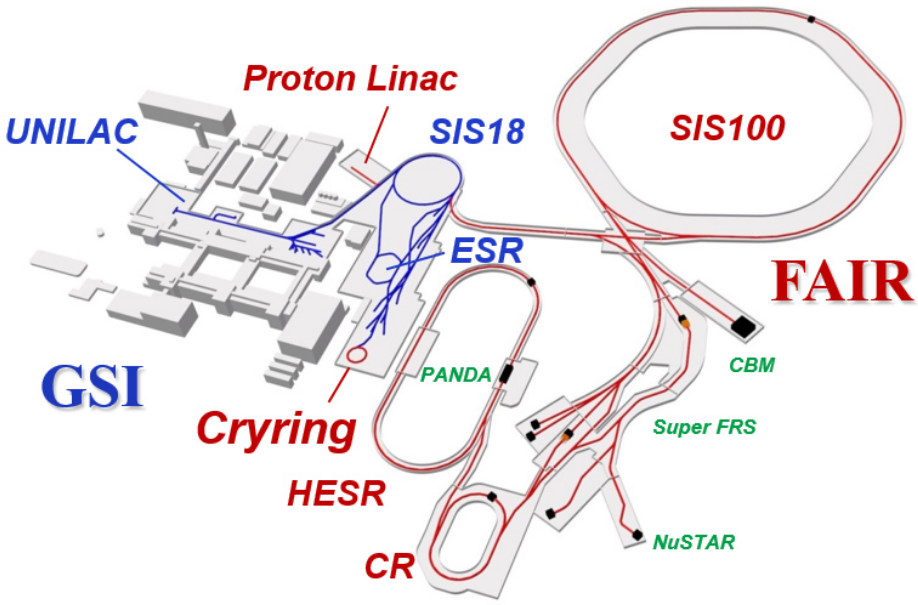

Figure 1: *Overview of the accelerator complex at GSI (blue), of the new facilities that constitute FAIR (red) and of the major experiments (green).*

interference, temperature/pressure fluctuations and mechanical vibrations prevented a wider success.

With the goal to mitigate these perturbations by a careful design of the cryostat and taking advantage of the development of small-sized helium re-liquefiers, which allows to significantly extend the cryogenic operating time from a few hours to several months, a CCC was installed at the Antiproton Decelerator (AD) at CERN in 2016 [7, 8]. While not completely eliminating all perturbations, in this installation temperature and pressure effects were reduced significantly and it has been used during the AD operation to monitor the beam current with an improved accuracy compared to the existing diagnostics based on Schottky measurements.

In contrast to the very rigid use-case of antiprotons at the AD, the upcoming Facility for Antiproton and Ion Research (FAIR) [9] (see Fig. 1) features a wide variety of ion species from hydrogen up to uranium with constantly changing beam parameters. This makes the absolute measurement of low-intensity dc beams with the available beam diagnostics even more difficult. Therefore, several CCC systems are planned to be installed at FAIR.

This PhD project started with the aim to prepare the installation of these CCC systems throughout transfer lines and storage rings at FAIR and to adapt the detector system to the specific requirements (e.g. increased beam-line diameter, expected beam parameter) at the FAIR facility. Moreover, the available noise-limited current resolution should be improved compared to previous systems. While the basic principle of the CCC detector remained very static throughout the years, for the installation at FAIR a new detector concept was explored [10]. It is based on a different topology of the magnetic shield which is part of the CCC to strongly attenuate all magnetic field components that are not symmetric around the axis of the detector, which is identical to the axis of the local beam-line. The new shield geometry [11] will allow for a much larger attenuation factor at the detector dimensions required for FAIR.

Furthermore, the increased shielding factor opens the possibility to omit the highly permeable core of the CCC. Typically, CCCs are equipped with a core in order to couple the beam current to a detector system with high efficiency. However, the integration of a high-permeability core has two disadvantages: It limits the bandwidth of the circuit and it introduces a significant amount of low-frequency noise (so-called colored noise) [12]. However, one of the main performance parameters of the CCC is the intrinsic current noise which determines the minimum amplitude of the beam current that can be resolved. In order to expand the low-intensity detection limit, in this work a coreless CCC [10] was investigated. The challenge of a coreless design is to adapt the detection system to the significantly smaller inductance (and signal) of the pick-up coil without increasing the susceptibility to other noise sources and without deteriorating the stability of the detector.

Of great importance for an increased current resolution of the CCC is the reduction of the effect of the perturbations from the accelerator environment. Temperature and pressure fluctuations as well as mechanical vibrations translate directly to a noisy signal in the CCC measurement. For the operation at the beam-lines a versatile cryogenic support system was designed with the goal to have a very stable operating environment. Out of the two competing CCC models, the detector with the better noise performance was installed at the heavy-ion storage ring CRYRING@ESR to be tested with beam.

FAIR uses the GSI accelerator chain as an injector (cf. Fig. 1). At GSI there exists a wide portfolio of fixed target or in-ring experiments in different areas (biophysics, plasma physics, atomic physics, etc.), which take advantage of the wide variety of different ion species and beam energies. The primary goal of FAIR is to increase the available ion currents which results in much better statistics for the experiments and allows observation of rare secondary (e.g. radioactive) beams. The GSI facility consists of the linear accelerator UNILAC (combination of IH and Alvarez acceleration structure) that reaches ion energies up to 30 MeV/u and supplies the heavy-ion synchrotron SIS18 with elements up to uranium. The maximum extraction energy for protons from SIS18 is 4.5 GeV/u. After the extraction from SIS, for nuclear physics experiments heavy ions are transported to the Fragment Separator (FRS) where short-lived, radioactive secondary beams are produced via collisions with a thin beryllium target. These beams can then be stored at the Experimental Storagre Ring (ESR) (4 MeV to 500 MeV) with excellent beam properties due to stochastic and electron cooling. Alternatively, the cooled ions can be decelerated and delivered to experiments or to CRYRING@ESR for further manipulations and in-ring experiments. CRYRING operates with beam intensities between several nA and 20 µA and with various different ion species [13]. Therefore, it offers the possibility to test the CCC with beam conditions that are very close to the conditions that are expected with low-intensity beams at FAIR.

In the **first chapter** the limitations of standard beam instrumentation are discussed in order to derive the role that the Cryogenic Current Comparator can play in this research field. **Chapter two** gives a theoretical foundation of superconductivity and introduces the concept of the Superconducting Quantum Interference Device (SQUID) which is the detector on which the CCC is based. Furthermore, in **chapter three** there is a description of a 'classic' CCC system [3] that, in **chapter four**, is compared based on laboratory measurements to a newly-developed CCC system with significant differences concerning the magnetic shield, the pick-up inductance, the SQUID parameter and the construction material that all affect the ultimate measurement performance. **Chapter five** deals with the design and performance of the cryogenic support system. Finally, the experimental results of the operation of the CCC system in the heavy-ion

storage ring CRYRING@ESR are presented in **chapter six** while a concluding summary closes this thesis in **chapter seven**.

Chapter 1

Limitations of beam intensity diagnostics

Beam instrumentation plays a vital role for a successful high-performance operation of accelerators, storage rings and transport sections and thus directly determines the quality of experimental results. This is particularly true for beam intensity monitoring since the beam intensity is used to calculate branching ratios and interaction cross-sections. Different types of intensity diagnostics are employed depending on the beam parameters and on the experimental requirements. While there exist many diverse detector configurations for different beam parameters and intensities, within the scope of this thesis the main focus is on instruments which can provide a current reading when beam intensities are rather low ($\ll 20\,\mu A$). Within the Facility for Antiproton and Ion Research (FAIR) such low beam currents will be common in transfer lines during slow extraction from SIS18 and SIS100 or with exotic beams in low-energy storage rings like CRYRING@ESR.

With the beam instrumentation available today, for many beam conditions the accurate non-destructive monitoring of these low beam intensities will be extremely challenging if not impossible. This is especially true for unbunched (coasting) beam that is routinely requested by experiments and for which there is no single standard beam diagnostic device which can provide a calibrated current measurement. The Cryogenic Current Comparator is designed to fill this gap in the intensity diagnostic and provide calibrated current data down to an absolute intensity of several nA.

In order to illustrate the superior properties and characteristics of the CCC, this chapter contains an overview of the standard intensity diagnostics and highlights the areas in which the CCC can overcome the limitations of the existing instrumentation in a storage ring, based on the broad variety of diagnostics devices at the heavy-ion storage ring CRYRING@ESR. Most of these devices can be found in every large accelerator facility so that the following description of their qualities and weaknesses gives a good overview of today's standard in the field of low-intensity diagnostics, particularly of hadron machines. The advantages of the application of the CCC in beam transfer lines is discussed in more detail in [14].

The amplitude of the ion currents in CRYRING@ESR typically ranges from several nA to 20 µA with beam energies between several tens of keV/u and 24 MeV/u. With the expectation of low beam intensities, particular attention was given to the intensity diagnostics during the design of the storage ring. The instruments which are used for intensity measurement and which are permanently installed in CRYRING are an Integrating AC Current Transformer (ICT), Beam Profile Monitors (BPM), Faraday Cups (FC), a Parametric Current DC Transformer (PCT), an Ionization Profile Monitor (IPM) and a Schottky pick-up [15]. In Table 1.1 basic properties of these devices are summarized.

1.1 Bunched beam

For the intensity measurement of bunched beam there are instruments that can achieve an excellent current resolution down to nA and below. The circulating bunches form a constantly fluctuating beam current which induces a signal in the inductive pick-up loop of the ICT or interacts with the free charge carriers in the capacitive pick-ups of the BPM. The FC collects the charge of the beam and can be used for both bunched and unbunched beam. However, at CRYRING it is only used as a first-turn diagnostics to optimize the injection of the bunched ions to the storage ring during the beam commissioning.

1.1.1 Integrating AC Current Transformer

Beam Current Transformers are a non-destructive family of intensity measurements that are based on the operating principle of electric transformers. In the beam transformer the ion current takes the role of the primary current I_{prim} that creates a change of the magnetic flux which induces a secondary current I_{sec} in a winding around a ring core with a high magnetic permeability that encloses the beam-line (see Figure 1.1). The secondary current or voltage is detected and is directly related to the original beam current.

The ICT from BERGOZ Instrumentation[1] at CRYRING can be used to quantify bunched beam currents down to 10 nA with averaging of multiple cycles. Since beam transformers rely only on the magnetic field created by the moving charges, they are independent of other beam parameters (e.g. ion species) and they can be calibrated with electric test currents to provide a calibrated current measurement. The bunch shape processing (BSP) to determine the zero-current baseline (see Sec. 1.1.2) limits the usable bandwidth to 100 Hz. The current noise of the ICT system can ideally be as low as $1\,\mathrm{nA_{rms}}$ at a bandwidth of 20 Hz [16]. Furthermore, the deviation from a linear response at current amplitudes of 10 nA or higher is better than 1.6 %, while the calibration error increases to 4 % at currents of 1 nA [17].

At CRYRING the measurement of the ICT is limited to the flat top after the acceleration when there is a constant revolution frequency of the bunches since there is no automatic routine to reliably match the integration window of the bunch shape processor to the changing phase of the current signal as the revolution frequency is increased [18]. At a constant revolution frequency the phase difference between the gate signal, that determines the integration window around the bunches, and the signal from the ICT is static and thus can be set manually to a fixed optimal value. Note that the manual configuration of the integration gate is a potential source of error.

Since the ICT requires bunched beam, it can provide no current data once the beam is de-bunched. However, for bunched beam (e.g. during the acceleration) the ICT provides the most precise calibrated current measurement at CRYRING (besides the CCC) and is used as a reference to calibrate other instrumentation.

[1] BERGOZ Instrumentation, 01630 Saint Genis Pouilly, France

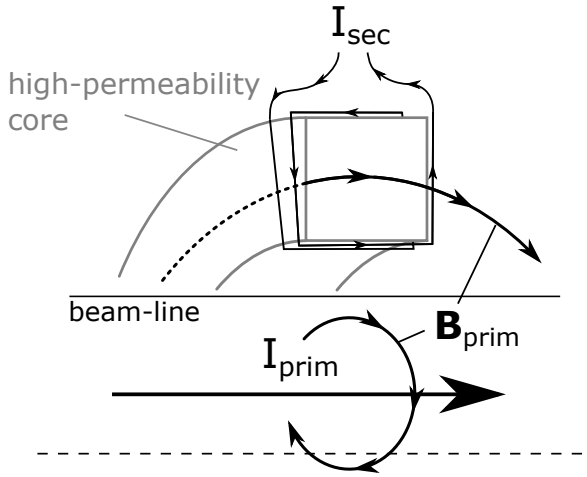

Figure 1.1: *Schematic of the measurement principle of the AC Current Transformer and the Integrating Current Transformer (ICT).*

This can be the detectors of the experiments themselves, dedicated neutral particle detectors which monitor the beam-loss at a dipole magnet or the signal from other beam instrumentation like the Schottky monitor or the IPM. After the initial acceleration, when the beam intensity (e.g. of a coasting beam) decreases, the beam loss that is detected in the detectors declines as well and an estimate of the stored ions can be given for the remainder of the cycle.

1.1.2 Capacitive Measurement (Beam Position Monitors & CryRadio)

The most precise current reading for bunched beams at CRYRING can be achieved with the BPM system. The BPMs consist of four electrically isolated wall-electrodes that follow the shape of the beam-tube. When an electric charge passes a BPM, its electric field attracts or repels the free charge carriers in the metal of the electrodes. Therefore, each change of the beam current produces a mirror current within the electrode and in the connected wires. The coherent signal of all charges in a bunched beam is proportional to the number of particles N. Since many different factors affect the amplitude of the extracted signal, capacitive measurements can only provide a relative current monitoring. In order to determine absolute beam currents, they need to be calibrated with an absolute current sensor (e.g. CCC or ICT).

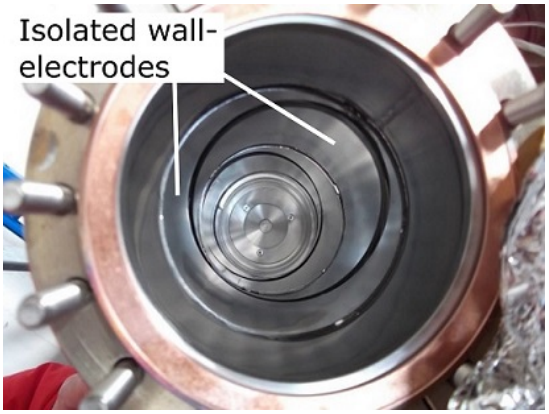

Figure 1.2: *Photo of the BPM installed at CRYRING. Courtesy of A. Reiter [18].*

At CRYRING there are a total of 9 BPMs with segmented wall-electrodes, each with two vertical and horizontal electrodes (see Figure 1.2). Typically, the difference in the signal of opposing electrodes is used to determine the beam position. However, to measure the beam current, the BPM sum signal is used. The main challenge to obtain an accurate measurement is to isolate the signal – which is proportional to the charge carried by the bunches – from the varying baseline throughout the acceleration cycle. One approach to determine the baseline is to create an adaptive integration gate that is linked to the acceleration frequency, with a duty cycle of 33.3 % and which is centered at the time between individual bunches [16]. In this way, only the baseline is extracted and can be subtracted from the overall signal. The technical implementation is not trivial and the phase of the integration window has to be fine tuned after each change of the operating parameter to achieve the maximum signal accuracy. However, this broadband measurement has the advantage that it is very robust against changes of the longitudinal beam profile (e.g. during beam cooling). Still, the output signal of the BPMs depends on the beam velocity β, which makes the monitoring of low-energetic beams more difficult. The ICT uses the identical readout scheme that requires a manual adjustment of the integration window. With this approach the current noise of the BPM current signal can be reduced to 100 pA_{rms} at a revolution frequency between 40 kHz to 1.5 MHz [15, 16]. The measurement is calibrated with the ICT to obtain an absolute scale.

A more refined approach, the so-called *CryRadio* [15, 18], is to transfer the relevant frequencies – that are associated with the charge of the beam – to

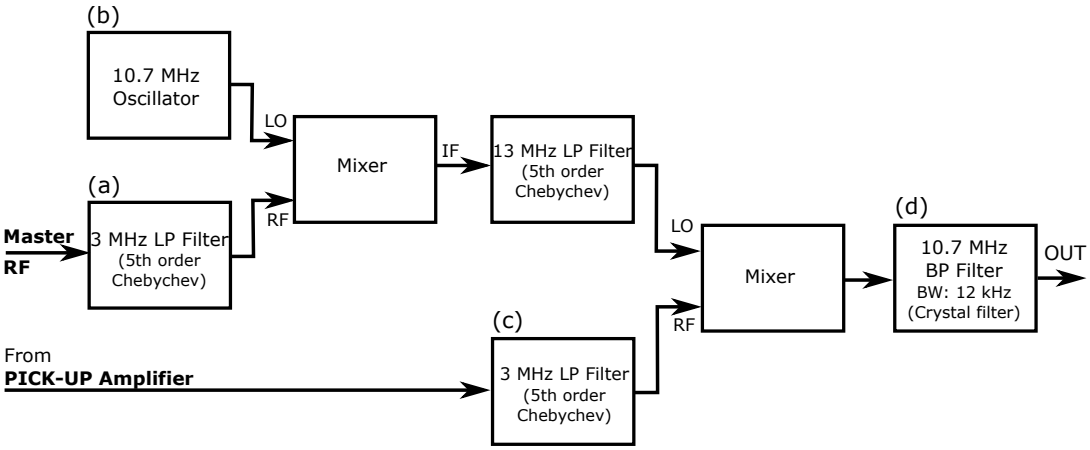

Figure 1.3: *Schematic of the CryRadio BPM intensity measurement system [17].*

a separate frequency range where they can be analyzed more easily using the super-heterodyne principle (see Figure 1.3). A first mixer creates the combination of the master frequency (a) that dictates the bunching by the HF cavity (e.g. 1.5 MHz) and an arbitrary frequency (b) that can easily be produced, in this case 10.7 MHz. A second mixer uses this output and combines it with the signal from the capacitive pick-up (c) which consists of the revolution frequency (f_{rev}) of the beam (e.g. 1.5 MHz) plus a frequency-band around the revolution frequency that describes the properties of the bunch. In a last step, only this frequency-band – located around 10.7 MHz after the second mixer – is extracted with a band-pass filter (d) with a pass band width of $\Delta f_{pass} = 12\,\mathrm{kHz}$. The amplitude of the resulting sine-wave is now proportional to the beam current. Without the low-frequency components, this signal has no baseline offset and with a constant frequency independent of the revolution frequency the integration is straight forward. For an easy readout, a demodulator paired with a logarithmic amplifier gives the beam intensity. This approach offers the most sensitive (relative) current resolution for bunched beams. However, it is more susceptible to be influenced by changes of the longitudinal beam profile (bunch shapes) as they occur during the operation of the electron cooler. The bandwidth is limited by the signal modulation at the frequency of 10.7 MHz and by a subsequent signal filter.

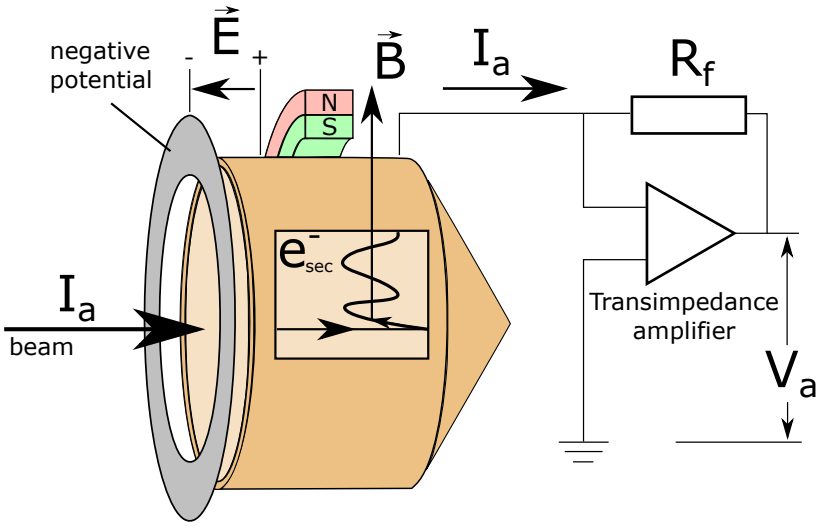

Figure 1.4: *Schematic of a Faraday Cup for hadron machines.*

1.1.3 Faraday Cup

The Faraday Cup is a fully destructive but very precise intensity diagnostic with a wide operating range from 10 pA up to 10 mA or higher [19]. It consists of a cup of an electrical conductor (typically copper in hadron machines) which is inserted into the beam-line (see Figure 1.4). The ions are collected in the material and the deposited electric charge is measured. Since it detects the charge of the ion beam, it is independent of other beam parameter like the ion species, the beam energy or the beam bunching. However, when the deposited energy is high enough to heat the material, an active cooling mechanism is required.

Furthermore, an electric potential $\vec{E}$ at the entrance of the cup prevents charged secondary electrons – created by the impact of the ions – from escaping and, in this way, ensures that the charge of the beam is measured correctly. Additionally, a magnetic field $\vec{B}$ created by a permanent magnet sends the secondary electrons on a spiraling path and stops them from leaving the cup. For the readout the current signal is processed with a current-to-voltage converter (e.g. a transimpedance amplifier). Faraday Cups are primarily used with medium and low beam energies below 100 MeV/u where the ions are stopped inside the material of the cup within less then 1 cm.

At CRYRING there are three Faraday Cups which are routinely used as a first-turn diagnostics with a bandwidth of 100 MHz [18]. Once the beam is stored in

the ring, Faraday Cups cannot be used since they would immediately stop and destroy the circulating beam.

1.2 Coasting beam

For intensity monitoring of weak unbunched ion beam in transfer lines or in storage rings the available options are more limited. In general, the workhorse for calibrated dc current measurement is the DC Current Transformer (also called PCT). However it is limited by intrinsic noise and can only provide good results for ion currents that are larger than 10 µA. In case the beam intensity is lower, at CRYRING an IPM detects the interaction products of the beam with the residual gas in the vacuum of the beam-line and gives an uncalibrated current reading. Furthermore, a Schottky monitor can be used to extract an uncalibrated current signal from the spectral power density of the bunched and, more interestingly, of the coasting ion beam. Currently, for low-energy ions the Schottky measurement is the only established beam diagnostics at low intensities. The lack of a calibrated non-destructive current measurement of unbunched beams with a high precision at low intensities is a strong limitation that can be solved by the Cryogenic Current Comparator.

For the use in transfer lines – where the ions pass through only once (e.g. during slow extraction) – there exist several other instruments that are not discussed in detail in this thesis, but they all have their own limitations (e.g. Secondary Electron Monitor, Ionization chamber). Most notably the majority of them are at least partially destructive devices. For a more detailed discussion of the application of a CCC in transfer lines refer to [14].

1.2.1 Parametric DC Current Transformer

In principle, beam current transformers as described above can only detect changes of the beam current since they rely on electromagnetic induction. However this limitation can be overcome with the DC Current Transformer [19]. For this purpose, the secondary winding is wrapped around two transformer cores which are both driven periodically into magnetic saturation (e.g. at 1 kHz) (see Fig. 1.5). This periodic saturation is created by the oscillating current I_{mod}

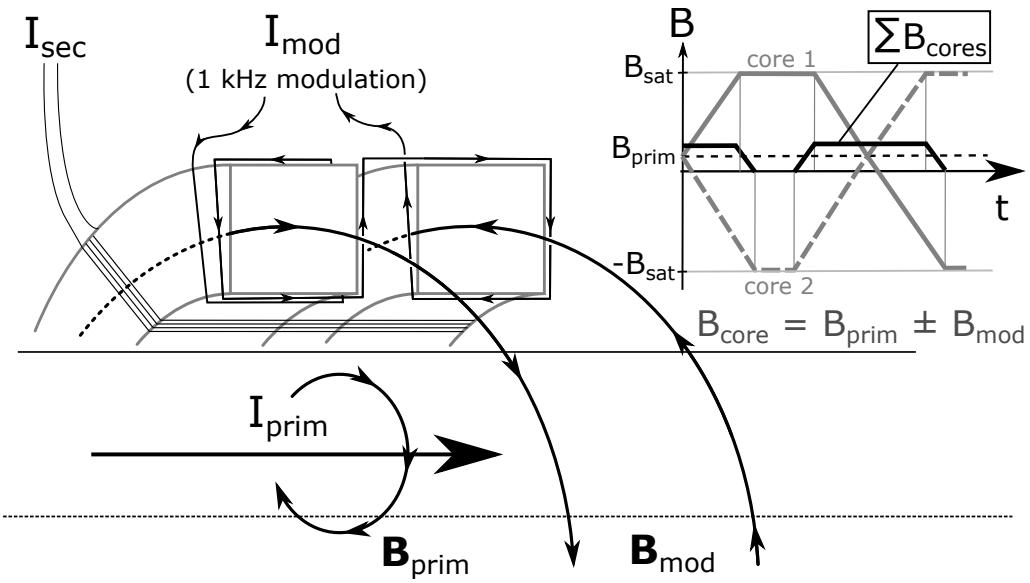

Figure 1.5: *Schematic of the measurement principle of the DC Current Transformer (DCCT) and the Parametric Current Transformer (PCT).*

through an additional *modulation* winding which is placed around the two cores in opposite rotations. Thus, the effective current I_{sec} that is induced in the secondary winding due to the modulation is zero.

However, whenever there is a constant primary current I_{prim} that is non-zero, its magnetic field B_{prim} is added to the modulation field. As a result, the cores are closer to the positive saturation limit $|B_{sat}|$. On the contrary, a larger modulation field B_{mod} is required to drive the cores to the negative saturation limit $(-|B_{sat}|)$. As a consequence, during the periodic modulation always the core with the positive modulation current is driven into saturation earlier and an effective magnetic field ($\sum_i B_{i,cores} \neq 0$) is created. The change of this field induces a voltage in the secondary winding with the frequency of the modulation that is directly proportional to the (constant) primary dc current.

A PCT from BERGOZ Instrumentation is installed at CRYRING and reasonably can be used to obtain a calibrated current signal down to a dc beam current of 10 µA with an analog bandwidth of up to 20 kHz [18]. At CRYRING a low-pass filter with a cut-off around 100 Hz is used. When multiple accelerator cycles are averaged, some information can be collected for intensities down to 1 µA. At these low currents, a two-layered high-permeability metal shield and an active

compensation of surrounding magnetic fields is necessary to reduce the effect of magnetic perturbations from the neighboring electromagnetic elements. In general, the low current range of Beam Current Transformers is limited by the following effects [19]:

- **Johnson-Nyquist (thermal) noise** - The load resistor R_l that is used to read the voltage signal with a bandwidth of Δf at the temperature T has an effective Nyquist voltage noise U_{rms} with a spectral voltage noise density of

$$S_{\text{Johnson-Nyquist}} = \frac{U_{\text{rms}}}{\sqrt{\Delta f}} = \sqrt{4\,k_B T\ R_l}\ . \tag{1.1}$$

  At room temperature and for low current measurements the bandwidth Δf has to be reduced to decrease the amount of noise that affects the measurement. Even then the remaining thermal noise limits the current resolution.

- **Permeability of the core** - Typically a material with a high magnetic permeability μ is selected for the core of the transformer. However, the exact permeability always depends on the temperature, the applied stress (magnetostriction), and a number of other quantities. Changes in the permeability directly affect the measured ion current and can limit the current resolution.

- **External fields** - In the case of the PCT at CRYRING, the neighboring dipole magnets induce currents in the windings of the transformer and create big perturbations compared to the faint signal of the ion beam. Despite a magnetic (high-permeability) shield as well as an active compensation of the noise, there is a residual effect that make precise low current measurement – especially during ramps – impossible. Other sources of magnetic noise like turbo and getter pumps exist as well.

- **Local field distortion** - The field created by the beam can be very small (see Eq. (2.1)). Therefore, minor local effects can strongly influence the measurement. Induced eddy currents, the flow of secondary particles due to collisions of the beam with the wall of the beam-line and the accu-

mulation of electric charges on the ceramic insulators are all example of processes that create local fields that do not represent the beam current.

- **Barkhausen noise** - On an atomic scale, the magnetization of the core material is created by many separated domains of atoms. Within each domain all the spins of the atoms are aligned. When a magnetic field is applied, within the domains all atoms flip their spin simultaneously leading to a discrete jump in magnetization rather than a continuous change. The Barkhausen noise is resembled in low-frequency noise [20]. This effect limits the smallest constant current that the PCT can detect since it relies on the continuous saturation of the core even at a very small magnetization.

1.2.2 Ionization Profile Monitor

The IPM or Residual-Gas Profile Monitor [19] is a (mostly) non-destructive device which can operate with a wide range of beam currents and independent of the beam condition (bunched & coasting). Although it is primarily used for measurements of the transverse beam profile, it also can give a precise current reading by integrating the signal to obtain a count rate. With a strong electric potential (0.45 kV/cm at CRYRING) it collects all ionized particles created by the interaction of the beam with the residual gas of the beam-line vacuum (see Figure 1.6). In some special cases additional gas is injected locally to increase the number of secondary particles.

As each ion species has a different interaction with the residual gas and the amount of ionized particles depends on the vacuum conditions, the IPM needs to be calibrated for each beam-time before absolute currents can be determined. In addition to the amount of residual gas and the ion species, also the selected bias voltage of the micro-channel plates, which are used to detect the ionized particles, determines the final count rate. While the IPM is typically regarded as a non-destructive device, the electric field of the IPM interacts with the beam and for low-energetic particles it can steer and partially destroy the beam in the case that no corrections are applied.

At CRYRING, one IPM for each transverse plane is installed. The total count rate of the IPM is read out by a scaler-based data acquisition system LASSIE [21]

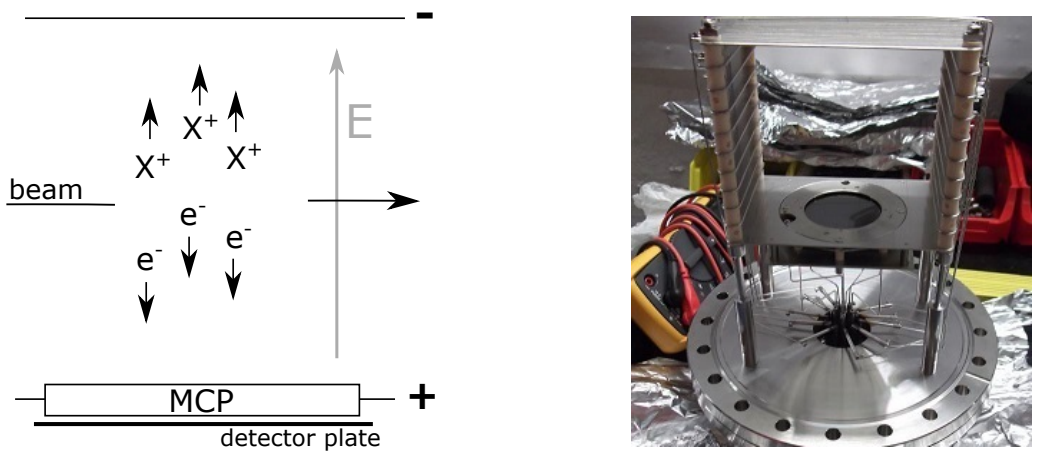

Figure 1.6: *(a) Schematic of an IPM. Charged secondary particles created by the interaction of the ion beam with the residual gas are accelerated toward a micro-channel plate (MCP). The count rate of the particles hitting the MCP is proportional to the beam current. (b) Photo of the IPM installed at CRYRING. Courtesy of A. Reiter [18].*

with an acquisition rate of 1 kHz. The count rate of the IPM can be as high as 150 kHz for a high-intensity beam. In this way, the IPM can be a very sensitive relative intensity diagnostics also at low beam intensities and with coasting beam. Additional information can be found in [15, 22].

1.2.3 Schottky monitor

A Schottky detector is a device designed primarily for the analysis of the coasting beam. At CRYRING, the Schottky noise probe consists of four 1350 mm long electrodes for transversal and longitudinal analysis [15]. Mathematically, the beam current – constituted by many individual ions – can be divided into a constant current plus a fluctuation term that is created by the spread of the momentum or the revolution frequency of the individual particles [19]. This second term is called 'Schottky signal' and its average power P_h of a given harmonic h is proportional to the number of ions N_{ions}, as shown in Eq. (1.2). $S(f)$ is the spectral power density of the signal measured by a spectrum analyzer.

$$P_{h,Schottky} = \int_{\Delta f_h} S(f)df \propto I_{\text{rms}}^2 \propto N_{\text{ions}} \tag{1.2}$$

The width Δf_h of the signal at each harmonic is proportional to the momentum distribution $\Delta p/p$ and typically is used to monitor beam cooling.

At CRYRING@ESR the Schottky detector is also used to measure the intensity of the bunched beam, which can be done with a high accuracy that is comparable with the data from the BPMs. For the measurement of a bunched beam, the spectrum analyzer that observes the frequency structure of the beam is operated in zero-span mode and displays the variation of the total signal power over time [15]. The extracted signal is proportional to the beam intensity, but needs to be calibrated with another beam instrumentation to obtain an absolute current measurement.

The use of the Schottky signal for monitoring coasting beam requires more complex signal processing and is not done at CRYRING. However at the Antiproton Decelerator and at the Extra Low ENergy Antiproton ring (ELENA) at CERN, the signal of the coasting beam in the longitudinal pick-up of the Schottky probe is digitized and the power spectral density (PSD) is calculated digitally by a Fast Fourier Transformation [23]. The number of stored particles is proportional to the power of a given harmonic of the revolution frequency (integral of the harmonic in the PSD) (see Eq. (1.2)). At the beginning of the beam time, the signal is calibrated with a proton beam at a much higher intensity ($\times 1000$), which allows the use of calibrated dc beam current transformers as an absolute reference. During regular low-intensity operation, the calibration is monitored with the signal from on ac transformer that measures the beam intensity of the extracted beam. The absolute measurement of the ac transformer after the extraction can be compared to the signal obtained from the Schottky analysis at the moment before the beam is extracted.

For ELENA – with beam intensities down to 230 nA – this method is at its limit due to significant stochastic noise and the lack of a calibrated current reference during routine operation [24, 26]. The reported rms error of the intensity measurement is between 2 % to 4 % in addition to the fluctuation or drift of the signal baseline. The installation of a CCC at ELENA has the potential to significantly improve the precision of the current measurement and remove the need to perform calibration measurements at higher intensities. An installation of a CCC in the ring is currently under investigation.

coasting	**FC** cal., destr.[1]	**PCT** calibrated	**ICT** calibrated	**BPM** uncal.	**Schottky** uncal.	**IPM** part. destr.[2]
Range	–	$\geq 10\,\mu A$	–	–	$\geq 100\,nA$	not def.[3]
Noise floor	–	$1.9\,\mu A_{rms}$	–	–	not det. (cf. [24])	$\leq 10\,Hz$[4] (param. dep.)
Output BW	–	dc – 100 Hz (LP filter)	–	–	def. by signal analysis	dc – 1 kHz (dep. on DAQ)
bunched						
Range	$\gtrsim 1\,nA$	$\geq 10\,\mu A$	$\geq 100\,nA$	$\geq 10\,nA$[6]	$\geq 10\,nA$	not def.[3]
Noise floor	$0.5\,nA_{rms}$ [5]	$1.9\,\mu A_{rms}$	$\geq 1\,nA_{rms}$ (@ 20 Hz BW)	$\geq 100\,pA_{rms}$[6] (@ 20 Hz BW)	not det. (cf. BPM)	$\leq 10\,Hz$[4] (param. dep.)
Output BW	dc – 1 MHz (LP filter)	dc – 100 Hz (LP filter)	dc – 100 Hz (BSP)[7]	dc – 100 Hz (BSP)[7]	def. by spectr. analyzer	dc – 1 kHz (dep. on DAQ)

[1]Used only as first-turn diagnostic, [2]at low beam energies, [3]count rate per ion strongly depends on measurement parameter, [4]dark count rate (cf. Sec. 6.5.1 for eq. current noise), [5]defined by Femto DHPCA-100 [25] amplifier with gain of 10^6, [6]CryRadio further improves this detection range and noise performance [18], [7]bunch shape processor.

Table 1.1: *Properties of selected beam instrumentation used for intensity measurements at CRYRING@ESR determined during the beam-time or taken from [16, 18, 19, 22]. The output bandwidth of the ICT and the BPM is defined by the Bunch Shape Processor (BSP). For bunched beam, the longitudinal Schottky pick-up is read out by a spectrum analyzer in zero-span mode.*

1.3 Prospects of the CCC

The non-destructive monitoring of low-intensity beams ($< 1\,\mu A$) with absolute precision throughout the whole acceleration cycle is very challenging, especially with constantly changing ion species and beam conditions. CRYRING is comparatively well equipped with multiple devices that can provide intensity data in this current regime. However, an absolute current measurement with coasting beam or during slow extraction is still very difficult or sometimes impossible. It requires tedious calibration procedures or is associated with a large calibration error. This gap in the intensity diagnostic restricts the experimental program at CRYRING@ESR and limits the accuracy of experiments that rely on a precise intensity measurement.

The Cryogenic Current Comparator is an excellent candidate to extend the calibrated measurement range of low-intensity dc beams down to ion currents in the order of nA and to significantly increase the available current resolution for coasting beams also at higher currents. In principle, the CCC can also be used to calibrate other instruments like the IPM. Not only at CRYRING but also

with the exotic low-intensity beams throughout FAIR, a fully functional CCC system will significantly support the experimental program and the machine operators. Therefore, several CCCs are planned to be installed throughout the transfer lines and storage rings at FAIR.

Measurements with a CCC beam monitor in the laboratory have shown that the detection of a current pulse with an amplitude of 5 nA or even lower using a detector bandwidth of 10 kHz is feasible [27]. An installation of a CCC at the Antiproton Decelerator at CERN showed that under the influence of all the perturbations from the accelerator environment at the beam-line, a current resolution of 30 nA is possible [7]. The work in this thesis aims to prove that a CCC system that is optimized for the beam conditions at CRYRING can be designed, integrated in and routinely operated at CRYRING@ESR which can provide the expected superior current resolution down to beam intensities of nA.

Chapter 2

Theory of SQUID magnetometry

The Cryogenic Current Comparator detects the beam current by comparing the magnetic field created by the moving charges of the ion beam to the field of a calibration current. For this purpose a Superconducting Quantum Interference Device (SQUID) is used as an extremely-sensitive current detector. This chapter provides a basic introduction into superconductivity and a first view on the properties of the superconducting wave function which can be used to measure magnetic field.

With ion species that are difficult to produce in large numbers, the amplitude of the magnetic field of the ion beam – e.g. with a total charge of 10 pC or below – is rather weak which makes its detection challenging. Considering the magnetostatic case, which is sufficient for describing the time-averaged beam current, the Maxwell equations can be reduced to the law of Biot-Savart which yields a direct relationship between an electric current $I_{dc}(\vec{r})$ and the magnetic field $\vec{B}(\vec{r})$ that is created. With the assumption that, locally, the ion current is equivalent to a current along a wire of infinite length, the Biot-Savart law can be simplified to

$$\vec{B}(\vec{r}) = |\vec{B}(r)|\,\hat{e}_\varphi = \mu_r\mu_0\frac{I_{dc}}{2\pi r}\,\hat{e}_\varphi \,\Bigg|_{\mu_0\approx 4\pi\cdot 10^{-7}} \approx 2\,\frac{I_{dc}}{r}\cdot 10^{-7}\,\hat{e}_\varphi \;\left[\frac{\mathrm{N}}{\mathrm{A}^2}\right] . \qquad (2.1)$$

The strength of the field at the detector position depends on the ion current I_{dc}, the distance r to the moving charges and the magnetic permeability μ_r of the matter that separates the two. With $\mu_0 \approx 4\pi \cdot 10^{-7}$ N/A^2 and typical design

values for the CCC operation of $I_{dc} = 10\,\mathrm{nA}$, the magnetic field at the distance that corresponds with the average radius of the detector ($r = 0.15\,\mathrm{m}$) is only $B = 130 \times 10^{-16}\,\mathrm{T} = 13\,\mathrm{fT}$.

At these small field strengths, an extremely sensitive magnetic field sensor, a so-called magnetometer, is required and it is a considerable challenge to eliminate external influences that can have an amplitude that is many orders of magnitude larger than the signal from the ion beam. One example is the magnetic field of the Earth which is around $50\,\mu\mathrm{T}$. Therefore, an effective magnetic shield is important to take advantage of the full measurement performance of the SQUID.

2.1 Superconductivity

For the description of the SQUID sensor a basic knowledge of superconductivity is required. In this section the fundamental concepts of superconductivity are introduced: In the scope of this work superconducting materials can be characterized by two properties that occur spontaneously below a critical temperature T_c, the expulsion of magnetic field lines (Meissner effect) and the drop of the electrical resistance to zero.

A first phenomenological theory to describe this behavior was developed by Fritz and Heinz London in 1935 [28]. They based their description on the Drude model, which applies Newton's law of mechanical motion to the movement of electrons inside an electric field $\vec{E}$ to estimate the electrical conductivity of a material. This approach leads to an effective force $\vec{F}_n$ on the charge carriers of

$$\vec{F}_n = m\frac{\partial \vec{v}_n}{\partial t} = -\frac{m\vec{v}_n}{\tau} + (-e)\vec{E}\ , \tag{2.2}$$

with the electron mass m, the mean velocity of normal-conducting charge carriers $\vec{v}_n$ and the mean time between collisions τ. Here the London brothers added the assumption that – for superconducting charge carriers with the current density $\vec{j}_s$ and with the superconducting charge density ρ_s – there is no collisions between the carriers at all ($\tau \to \infty$). With this assumption, Eq. (2.2) transforms to

$$m\frac{\partial \vec{v}_s}{\partial t} = (-e)\vec{E} \qquad \text{with} \qquad \vec{v}_s = \frac{\vec{j}_s}{(-e)\rho_s}\ , \tag{2.3}$$

$$\frac{\partial \vec{j_s}}{\partial t} = \frac{\rho_s e^2}{m} \vec{E} \ . \tag{2.4}$$

Equation (2.4) is called the *1. London equation.*

In order to derive the general London Equation an additional assumption is necessary. For the transversal electric field $\nabla \cdot \vec{E_T} = 0$, the Coulomb gauge ($\nabla \cdot \vec{A} = 0$) and the transversal component of the magnetic vector potential $\vec{A_T}$ the London equation can be reformulated as

$$\begin{aligned} \frac{\partial \vec{j_s}}{\partial t} &= -\frac{\rho_s e^2}{mc} \frac{\partial \vec{A_T}}{\partial t} \\ \text{with} \qquad \vec{E} &= -\frac{1}{c} \frac{\partial \vec{A_T}}{\partial t} \quad \text{and} \quad \vec{\nabla} \cdot \vec{A} = 0 \ . \end{aligned} \tag{2.5}$$

Omitting the time derivative on both sides – which is the core assumption of the London theory –, one obtains the general *London Equation*

$$\vec{j_s} = -\frac{\rho_s e^2}{mc} \vec{A_T} \ . \tag{2.6}$$

The superconducting current density $\vec{j_s}$ can be inserted in the static version of the Ampère-Maxwell equation to obtain the London penetration depth λ_L which is a description of the Meissner effect. When a magnetic field $\vec{B}$ penetrates a superconductor, it is suppressed exponentially depending on the distance z to the surface. For a static magnetic field $\vec{B}_{||}$ parallel to the surface of the superconductor the field strength is reduced according to

$$|\vec{B}_{||}(z)| = B_0 e^{-\frac{z}{\lambda_L}} \quad \text{with} \quad \lambda_L = \sqrt{\frac{m}{\mu_0 \rho_s e^2}} \ . \tag{2.7}$$

The London penetration depth is typically in the order of tens of nm and depends on the material properties ρ_s and m. The attenuation of the magnetic field inside the bulk of the superconductor can be described with screening currents which are confined to the surface layer of the superconductor with a thickness in the order of λ_L.

The two superconducting materials used for the superconducting shield of the CCC are niobium ($T_c = 9.25\,\mathrm{K}$) and lead ($T_c = 7.2\,\mathrm{K}$) with London penetration depths of 39 nm and 37 nm, respectively. The given values are valid for

anisotropic bulk material; thin films of the same material tend to have even higher critical temperatures [29].

2.2 The Josephson Junction

A more advanced but still phenomenological description is given by Vitaly Ginzburg, Lev Landau et al. in 1950 [30]. As an analogon to the wavefunction of quantum mechanics, they introduce a macroscopic complex order parameter $\rho_s(\vec{r}) = |\psi(\vec{r})|^2$ that can be calculated for any given material by using a total of four material properties which can be quantified experimentally. ψ is then used to define the free energy $f[\psi]$ of the system which gives an understanding of its basic properties. One of this properties is the *quantization of the magnetic flux* through a closed superconducting loop to integer values of the magnetic flux quantum $\Phi_0 \equiv h/(2e)$ according to

$$\Phi_{sc,loop} = m\,\Phi_0, \quad \forall m \in \mathbb{Z}\ . \tag{2.8}$$

The Ginzburg-Landau theory can be derived by the more fundamental microscopic theory of superconductivity developed by Barden-Cooper-Schriefer (BCS) in 1957 [31]. Using the BCS-theory, Brian Josephson investigated the interface between two superconductors that are separated by a thin layer of an insulator or a normal conductor. Due to the tunneling of charge carriers through the barrier, the two macroscopic wave functions – that describe the superconducting state in the superconductors – are weakly coupled. Brian Josephson predicted a super-current I_s that flows between the two superconductors at the interface, which is named *Josephson junction* to his honor. While there exist many different variations of Josephson junctions, in the scope of this thesis, only tunneling junctions are described in detail.

The amplitude of the current across the junction depends on the phase difference δ between the superconducting wave functions. In case a voltage U forms across the barrier, the phase difference changes with time and modulates the flowing super-current I_s up to the critical current I_c of the junction according to

$$I_s = I_c \sin\delta \qquad \text{with} \tag{2.9}$$

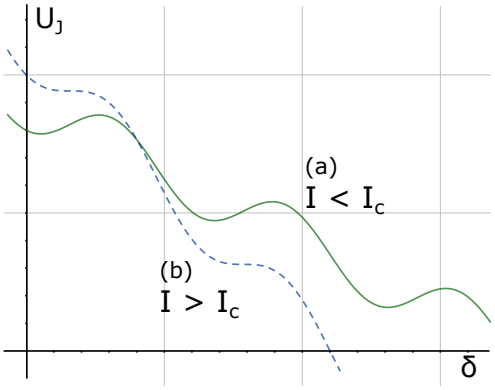

Figure 2.1: *The tilted-washboard potential U_J (see Eq. 2.13) is used in the 'equation of motion' for the phase difference δ between the macroscopic superconducting wave function at the Josephson junctions for two different total currents I applied.*

$$\dot{\delta} = \frac{2e}{\hbar} U \quad (\approx 483.6\,\mathrm{MHz/\mu V}) \; . \tag{2.10}$$

The two relations in Eq. (2.9) and (2.10) are called *first and second Josephson equation* [29]. With a finite voltage U applied to a Josephson junction, the total current I across the interface is a sum of the super-current I_s, the quasi-particle current I_q and the displacement current I_D

$$I = \underbrace{I_c \sin\delta}_{I_s} + \underbrace{\frac{U}{R}}_{I_q} + \underbrace{C\dot{U}}_{I_D} \; . \tag{2.11}$$

In practice, for the majority of Josephson junctions that are built, the barrier is shunted with a resistor R that is placed parallel to the junction and a capacitance C (which typically is its self-capacitance) to obtain a well-defined relation between the applied voltage and the resulting current [29]. With Eq. (2.11) the properties of a Josephson junction can be described using an equivalent electrical circuit, the *resistively and capacitively-shunted junction model (RCSJ-model).* Analogous to the equation of motion for a particle with a mass m and subject to a friction ξ, an equation of motion can be formulated for the phase difference δ [29]. With the Josephson relation (2.10) the voltage U in equation (2.11) can be written in terms of δ which leads to

$$\frac{\Phi_0}{2\pi} C\ddot{\delta} + \frac{1}{R}\dot{\delta} = I - I_c \sin\delta = -\frac{2\pi}{\Phi_0}\frac{\partial U_J(\delta)}{\partial\delta} \quad \text{with} \tag{2.12}$$

$$U_J(\delta) = E_J \left(1 - \cos\delta - \frac{I}{I_c}\delta\right) \ . \tag{2.13}$$

The tilted-washboard potential U_J (see Figure 2.1) is introduced as a way to visualize the forces that act on the superconducting wave function and the resulting direction or velocity of motion in δ. In case the current through the junction is smaller than the critical current ($I < I_c$) there are local minima in the potential and δ is confined to oscillations within one of the potential wells (a). Therefore, the mean value of δ is constant which – according to Eq. (2.10) – leads to a mean voltage $\langle U(t)\rangle_t$ across the junction of zero.

When the current exceeds the critical current ($I > I_c$) there is no potential well and $\dot{\delta}$ leads to a voltage at the barrier that increases with higher applied currents (b). In order to avoid hysteresis effects at the transition between those two phases, the typical Josephson junctions used in SQUIDs are strongly overdamped systems. In these systems δ is trapped in a potential well instantly as soon as the current through the junction is decreased below the transition at $I = I_c$. This leads to a normalized time-averaged voltage across the barrier of

$$\langle U(t)\rangle_t = \begin{cases} 0 \ , & \forall I \leq I_c, \\ \left\langle I_c R \, \frac{(I/I_c)^2 - 1}{I/I_c + \cos\omega t} \right\rangle_t = I_c R \sqrt{(I/I_c)^2 - 1} \ , & \forall I > I_c, \end{cases} \tag{2.14}$$

with $\omega = \omega_c \sqrt{(I/I_c)^2 - 1} = 2\pi I_c R/\Phi_0 \sqrt{(I/I_c)^2 - 1}$ which uses the characteristic frequency ω_c of the junction [29]. ω_c is equivalent to the Josephson frequency (2.10) with $U = I_c\, R$.

In the presence of thermal noise the transition phase is smeared out and for large noise values (e.g. high-temperature superconductors) the relationship between current and voltage approaches a linear behavior even at currents below the critical current. There are additional effects that modify the response of the SQUID which are important for a theoretical analysis, however for the understanding of the practical application of Josephson junctions in dc SQUIDs they can be neglected and therefore will not be discussed further. More information can be found in [29, 32].

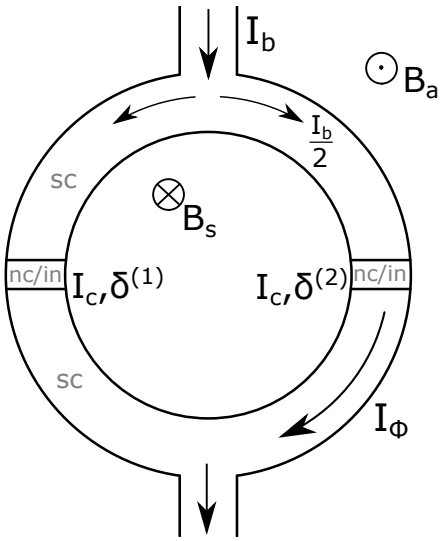

Figure 2.2: *Schematic of a simple dc SQUID with two Josephson Junctions* $\left(\delta^{(1)}, \delta^{(2)}\right)$ *formed by a superconductor–insulator–superconductor transition. Typically both junctions have identical properties and the same critical current* I_c*.*

2.3 The dc SQUID: Theory and Readout

The so-called dc SQUID consists of a closed superconducting loop that is divided by two Josephson junctions with the same critical current I_c. A schematic of a simple dc SQUID sensor is given in Figure 2.2. According to Eq. (2.8) the magnetic flux $\Phi_a = A_{eff} B_a$ that is enclosed by a superconducting ring with an effective area A_{eff} is quantized and can only be full integer multiples of Φ_0. An applied flux $\Phi_a \neq m\Phi_0$ is either lowered or increased to a full integer value by a screening flux $\Phi_s = L_t I_\Phi$ that is created by the circulating current I_Φ and the total inductance of the ring L_T. The total flux through the effective area of the SQUID is then $\Phi_T = \Phi_a + \Phi_s$. The relation between the applied magnetic flux Φ_a and the difference in the phase of the macroscopic wave function of the two superconductors at the two Josephson junctions $\left(\delta^{(1)}, \delta^{(2)}\right)$ is given by [29]

$$\delta^{(2)} - \delta^{(1)} = \frac{2\pi}{\Phi_0}\Phi_{Tot} = \frac{2\pi}{\Phi_0}(\underbrace{A_{eff}B_a}_{\Phi_a} + \underbrace{L_T I_\Phi}_{\Phi_s}) = \frac{2\pi}{\Phi_0}\left(\Phi_a + \frac{\Phi_0}{2I_c}\beta_L I_\Phi\right). \quad (2.15)$$

The screening parameter (also called the reduced inductance) $\beta_L = 2L_T I_c/\Phi_0$ therein is an indicator for the influence of the SQUID inductance L_T. Analogous

to the approach for a single Josephson junction (see Eq. (2.11)), the RCSJ-model can be used to describe the currents inside the pair of junctions that constitute a dc SQUID as

$$\begin{aligned} I_c \sin\delta^{(k)} + \frac{1}{R^{(k)}} U^{(k)} + C^{(k)} \dot{U}^{(k)} &= I_c \sin\delta^{(k)} + \frac{\Phi_0}{2\pi} \left(\frac{1}{R^{(k)}} \dot{\delta}^{(k)} + C^{(k)} \ddot{\delta}^{(k)} \right) \\ &= \begin{cases} I_b/2 - I_\Phi & \text{for junction } k = 1 \\ I_b/2 + I_\Phi & \text{for junction } k = 2 \end{cases} \end{aligned} \tag{2.16}$$

with an applied bias current I_b. Again the thermal noise term is omitted. With the two equations in (2.16) the behaviour of the SQUID can be described [29].

In the case of a negligible inductance of the SQUID ($\beta_L \ll 1$), the static solution of the coupled differential equations (2.16) for the critical current I_C of the SQUID is

$$I_C = 2I_c \left| \cos\left(\pi \frac{\Phi_a}{\Phi_0} \right) \right| \ . \tag{2.17}$$

According to Eq. (2.17) the combined critical current I_C of the two Josephson junctions of a SQUID change between 0 and $2I_c$ as a function of the applied flux Φ_a. With non-negligible values of $\beta_L \gg 1$, the critical current I_C given in Eq. (2.17) is reduced and scales loosely with $1/\beta_L$ [29].

In principle, a SQUID can be operated as a functional magnetometer in a superconducting mode by measuring the change of the critical current with the applied magnetic field. However, this readout scheme relies on a fixed magnetic field for the duration of the measurement. A more elegant readout is possible with a finite voltage drop across the junctions. It turns out that the modulation of I_C leads to a similar modulation in the voltage V across the SQUID. Assuming both junctions share the same parameters, the system is strongly over-damped and the inductance of the SQUID is negligible ($\beta_L \ll 1$), then Eq. (2.16) turns into the RCSJ-model for a single junction with a voltage modulation identical to Eq. (2.14) of

$$V = \frac{R}{2} \sqrt{I_b^2 - I_C^2} \ , \tag{2.18}$$

with the critical current I_C of the SQUID according to Eq. (2.17). The left side of Figure 2.3 shows the modulation of the normalized voltage drop $V/(I_c R)$ at

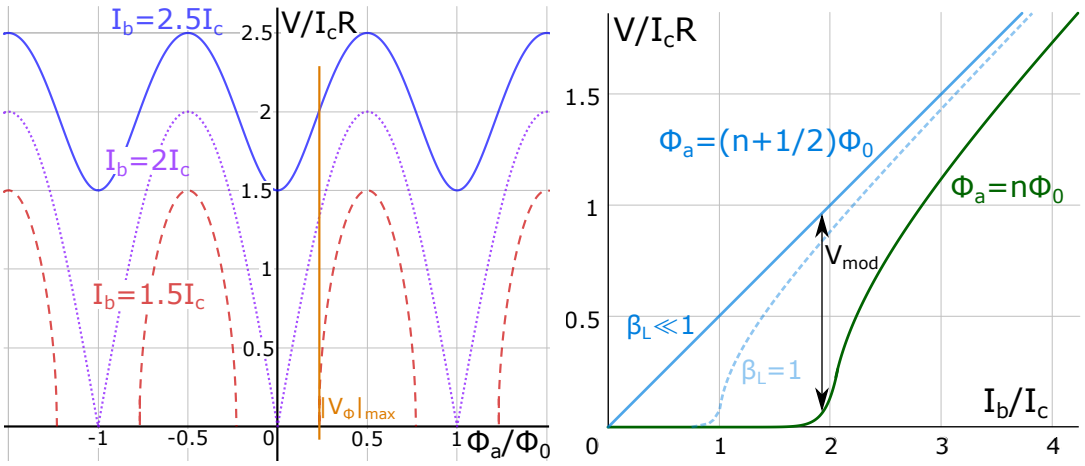

Figure 2.3: *(left) Modulation of the normalized voltage $V/(I_cR)$ across a dc SQUID with the applied magnetic flux Φ_a for a fixed bias current I_b of $1.5\,I_c$ (red), $2\,I_c$ (violet) and $2.5\,I_c$ (blue). The position of the optimal working point with the largest transfer function V_Φ is marked with an orange line. (right) The characteristic V–I curve of a strongly over-damped dc SQUID ($\beta_L \ll 1$) in the presence of thermal noise at a constant applied flux $\Phi_a = n\Phi_0$ and $\Phi_a = (n+1/2)\Phi_0$.*

the SQUID with an applied flux Φ_a/Φ_0 and for different bias currents I_b (from 1.5 to $2.5\,I_c$). The $V-I$ characteristic of the SQUID according to Eq. (2.18) is given on the right. Small variations of the applied flux Φ_a in the order of a fraction of the magnetic flux quantum Φ_0 lead to a significant measurable change in the voltage across the SQUID and thus can be detected. Although there are small deviations of the modulation pattern due to asymmetries of the Junctions and other parasitic effects such as resonances [32], the operating principle remains the same.

The sensitivity of the voltage with respect to changes of the magnetic flux $V_\Phi = |\partial V_{sq}/\partial\Phi_a|$ is called the dc SQUID transfer function and depends on which point along the $V-\Phi$ modulation in Fig. 2.3 the measurement is performed. In general, for dc SQUIDs the optimum with the largest transfer function can be found at $\Phi_a \approx 0.25\,\Phi_0$ with $\beta_L \approx 1$. Often, the bias current I_b is optimized manually directly before the measurement. Without considering the effect of the resonances of a particular SQUID setup, it can be shown that in the configuration at which the transfer function is maximized, the low-frequency flux noise is at its minimum. [29]

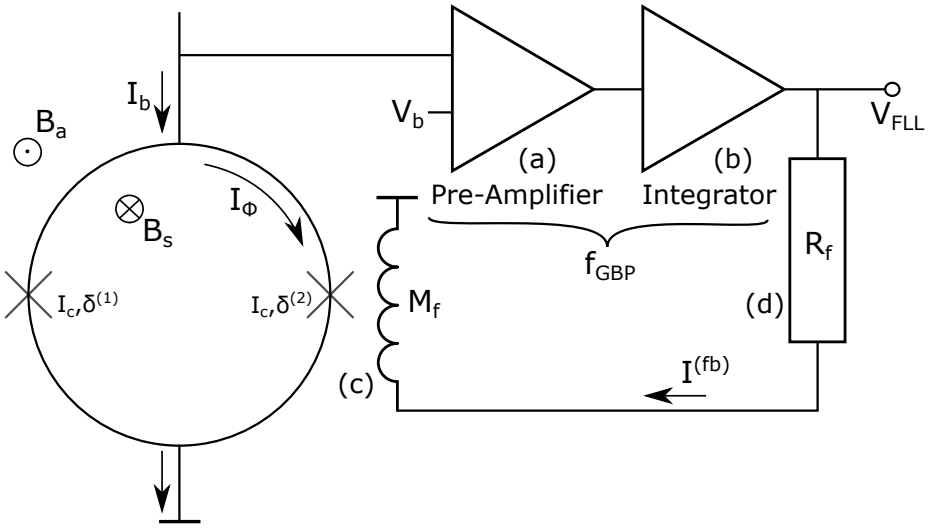

Figure 2.4: *Circuit diagram of the FLL readout electronics for a dc SQUID. The FLL feedback scheme linearizes the output of the SQUID to an external flux.*

2.3.1 SQUID electronics and FLL mode

For each dc SQUID there exists a combination of Φ_a and I_b that maximizes the transfer function $|\partial V_{sq}/\partial \Phi_a|$ and gives an optimal sensitivity. Therefore, it is advantageous when the applied flux during the measurement is kept constant even with varying external magnetic field. In this so-called flux-locked loop (FLL) mode the voltage signal of the SQUID is used in a feedback loop to drive a feedback coil with a mutual inductance M_f to the SQUID. The local magnetic flux induced by the feedback current $I^{(\mathrm{fb})}$ cancels any deviation (e.g. due to external fields) from the preset operating flux Φ_a and thus maintains the optimal working point. At the same time, the feedback current $I^{(\mathrm{fb})}$ that is required to counteract the external signal naturally is directly proportional to the amplitude of the external flux and can be converted to a measurable current V_{FLL} using a feedback resistor R_f.

Moreover, this readout scheme linearizes the periodic voltage output V_{sq} of the SQUID (see Fig. 2.3) and allows the tracking of signals that are larger than one Φ_0. Additionally, with the FLL readout the transfer factor between the external input flux and the detected signal V_{FLL} in the ideal case is independent on the magnitude of the transfer function and only depends on the fixed design parameters of the feedback (M_f and R_f).

A wiring diagram of one possible readout scheme for the FLL mode is shown in Fig. 2.4. The voltage deviation from the working point of the SQUID due to an external flux is amplified (a), an integrator (b) obtains the absolute difference in voltage and creates the feedback current $I^{(\mathrm{fb})}$ that induces the counteracting magnetic field at the SQUID via the feedback coil (c) [29].
The measurement range of the FLL readout is determined by the feedback resistor R_f (d) and by the mutual inductance M_f in combination with the connected SQUID. In general, the intrinsic noise of the SQUID readout is rather low and in most cases, the dynamic range of the setup is not limited by the SQUID system itself but by the ADC that is used to digitize the signal. With a large dynamic range of the signal output due to a small R_f, the flux noise of the SQUID is usually lower than the resolution limit of a standard ADC. The overall flux noise density $S_{\Phi,\,\mathrm{FLL}}$ of a dc SQUID using an FLL readout can summarized by

$$S_{\Phi,\,\mathrm{FLL}} = S_\Phi + \frac{S_{V,\,\mathrm{AMP}}}{V_\Phi^2} + S_{I,\mathrm{AMP}} M_{dyn}^2 \quad , \tag{2.19}$$

with the intrinsic flux noise density of the SQUID S_Φ, the white voltage noise density $S_{V,\,\mathrm{AMP}}$ and the current noise density $S_{I,\mathrm{AMP}}$ of the pre-amplifier [29]. At large frequencies ($f \gg 1\,\mathrm{kHz}$), $S_{I,\mathrm{AMP}}$ is usually negligible due to the small dynamic resistance at the working point of the SQUID itself. However, at smaller frequencies semi-conductor based amplifiers can exhibit an increased current noise that needs to be taken into account.
The flux noise of the SQUID S_Φ consists of a white noise that determines the noise level at larger frequencies and a $1/f$-noise that becomes dominant at very low frequency applications ($f < 2\,\mathrm{Hz}$). The white noise has its origin in thermal fluctuation of the current across the Josephson junctions. The origin of the $1/f$-noise is still not entirely clear [33, 34]. For Josephson tunnel junctions based on high-temperature superconductors the $1/f$-noise can be described by the fluctuation of junction parameters (e.g. of the critical current of the junction) and by the motion of magnetic flux lines trapped in the bulk of the superconductor of the SQUID. However, these effects are usually rather small for SQUIDs based on low-temperature superconductors [29]. In the application as a beam diagnostic device, at low frequencies all the intrinsic noise contributions are overshadowed by external perturbations in the accelerator environment.

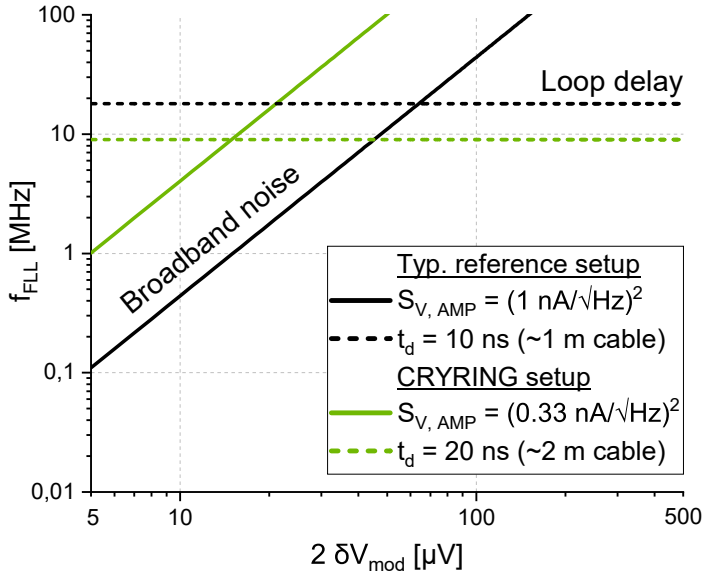

Figure 2.5: *Calculated maximum theoretical bandwidth limit due to broadband noise of the amplifier (cf. Eq.* (2.20)*) and due to the loop delay of the cables and the signal processing (cf. Eq.* (2.21)*) for a typical SQUID setup and for the setup at CRYRING [32].*

During operation, the bandwidth of the feedback loop it typically adjusted by changing the combined gain-bandwidth-product f_{GBP} of the amplifier and of the integrator, which affects their unity-gain frequency f_1. However, the overall system bandwidth is determined by multiple additional factors that set stringent limits on the maximum usable bandwidth [32].

One of them is the loop delay time t_d, which is the signal delay between the SQUID and the readout electronics. A maximum 3dB-bandwidth $f_{\mathrm{FLL,max}}$ of a SQUID system with a given loop delay t_d of

$$f_{\mathrm{FLL,\,max}}^{(\mathrm{loop\ delay})} = 2.25 f_1 = 0.18/t_d \ , \tag{2.20}$$

can be achieved when the product of the loop delay and of the unity-gain frequency f_1 of the open feedback loop are selected according to $f_1 t_d = 1/(4\pi)$ [29, 32]. In the case that $f_1 t_d$ is larger than the optimum value ($f_1 t_d > (4\pi)^{-1}$) a resonance in the transfer function forms close to the cut-off frequency without significantly extending the bandwidth limit which impairs the stability of the system. For smaller $f_1 t_d < (4\pi)^{-1}$ the maximum system bandwidth is reduced.

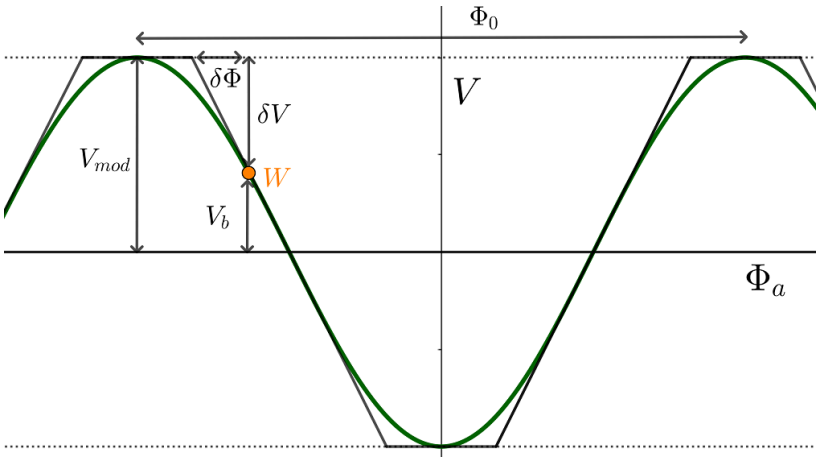

Figure 2.6: *Linear approximation of the periodic modulation of the voltage across the SQUID V_{sq} with an applied field Φ_a ($V_{sq}-\Phi_a$ characteristic) [32]. The usable voltage swing δV and the linear flux range $\delta\Phi$ around the working point W used for the estimation of the maximum bandwidth are indicated.*

Therefore, the FLL electronic, including the pre-amplifier and the active feedback circuit, has to be placed as close to the SQUID sensor as possible to reduce t_d to increase the usable bandwidth, and more importantly the slew rate [29, 32]. Typical values for the loop delay are around $t_d \sim 10\,\mathrm{ns}$ [29, 35] with a distance of around 1 m between the SQUID and the room-temperature electronics (in the SQUID system at CRYRING the length is 1.9 m). This corresponds to a maximum system bandwidth of around 20 MHz (about 9 MHz for $t_d \approx 20\,\mathrm{ns}$ with the cable length at CRYRING) (see Fig. 2.5). In addition, the finite bandwidth of the amplifier which is part of the FLL readout introduces an signal delay $t_{d,\,\mathrm{AMP}}$ that leads to a further reduction of the maximum system bandwidth by a factor of roughly 0.8 [32].

Furthermore, the system bandwidth is limited by broadband noise $S^b_{\Phi,\,\mathrm{FLL}}$ that consists of the amplifier noise $S_{V,\,\mathrm{AMP}}$ and of the voltage noise of the SQUID $S_{V,\,\mathrm{SQ}}$. Within the feedback loop their noise contribution is amplified, integrated and guided back to the SQUID. Excessive broadband noise will reduce the transfer function V_Φ, the maximum slew rate and affect the stability of the feedback. The maximum 3dB-bandwidth of the system, without significantly affecting the output signal, is given according to [29, 32] by

$$f_{\mathrm{FLL,\,max}}^{(\text{broadband noise})} \simeq 0.0044\,(2\,\delta V)^2/(S_{V,\,\mathrm{AMP}} + S_{V,\,\mathrm{SQ}})\ . \tag{2.21}$$

The usable voltage range δV is the difference between the amplitude V_{mod} of the $\Phi - V$ modulation of the SQUID and the bias voltage V_b at the working point according to $\delta V = V_{mod} - V_b$ (cf. Fig. 2.6). Thus, to reach a high bandwidth, the amplitude of the modulation needs to be increased while the noise of the components need to be reduced (see Eq. 2.21). In this way, ideally the bandwidth of the SQUID system is ultimately limited by the loop delay rather than the broadband noise. According to Fig. 2.5, the transition between the two bandwidth limitations for the setup at CRYRING is expected to be around a usable voltage range of $2\,\delta V = 15\,\mu\mathrm{V}$ which means the maximum bandwidth of the system is primarily limited by the loop delay.

Using the unity-gain frequency f_1 of the FLL feedback circuit, for an idealized SQUID system with a one-pole integrator the maximum slew rate $\dot{\Phi}_{f,\,\max}$ can be calculated according to

$$\dot{\Phi}_{f,\,\max} = 2\pi f_1 \delta\Phi \lesssim \Phi_0 f_1 \ . \tag{2.22}$$

However, taking into account the broadband noise $S^b_{\Phi,\,\mathrm{FLL}}$ – but without considering the loop delay – the resulting maximum slew rate is reduced and can be estimated based on a linear approximation of the SQUID modulation (cf. Fig. 2.6) to be

$$\begin{aligned} \dot{\Phi}^b_{f,\,\max} &= 2\pi f_{\mathrm{FLL}} \left(\delta\Phi - S^{b,\,\mathrm{peak}}_{\Phi,\,\mathrm{FLL}}\big(f_{\mathrm{FLL}}\big)\right) \quad \text{with} \\ S^{b,\,\mathrm{peak}}_{\Phi,\,\mathrm{FLL}}\big(f_{\mathrm{FLL}}\big) &= 4\, S^{b,\,\mathrm{rms}}_{\Phi,\,\mathrm{FLL}}\big(f_{\mathrm{FLL}}\big) = \frac{4}{V_\Phi}\sqrt{\frac{\pi}{2} f_{\mathrm{FLL}}\left(S_{V,\,\mathrm{AMP}} + S_{V,\,\mathrm{SQ}}\right)} \ , \end{aligned} \tag{2.23}$$

with the 3dB-bandwidth of the system f_{FLL} after considering the effect of noise and with the linear flux range $\delta\Phi$. More details on the derivation can be found in [32]. Looking at Eq. (2.23) it becomes apparent that a reduction of the transfer function V_Φ and of the usable voltage range δV both leads to a reduction of the maximum achievable slew rate.

Considering the effect of the loop delay t_d, the maximum bandwidth $f_1 = 1/(4\pi t_d)$ can be inserted into Eq. (2.22) [29] to obtain

$$\dot{\Phi}^d_{f,\,\max} = \frac{\delta\Phi}{2t_d} \lesssim \frac{\Phi_0}{4\pi t_d} \ . \tag{2.24}$$

A loop delay of 10 ns (20 ns) leads, according to the upper limit in Eq. (2.24), to a maximum slew rate of $8\,\Phi_0/\mu s$ ($4\,\Phi_0/\mu s$) which is independent of the transfer function. In practice, maximum slew rates that can be achieved with direct read-out schemes are typically 1 to $10\,\Phi_0/\mu s$ [29].

2.3.2 SQUID radiation hardness

In preparation for the installation of several SQUIDs along the accelerator beam-line where they are exposed to a moderate amount of radiation, the performance of the dc SQUIDs of two manufacturers (Magnicon GmbH and Supracon AG) were tested before and after exposure to a total radiation dose of 1.368 kGy at the CERN High Energy Accelerator Mixed-field (CHARM) irradiation facility at CERN [36]. One of the four SQUIDs that were irradiated showed a deterioration in its performance, however it did not fully destroy its measurement capability.

The expected radiation level at FAIR strongly depends on the installation location. At the transfer lines the beam losses are expected to be small and the radiation level will be rather low. There the irradiation dose D_{sq} directly at the beam-line is estimated to be

$$D_{\mathrm{sq}}^{(\text{transfer line})} \leq 10\,\mathrm{Gy/a}\ , \tag{2.25}$$

which – in the worst case – can sum up to several hundred Gray during the operating life of the SQUID. An irradiation target at CHARM of 1 kGy was selected to simulate the total exposure throughout the operational life and to take into account a comfortable safety margin in case the radiation is larger than expected.

The dc SQUID sensors – with Josephson junctions made of niobium and aluminum oxide – were supplied free-of-charge by Magnicon GmbH (type C6XL1 and C6XL1W) and by Supracon AG. The entire sample consisted of the SQUID on a fiberglass carrier with the outer dimensions of $17 \times 7.2 \times 3$mm (Magnicon) and $13 \times 7.5 \times 2$mm (Supracon). At CERN they were installed at the CHARM irradiation facility and were irradiation for a total of 3 weeks. During this time the samples were mounted behind a copper target which was hit by a proton

Accumulated dose [Gy]	1368
High Energy Hadrons (HEH) fluence ($>20\,\mathrm{MeV}$) [cm^{-2}]	6.30×10^{12}
1 MeV n equivalence [cm^{-2}]	1.02×10^{13}
Total number of particles-on-target	3.81×10^{16}

Table 2.1: *Accumulated radiation dose of the SQUID sensor during an irradiation for a total of three weeks at the CHARM irradiation facility. All values have an uncertainty of* 35 % *[37].*

beam with an energy of 24 GeV. The accumulated radiation dose is given in Tab. 2.1. Figure 2.7 shows the flux of particles at different energies and for different particle species.

After the irradiation, the sensors were returned to the companies to look for any deterioration of the performance. For both of the SQUID models by Magnicon no significant performance reduction could be observed. However, one of the sensors by Supracon showed a reduction of the amplitude of the $V_{\mathrm{sq}} - \Phi_a$ modulation by 42 % which negatively affects the SQUID transfer function V_Φ. Moreover, a larger bias current was required to achieve the maximum voltage modulation which could be in total addressed to be an electrostatic damage rather than a radiation effect. The performance of the second SQUID by Supracon was unchanged after the irradiation.

While the irradiation of SQUID sensors by the Supracon AG should be repeated to get a clear picture, the overall result is an indicator that SQUIDs in general – and the SQUIDs supplied by the Magnicon GmbH in particular – are largely unaffected by a moderate amount of ionizing radiation. Similar results for Josephson junctions from different materials are reported in literature [38].

However, the knowledge that the SQUID can maintain its performance after being irradiated is not sufficient to guarantee a smooth operation while it is exposed to radiation at the same time. During this test, the SQUID was not superconducting and there was no voltage applied to the sensor, which can change the effect of radiation on the circuit. Moreover, with the system being active there is the possibility for single-event effects that can lead to damage in the electric circuit or that can produce anomalies in the measured signal. In order to exclude these effects a more complex radiation test – in which the performance

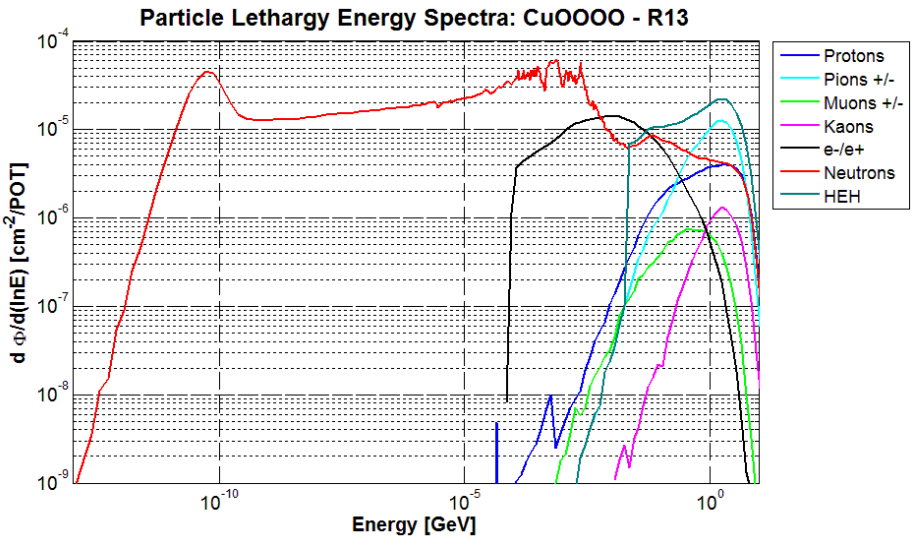

Figure 2.7: *The spectrum of the particle flux at different energies for various particle species at the location of the SQUID sensors during the irradiation at the CHARM test facility [37].*

of the SQUID is monitored during the radiation – is required. Please note that the standard FLL electronics uses many electric components that are known to not be radiation hard and thus the electronics need to be placed in an area shielded from ionizing radiation. Due to bandwidth limitations, the distance between the SQUID and the FLL readout electronics should be kept as short as possible (typically below 5 m for an FLL bandwidth of 1 MHz).

In addition to the CCCs planned in low radiation environments, there is one CCC installed at a distance of around 14 m to the extraction of the SIS100 synchrotron where higher levels of radiation are expected. The radiation dose throughout FAIR is estimated by the radio protection department at GSI and generally can be seen as an upper limit that is based on higher beam losses than what can be achieved in practice. Directly at the extraction with an assumed beam loss during slow extraction of 3×10^{10} U^{28+} ions per second at an energy of 2.7 GeV/u the accumulated radiation dose is 300 kGy/a when there is continuous operation for 250 days [39]. At the proposed location of the CCC the expected dose is still

$$D_{\mathrm{sq}}^{(\mathrm{FAIR})} \leq \frac{1}{d^2}\, D_{\mathrm{extaction}} \approx 1.5\,\mathrm{kGy/a}\ . \tag{2.26}$$

While this larger radiation dose was not tested within the scope of this thesis, according to literature Josephson junctions can survive this level of radiation [38]. However, even more care has to be taken that susceptible electric components connected to the operation of the SQUID are protected.

Chapter 3

The Cryogenic Current Comparator

The Cryogenic Current Comparator (CCC) for beam intensity measurements has its origin in the cryogenic current comparators that have been used in metrology to quantify resistances and currents with highest precision. In this chapter, the basic concept of a CCC is introduced together with all the elements that are necessary to operate a CCC at an accelerator beam-line.

With a CCC, two currents (I_a, I_{cal}) can be compared by observing the magnitude of their superimposed magnetic field B_I [1]. During the measurement, the currents are sent with opposite polarity through two parallel wires. The two currents each create a magnetic field according to the law of Biot-Savart in Eq. (2.1). The fields superimpose and – in case the magnitude of the currents are identical – their magnetic fields cancel out completely. In the presence of a small deviation between the currents, there is a residual magnetic field B_I remaining and the resulting magnetic flux is detected with a Superconducting Quantum Interference Device (SQUID) either directly or via the pick-up coil L_p and a flux transformer. The measured flux Φ_I is directly related to the difference of the currents $I = I_a + (-I_{cal})$. For an absolute current measurement, the (well-defined) calibration current I_{cal} can be tuned until the measured flux becomes zero when I_{cal} matches the input current I_a.

In practice, when two separate wires are used to carry the currents, the mutual inductance of each wire to the SQUID is not exactly the same. Depending on

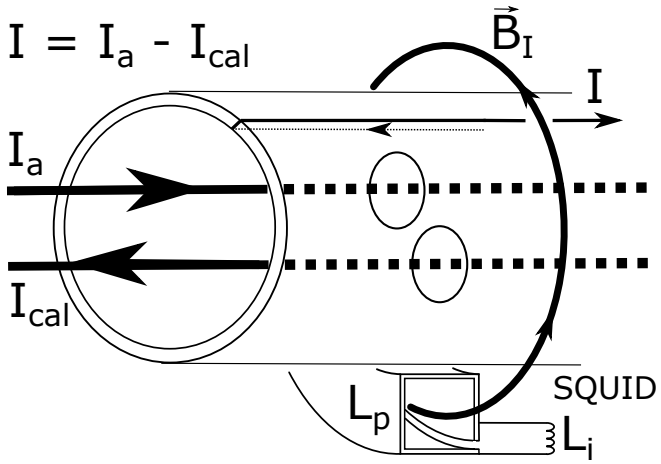

Figure 3.1: *Two opposing currents (I_a, I_{cal}) through a superconducting tube induce a Meissner screening current I on its surface, unless they are identical. The magnetic flux outside the tube Φ_I is measured by a SQUID and is directly related to the difference in the two original currents.*

small details like the geometry of the wire and the distance from the path of each wire to the pick-up of the SQUID there can be a significant difference between the two inductances which introduces an error to the measurement.

To harmonize the values of the mutual inductance both currents are sent through a superconducting tube (see Fig. 3.1). According to the Meissner effect, a homogeneous screening current I with a magnitude equal to the combined field of the enclosed currents ($I = I_a - I_{cal}$) is induced on the inner surface of the superconducting tube and prevents the flux to enter the bulk of the superconductor. On the outer surface of the tube, the same screening current generates a magnetic field that is independent on which of the two wires inside the superconducting tube carries the current. In this way, both wires have an identical mutual inductance to the SQUID and can be compared with highest precision [1, 2, 40].

3.1 A CCC for beam intensity monitoring

In analog to the metrological cryogenic current comparator, the CCC monitors the beam current by comparing the magnetic field created by the moving charges of the ion beam I_a to the field of a well-defined reference current I_{cal}. Figure 3.2 shows the measurement principle of the CCC for beam intensity monitoring. To

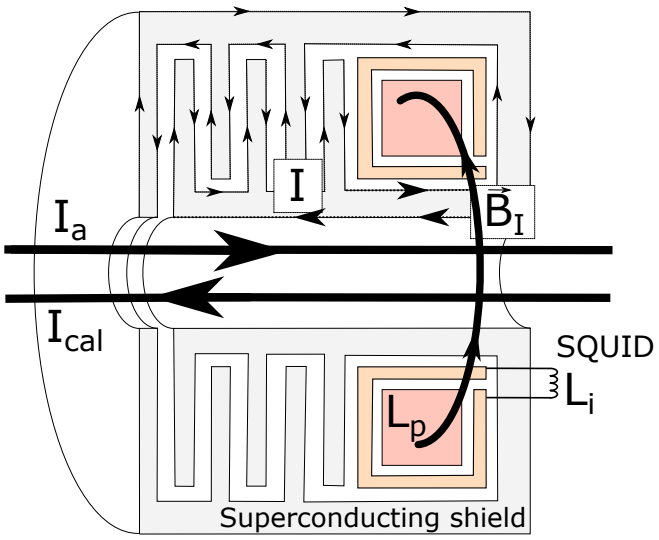

Figure 3.2: *Schematic of the CCC with radial shield geometry. The rotational axial symmetry of the superconducting shield strongly attenuates non-symmetric ($\neq B\hat{e}_\varphi$) magnetic field components. The magnetic flux inside the pick-up inductance L_p created by the ion beam I_a is detected by the SQUID sensor and is compared to a reference calibration signal I_{cal}.*

avoid the continuous matching of the calibration current to the variable input current, it is possible to obtain a calibration factor k that links the magnetic flux Φ_I that is detected by the SQUID to the applied current I_a. In this way the sensing current I_{cal} can stay constant or can be omitted during the measurement. This is a deviation from the metrological cryogenic current comparator, however, the underlying measurement principle is the same.

To determine the flux-to-current calibration factor k, a reference current is fed through a normal-conducting calibration wire that runs parallel to the ion beam. As pointed out above, due to the superconducting tube the effect of the position of the current within the detector on the total magnetic field that is measured is negligible. A toroidal superconducting pick-up (as shown in Fig. 3.2) with inductance L_p is used to couple the field to a dc SQUID via the input inductance L_i. All components that carry the signal from the pick-up to the SQUID are superconducting and there are no resistive losses that limit a normal-conducting current transformer and thus allow the measurement of dc currents.

A major challenge in the operation of a SQUID sensor is the mitigation of external perturbations. Due to the geometry of the pick-up coil of the CCC, its

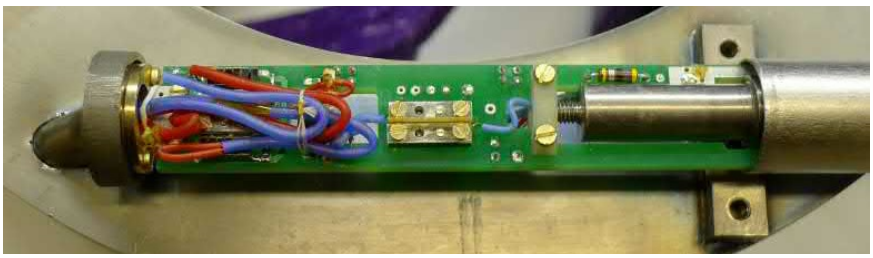

Figure 3.3: *SQUID cartridge of a very similar CCC system in operation at CERN. The cartridge encloses the flux transformer and the SQUID sensor, which is protected by an additional shielding can on the right hand side. On the far left the cartridge is connected to the shield enclosing the pick-up coil. Picture taken from [8].*

inductance is highest for azimuthal field components $B_\phi \hat{e}_\phi$. This is a first filter against external perturbations that could interfere with the measurement. However, it is impossible to build a perfectly selective pick-up and at a particle accelerator there is a broad range of magnetic fields that are many orders of magnitude stronger (up to several T) than the field of the ion beam. In order to shield the pick-up from these external magnetic fields, the superconducting tube – which homogenizes the mutual inductance of the calibration and the measurement wires to the toroidal pick-up coil of the SQUID – is expanded to form a passive superconducting shield that surrounds the pick-up almost entirely (see Sec. 3.3).

To protect the SQUID and the flux transformer from direct interference by external fields, they are mounted inside a separate shielding cartridge fixed to the outside of the superconducting shield and are connected to the pick-up by a pair of superconducting wires that go through miniature holes in the surface of the shield (see Fig. 3.3). Inside the cartridge, the SQUID itself is again enclosed by a small niobium cylinder. The only opening is a small hole for the connection to the readout electronics of the SQUID. Finally, the input inductance of the SQUID L_{sq} usually is manufactured in a gradiometer design which filters out homogeneous magnetic field components and thus leads to an attenuation of distant perturbation sources. The combination of all these measures make a direct coupling of magnetic fields to the SQUID very unlikely and all the signal that reaches the SQUID is coupled in through the pick-up circuit.

The pick-up, its superconducting shield and the dc SQUID constitute the CCC detector system. The CCC encloses the beam-line of the accelerator and is in-

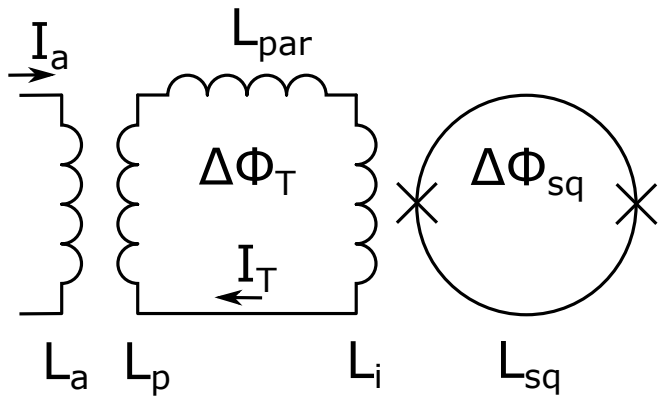

Figure 3.4: *Schematic of the coupling transformer of the CCC.*

stalled inside a cryogenic support system (see chapter 5). The SQUID is operated in flux-locked-loop (FLL) mode and measures the change of the magnetic flux $\Delta\Phi$ from the point when the FLL readout scheme is activated. At its core, the CCC is a relative measurement that is designed to monitor changes of the beam current independent of the absolute current that is present when the SQUID enters FLL mode. To get an absolute current measurement, a reference flux needs to be selected. For the application at the accelerator, a natural reference point is the zero-beam flux, which is the flux background that is present when there is no beam in the beam-line.

3.2 Superconducting flux transformer

In principle, the magnetic field of the ion beam can be measured directly with a SQUID without the need for a dedicated pick-up circuit. However, the inductance of a SQUID L_{sq} – and with it its effective measurement area – is kept small to minimize the intrinsic noise of the measured output signal [29]. Consequently, the response of the SQUID to the ion beam will be very weak with a poor signal-to-noise ratio. In order to amplify the response of the SQUID to the field of the ion beam, the effective flux-sensing area needs to be expanded. This is achieved with the superconducting pick-up coil L_p that is coupled inductively to the SQUID via an input coil L_i that is included on the chip carrier of the SQUID. Figure 3.4 shows a schematic of the configuration including a term for any parasitic inductance L_{par}.

For an ideal transformer, the coupling of two coils (m, n) – each in their separate system (A, B) – is described by the mutual inductance $M_{(m,n)}$ and by the coupling constant constant $k_{(m,n)}$ according to

$$\begin{aligned} \Phi &= L\, I \ , \\ \Phi_A &= M_{(m,n)}\, I_B = k_{(m,n)} \sqrt{L_m L_n}\ I_B \ . \end{aligned} \tag{3.1}$$

A primary current I_a (an ion beam or a calibration current) creates the magnetic flux $\Delta\Phi_T = M_{(p,a)} I_a$ in the pick-up loop which can be seen as the secondary winding of a transformer. The change of the magnetic flux induces the current $I_T = \Delta\Phi_T / L_T$ in the pick-up circuit with the total inductance of $L_T = L_p + L_{par} + L_i$. With Eq. (3.1) the change of flux in the SQUID $\Delta\Phi_{sq}$ due to a primary current I_a can be written similar to [10, 41] as

$$\begin{aligned} \Delta\Phi_{sq} = M_{(sq,i)}\ I_T = M_{(sq,i)} \frac{\Delta\Phi_T}{L_T} = M_{(sq,i)} \frac{M_{(p,a)}\, I_a}{L_T} = \\ = k_{(sq,i)}\, k_{(p,a)} \frac{\sqrt{L_{sq}\, L_i\, L_p\, L_a}}{(L_p + L_{par} + L_i)}\ I_a \ . \end{aligned} \tag{3.2}$$

With $d(\Delta\Phi_{sq})/dL_i = 0$, it can be determined that the maximum signal at the SQUID is achieved when the primary inductance $(L_p + L_{par})$ and the secondary inductance (L_i) are identical (impedance matching) according to

$$L_i = L_p + L_{par} \ . \tag{3.3}$$

With Eq. (3.3), the beam coupling $M_{(p,a)} = L_p = L_a$ and with the idealized coupling factors $k_{(m,n)} \equiv 1$, Eq. (3.2) can be written as

$$\Delta\Phi_{sq} \approx \frac{1}{2} \sqrt{L_{sq}}\, \frac{\sqrt{L_p + L_{par}}}{\left(1 + \frac{L_{par}}{L_p}\right)}\ I_a \ . \tag{3.4}$$

This relation can be used to determine the transfer coefficient between the intrinsic flux noise of the SQUID sensor $\Delta\Phi_{sq}^{(\mathrm{noise})}$ and the resulting current noise of the output signal $I_a^{(\mathrm{noise})}$. Moreover, Eq. (3.4) shows that indeed the flux at the SQUID due to an applied current I_a increases with a larger inductance L_p of the pick-up (e.g. because of a core with a high magnetic permeability). How-

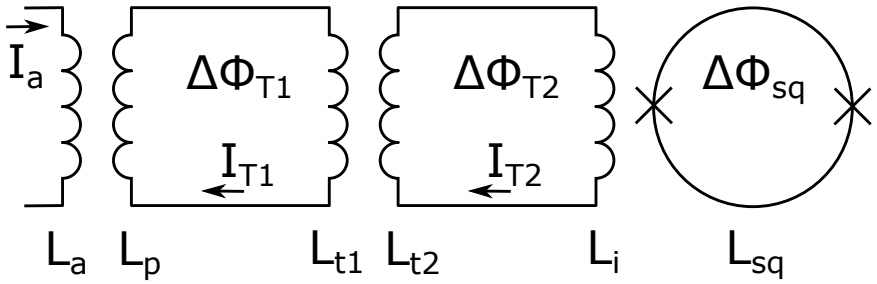

Figure 3.5: *Schematic of the 2-stage coupling transformer of a CCC with a large inductance of the pick-up (e.g. due to a high-permeability core).*

ever, with $L_p \gg L_{par}$ the effect of the parasitic inductance becomes negligible. The resulting impedance mismatch between the pick-up and the SQUID can be mitigated with an additional flux transformer. Figure 3.5 shows a schematic of the modified pick-up circuit. Eq. (3.2) can be expanded to include another transformer such that the system with a high-permeability core is described by

$$\Delta\Phi_{sq}^{(core)} = M_{(sq,i)} M_{(t_2,t_1)} M_{(p,a)} \frac{1}{L_{T_1} L_{T_2}} \, I_a \; . \tag{3.5}$$

The inductances of the primary and secondary winding of the additional flux transformer are given by L_{t_1} and L_{t_2}. The sum of the inductances of the two circuits are given by L_{T_1} and L_{T_2}. With an impedance matching of the primary and secondary inductances ($L_p = L_{t1}$, $L_{t2} = L_i$) an optimal transfer of the signal can be achieved [27].

In addition to the optimization of the transport of the signal, the flux transformer can be used to modify the frequency response of the system. The inductance of the pick-up coil and the capacity of the shielding structure together create a LC resonator which can amplify external perturbation and which can make a stable operation of the SQUID impossible. With an adequate design of the flux transformer, the resonance can be dampened to avoid any negative influence on the measurement. When signals with a high slew rate are expected, a low-pass filter can decrease the field gradients at the SQUID to values below $10\,\Phi_0/\mu s$, which can be tracked by the FLL electronics. Depending on the measurement task, the frequency response can be adjusted further.

3.3 Topology of the superconducting shield

As pointed out before, the dominant source of errors in current measurements with the CCC are external perturbations. Therefore, particular attention is given to the design of a superconducting shield to attenuate magnetic field components that do not carry information about the beam current. Since magnetic fields can not penetrate superconductors beyond the London penetration depth as long as the field strength is below the critical field, superconducting housings make excellent magnetic shields.

In 1976, Grohmann *et al.* [40] described the field attenuation of a shield design that is based on an axial stack of multiple ring cavities depicted in Figure 3.6 (left). Effectively, the stack of these cavities forms two coaxial tubes which then are connected on one end, where they enclose the pick-up winding (L_p) of the detector. The effective length l_e of the path within the coaxial tubes between the entrance and the position of the pick-up winding as well as the radial dimensions define the overall screening factor. The length l_e is increased by additional ring-disks that intrude the space between the tubes. The disk are connected to the outer tube and the inner tube alternately creating a meandering path.

Solving the Laplace equation for a magnetic scalar potential ($\nabla^2 V = 0$) for this geometry by assuming ideal diamagnetism of the superconducting material (field orthogonal to the wall of the superconductor $B_{\perp\, sc} = 0$) and introducing an axial current through the CCC, it can be shown that the azimuthal field component $\vec{B}_\varphi(r) = \mu_0 I/(2\pi r)\hat{e}_\varphi$ (e.g. from the beam current) can reach the pick-up volume

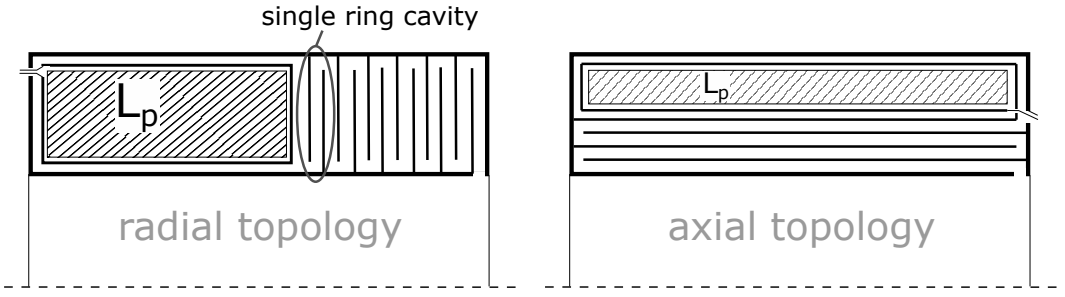

Figure 3.6: *Cross-section of two topologies of the superconducting shield of the CCC: (left) The disk shield (radial meanders) used in the radial design of the CRY–rCCC. (right) The ring shield (coaxial meanders) used in the coreless axial design of the CRY–aCCC.*

without being attenuated [40, 42, 43]. Moreover, all B_Φ field components that are dependent on the radial position of the current within the CCC are strongly attenuated which confirms the independence of the CCC measurement from the precise position of the beam. The same is true for external field components that originate in the measurement environment. Fields are attenuated with a damping factor depending on the effective length l_e of the shield. Larger total height, additional meanders and a bigger difference in the inner and outer diameter – among other parameter – all increase l_e and give an increased shielding factor [43, 44]. The CRY–rCCC is based on this radial design (see Sec. 4.3).

Attenuation values are given for the excitation created by an external dipole field since other components are attenuated more strongly. In this geometry, the dipole attenuation factor A – which is the ratio of magnetic flux densities at the exit and at the entrance ($A = |B_{out}|/|B_{in}|$) – of a single ring cavity, consisting of an inner and an outer disk, can be calculated according to

$$A_{radial} = \left(\frac{R_{out}}{R_{in}}\right)^2 = \left(\frac{h_{gap}}{R_{in}} + 1\right)^2 = \left(\frac{l_e}{2R_{in}} + 1\right)^2 \quad , \tag{3.6}$$

with the inner and outer radius of the volume enclosed by the shield (R_{in}, R_{out}) [40, 43]. The radial height of the shielding volume is $h_{gap} = R_{out} - R_{in}$.

Recent investigations suggest an alternative *coaxial shield* design which is more efficient for shield geometries with a length l that is significantly larger than the radial thickness h_{gap} [10, 11]. This is the case for the CCCs that are planned at FAIR, which have a large inner diameter to accommodate the beam-line and a small radial height in order to reduce the overall size of the setup. In the axial design, instead of using a stack of disks to increase the effective length, additional coaxial tubes that are connected on alternating ends can be stacked radially (see right side of Figure 3.6). This alternative shield design is used for the coreless axial CRY – aCCC (see Sec. 4.4).

The attenuation factor for magnetic fields that are perpendicular to the axis of the CCC for one coaxial layer with the radius r_i and the length l can be estimated with [11, 42]

$$A_{axial,i} = e^{(l/r_i)} \quad . \tag{3.7}$$

For multiple layers, the total screening factor is calculated according to

$$A_{axial} = \prod_i \exp\left(\frac{l}{r_i}\right) = \exp\left(\sum_i \frac{l}{r_i}\right) \approx \exp\left(\frac{l_e}{r_{mean}}\right) \ . \tag{3.8}$$

In principle, the co-axial shielding layers can be added to the inner surface of the shield (like depicted in Fig. 3.6) or to the outside surface. The shielding factor is a bit smaller when the layers are on the outside radius (cf. Eq. (3.8)), but for large diameters of the shield the different is rather small. More importantly, the manufacturing is a bit easier when the shield is placed on the inner radius.

3.4 The high-permeability core

In order to increase the coupling of the SQUID to the beam current, the inductance of the pick-up coil L_p can be increased by either a larger pick-up volume or by a 'magnetic' core with a large magnetic permeability that is used as a flux concentrator. The use of a magnetic core gives the possibility to raise the inductance much more significantly, however it comes with a multitude of consequences for the measurement sensitivity and for the signal background. A list of the effects is given in Tab. 3.1 at the end of this section.

First of all, the relative magnetic permeability $\mu_r(f)$ of the core is a function of the frequency of the applied field (see Figure 3.7 (left)). While the material of the core is selected in a way to have a very linear response throughout the desired measurement bandwidth, at frequencies above 10 kHz the magnetic permeability starts to drop significantly limiting the operating bandwidth of the detector [12]. As a consequence, the flux-to-current calibration factor k of the CCC slightly varies with the frequency of the applied signal, due to the decrease of the magnetic permeability. However, when the focus of interest are dc currents the non-linearity at high frequencies becomes irrelevant.

Moreover, in case the inductance of the high-permeability core L_p is much larger than the small parasitic inductances L_{par} along the pick-up circuit (e.g. of the wire connections), the influence of L_{par} on the current measurement is negligible. Due to the stronger directional coupling of the SQUID to the ring-symmetric magnetic field component created by the beam current, the relative contribution

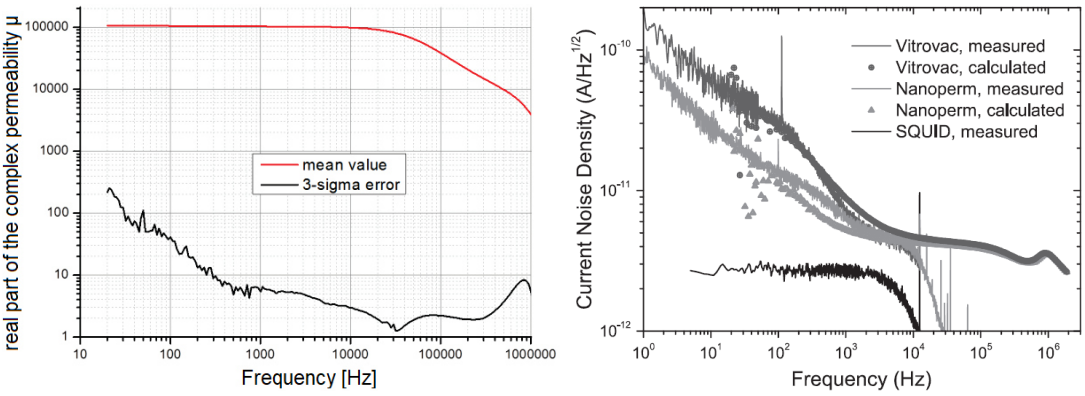

Figure 3.7: *(left) Measurement of the real part of the cryogenic magnetic permeability $\mu(f)$ of the Nanoperm GSI-328plus core used in the CRY–rCCC. The resulting inductance of the pick-up coil is almost constant up to a frequency of* 10 kHz *[45]. (right) Comparative measurement of the cryogenic current noise spectral density of a bare dc SQUID (Magnicon GmbH) and of two different core materials (Vitrovac and Nanoperm) [12].*

of other field directions that enter the system via the parasitic inductances is reduced. As a consequence, the demand on the shielding efficiency of the magnetic shield is lower for a system with a magnetic core to achieve the same signal-to-noise ratio when only external magnetic fields are considered. Moreover, a core material with a high-permeability leads to an impedance (inductance) mismatch between the pick-up coil and the input coil of the SQUID. Thus, an additional flux transformer is required to optimize the coupling of the signal, which makes the design of the pick-up circuit more complex.

However, with the stronger beam coupling due to the core, at the same time the demand on the SQUID readout – to process larger signal slew rates – is increased. The CCC installed at the Antiproton Decelerator (CERN) features a high-permeability core and during the injection of the antiproton beam into the ring the resulting slew rates at the SQUID exceed the bandwidth limit of the active FLL feedback. As a results, the SQUID loses its working point and a baseline correction is necessary. An offset correction can be performed using the zero-current baseline of the empty ring at the end of the accelerator cycle [8].
In contrast, the limitation of the operating bandwidth due to the magnetic core can also be seen as a natural low-pass filter which removes high-frequency perturbations at the natural resonance of the system and which reduces the slew

Frequency & bandwidth	• Frequency dependency of the signal $\mu_r(f)$ [12, 45]. • Limits the operating bandwidth $\mu_r(f)$. • Suppresses high-frequency noise and resonance of pick-up.
Inductance & slew rate	• Increases inductance of pick-up L_p. • Lowers contribution of parasitic inductances L_{par}. • Increases the signal slew rate at the SQUID.
Flux transformer	• Additional flux transformer necessary for impedance matching.
Noise	• Fluctuations of the magnetization adds flux noise [12, 45]. • Increased temperature sensitivity $\mu_r(T)$. • Cause of microphony via magnetostriction.

Table 3.1: *List of parameters which are affected by the presence of a high-permeability core.*

rate of the measured signal. Both effects help to stabilize the operation of the SQUID. In future CCCs, the influence of the core's magnetic permeability can be exploited to shape the frequency response of the system without introducing additional noise (e.g. via the resistor) that comes with an electric low-pass filter.

Although the high-permeability core leads to an increase in the effective amplitude of the signal at the SQUID, it also introduces additional noise to the system (see Fig. 3.7). The magnetization of the core material is subject to thermal fluctuations and – in combination with the discrete reorientation of magnetic spin domains (Barkhausen noise) – the result are low-frequency variations of the magnetic permeability and thus of the measured field. The resulting current noise density of the inductance (detector coil & core material) can be estimated by the fluctuation-dissipation theorem (cf. Fig. 3.7) [12, 41]. For CCCs with a high-permeability core, its contribution becomes the dominant source of noise and limits the achievable current resolution, particularly at low frequencies, which is a significant disadvantage.

Finally, the high-permeability core increases the susceptibility of the CCC to external perturbations. First, the magnetization of magnetic materials is linked to a change of their geometric dimensions and to mechanical stress (magnetostriction). This opens the possibility for mechanical vibrations to be converted into a magnetic field and to directly affect the measurement. This microphony has been observed with CCC systems and is suspected to have its origin in the high-

permeability core [12]. Moreover, a susceptibility of the CCC to changes of the temperature was measured [14], which has its origin in the change of the junction parameter of the SQUID itself [29]. However, there is a contribution by the core as well since its magnetic permeability $\mu(T)$ is variable with temperature. The variation for the core material used in the radial CCC were measured in [45]. Any fluctuation of the temperature will change the magnetization of the core and, in this way, will produce a signal in the SQUID.

In the end, the incorporation of a magnetic core in the system is a complex decision and, in existing CCCs, has resulted in a good measurement stability with a moderate amount of noise. While the goal always was to find the best core material (largest inductance, linearity of μ_r), for a long time the use of a core was never questioned. In recent years, detailed investigations of the noise background has lead to advances in the reduction and characterization of the individual noise contributions [12, 46] and have identified the magnetic core as one of the remaining dominant sources of noise which limits the current resolution of the CCC. Therefore, the removal of the core promises an improvement of the measurement performance of the detector system and needs to be investigated.

Chapter 4

Evaluation of CCC detector systems

The main limitation of the achievable current resolution of the CCC is the noise background of the measurement. In existing CCC beam monitors, the high-permeability 'magnetic' core is a significant source of noise and there is the potential for a substantial increase in the overall signal-to-noise ratio by designing a system that can operate without it. In the past, the construction of a coreless CCC was not feasible for the required detector dimensions, due to the unattainably high demands on the shielding factor and the large intrinsic noise of the available SQUIDs. With the large inner dimensions required to incorporate the accelerator beam-line and with the restrictions on the available detector volume, it has not been possible to realize the required shielding properties to mitigate the effect of parasitic inductances using the radial shielding topology.

However, the recent developments on the axial shield topology offer the possibility to realize the shielding factor which is required for a coreless CCC within the given detector dimensions. Moreover, the construction from sheets of lead – with adequate safety precautions to address the health issues connected with the material – makes it feasible to implement a new detector from the design to the construction in little time. There has been experiments at the Leibniz-IPHT with various prototypes of the axial shield design [10]. However, a direct comparison of the performance of the radial shield with a high-permeability core and of the novel coreless axial CCC in view of the specific measurement task

at CRYRING and at FAIR was never performed. In this chapter, the two detector models are described in detail, followed by a direct comparison of their measurement performance.

4.1 Shield performance

In preparation for the construction of the magnetic shield of the CCC detector for FAIR, simulations of the achievable shielding factor for the different topologies of the shield were performed at TU Darmstadt [11, 43, 44], with the goal to maximize the shielding efficiency for the detector dimensions that are feasible at the beam-line. The two shielding topologies (see Sec. 3.3) were simulated in a 2.5D finite element model and the attenuation factor A of the magnitude of a magnetic dipole field between the entrance of the shield and the position of the pick-up volume was determined as a function of the axial length ℓ and the outer radius R_{out} of the shield. The fixed inner diameter ($D_{in} = 240\,\mathrm{mm}$) together with the outer dimensions (ℓ, R_{out}) determine the volume of the detector. From the available detector volume, the number of shielding layers that can be incorporated were derived, while keeping the cross-section of the pick-up coil (and its inductance) constant at $60\,\mathrm{cm}^2$.

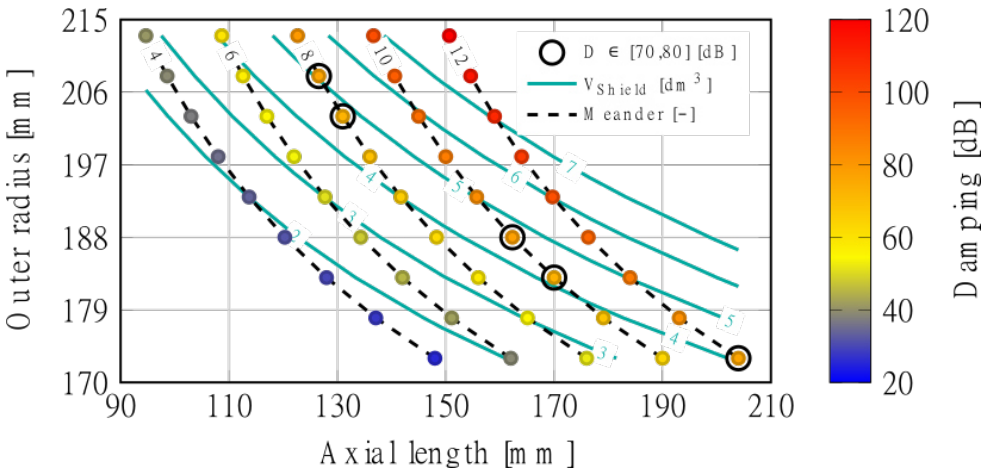

Figure 4.1: *Simulation of the shielding factor of the superconducting shield in the radial topology against a magnetic dipole field for different outer dimensions (outer radius R_{out}, length ℓ) and the resulting number of pairs of shielding disks. Courtesy of N. Marsic (TU Darmstadt) [44].*

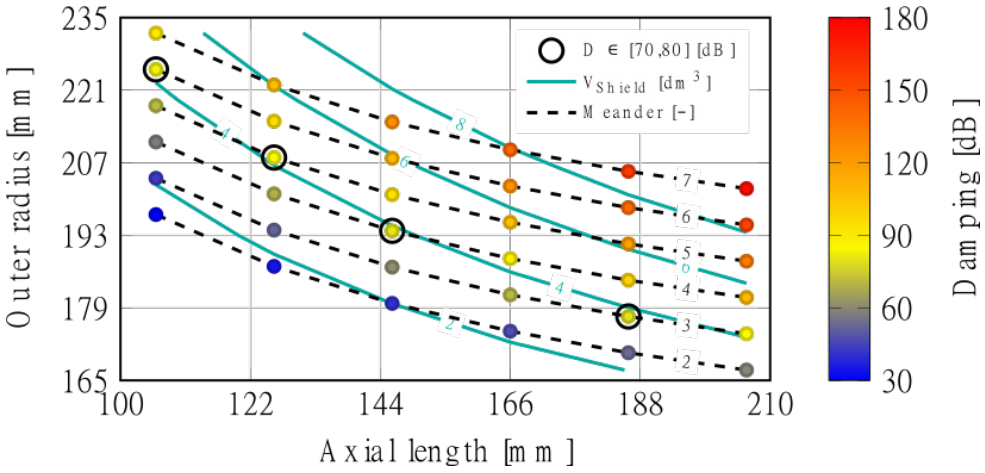

Figure 4.2: *Simulation of the shielding factor of the superconducting shield in the axial topology (shielding layers at R_{in}) for different outer dimensions (outer radius, length) and the resulting number of coaxial shielding layers. The inner diameter ($D_{in} = 240\,mm$) and the cross-section of the pick-up are fixed. Courtesy of N. Marsic (TU Darmstadt) [47].*

For the radial shield topology, Figure 4.1 shows the damping of the magnetic dipole field for different outer radii and total lengths. Dashed black lines give the possible dimensions for a fixed amount of shielding disks (4 to 12 disk pairs). For comparison, different configurations with an identical attenuation factor ($A \approx 75\,\mathrm{dB}$) are marked with a black ring. The geometry of the radial shield for CRYRING (CRY–rCCC) is close to the one marked in the bottom right of Fig. 4.1 with an outer radius R_{out} of 175 mm and an axial length ℓ of 210 mm. However, its inner diameter ($D_{in} = 250\,\mathrm{mm}$) is larger than the one assumed in the simulation, which corresponds to a slightly smaller expected shielding factor than indicated in the simulation. It becomes apparent, that with the radial shield design a significant number of shielding disks (≥ 8) is required to achieve a damping factor that is comparable to the one of previous CCCs ($\geq 75\,\mathrm{dB}$).

In contrast, in the axial design with identical dimensions the number of shielding layers to achieve a similar shielding factor is significantly smaller (see Figure 4.2). Please note that in this simulation the shielding disks are place on the inner radius of the CCC (cf. Sec. 3.3). By considering the outer dimensions of the CRY–rCCC ($R_{out} = 175\,\mathrm{mm}$, $\ell = 210\,\mathrm{mm}$) in Fig. 4.2, the shielding factor of the axial geometry is similar to the radial topology, but only three axial shielding layers are required (see dashed black line for three meanders). A smaller amount

of shielding layers makes the manufacturing process simpler and less prone to errors (e.g. electric contact between layers).

It is important to note that the simulation assumes a construction from niobium, which requires a wall thickness of the material of at least 3 mm and a gap between the layers of 0.5 mm. Thus, each coaxial shielding layer made out of niobium increases the outer diameter D_{out} of the shield by 7 mm. However, with sheets of lead with a wall thickness of 0.25 mm and a gap between layers below 0.45 mm, the increase of the radius due to one shielding layer is below 0.7 mm, which corresponds to an increase of the diameter of 1.4 mm. Therefore, five times as many additional layers can be installed without increasing the outer radius (or decreasing the pick-up volume) when using lead as the construction material. In this way, much larger shielding factors are possible. The three coaxial layers of niobium, with a total radial thickness of 10.5 mm, can be replaced by 15 layers of lead, which results in a shielding factor A of about 218 dB at identical outer dimensions (cf. Eq. (3.8)).

The simulations confirm the analytical estimate that a significantly larger shielding factor can be achieved in the axial design for the detector dimensions that are available at the beam-lines at CRYRING and at FAIR. This result is the basis for the subsequent design and construction of the axial superconducting shield.

4.2 CCC test bench

To allow a direct comparison, both CCC detector models were tested at the same test bench at University Jena. In addition, there exists a very similar setup at GSI which was used to validate the CCC before it was installed at the beam-line. Figure 4.3 provides an overview of the experimental setup.

The setup consists of a wide-neck helium-bath cryostat in which the CCC rests on a non-conductive platform made of fiberglass. The distance between the SQUID and the pre-amplifier of the FLL electronics is roughly 1 m. A wire loop through the CCC carries a calibration current I_{cal} to simulate the beam current (see Fig. 4.3). Arbitrary current signals with different waveforms can be applied to characterize the detector (e.g. the beam current sensitivity and the bandwidth

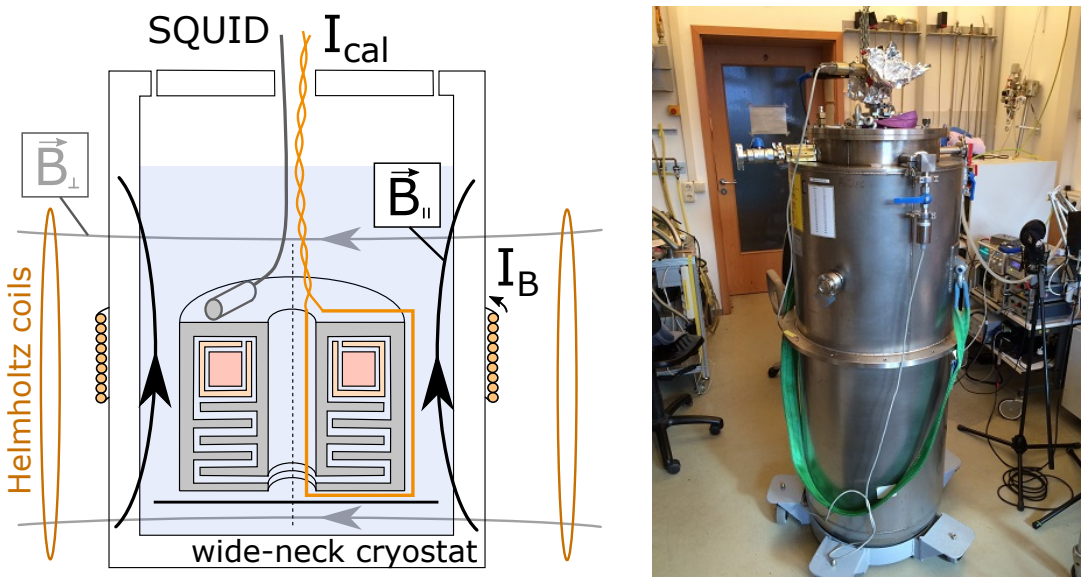

Figure 4.3: *Test bench at University Jena for characterization of different CCC models. The CCC is placed on a platform inside a wide-neck helium-bath cryostat. A beam current is simulated with by the calibration current I_{cal} through a wire loop.*

limits). Furthermore, a Helmholtz coil can be placed around the cryostat and is used to apply a magnetic field $\vec{B}_\perp$ that is orthogonal to the axis of the CCC. A second coil is wound around the cryostat to create a magnetic field $\vec{B}_\parallel$ that is parallel to the axis of the CCC. With these fields the magnetic shielding factor A of the superconducting shield can be determined.

For the experiment, the CCC is cooled down inside the cryostat and requires several days to reach a thermal equilibrium. During this time, the discrete jumps of the magnetization of the high-permeability core (cf. Barkhausen noise) – as it settles on an equilibrium temperature – lead the SQUID to spontaneously lose its working point and makes long-term measurements impossible. Note, that these flux jumps are caused by an unlocking of the electronics and thus do not necessary have an amplitude which is equivalent to multiple magnetic flux quantum. As the system is approaching the thermal equilibrium, the interval between these jumps increases with the cryogenic standing time until the probability is very low that a large jump of the magnetization will appear during a measurement of several minutes.

In order to provide reproducible measurement conditions, the cryostat is placed inside a magnetically shielded room at University Jena in order to minimize ex-

ternal magnetic perturbations and to enable a valuable comparison between different CCC models. Acoustic and mechanical perturbations can not be shielded as easily. Therefore, comparative measurements were performed during the night when these noise sources are at a minimum. The noise background in these measurements was usually very low. It allows to determine the intrinsic detection limits defined by the spectral current noise density of the detector. To this purpose, the fluctuations of the signal baseline are measured for several minutes to obtain a spectral current noise density, either directly with a spectrum analyzer or via a Fourier transformation of the signal collected in the time domain. While these measurements are aimed to make conclusions about the best possible instrument performance, at the accelerator the noise figures are expected to be significantly higher which will deteriorate the current resolution and the signal-to-noise ratio of the CCC. The susceptibility of the detector to these external perturbations ultimately determines the precision of the measurement.

4.3 Radial topology

The CCC for CRYRING in the radial design (CRY–rCCC) was completed at University Jena in 2017 and required a significant increase in size compared to previous models to accommodate the diameter of the beam-lines at FAIR of 150 mm. The inner diameter had to be increased by 35 % which decreases the efficiency of the superconducting shield. It follows the traditional topology suggested by Grohmann *et al.* [40] and has a disk shield made from niobium with a total of 12 pairs of radial meanders (see Figure 4.4). The length $\ell = 210\,\mathrm{mm}$, the inner diameter $D_{in} = 250\,\mathrm{mm}$ and the outer diameter $D_{out} = 350\,\mathrm{mm}$ are a compromise between maximizing the shielding efficiency and reducing the required space along the accelerator beam-line. The cryogenic support system was designed in a way to accommodate these detector dimensions.

4.3.1 Construction and design

The individual parts that form the shielding structure need to be connected in a way to form one solid superconductor without any pinholes that would deteriorate the shielding efficiency. The inner and outer niobium disks have two slightly

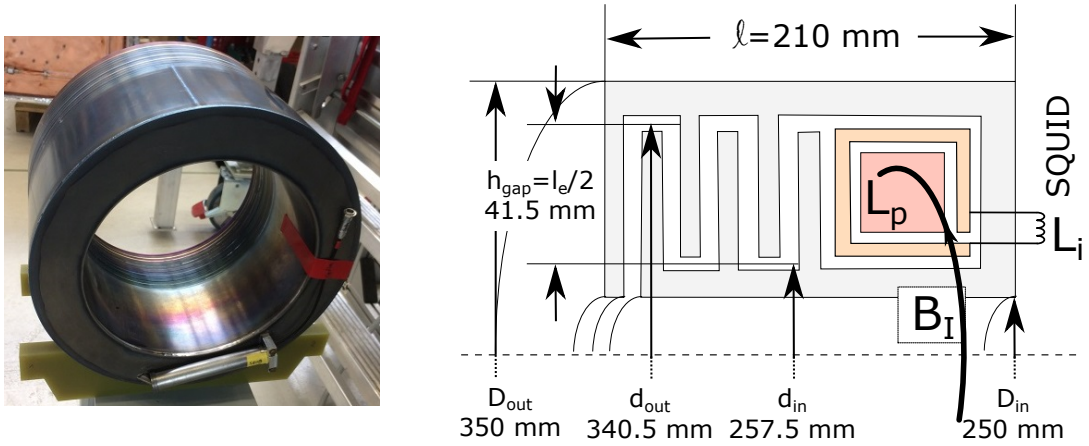

Figure 4.4: *(left) The CRY–rCCC before installation inside the cryogenic support system. (right) Schematical cross section of the radial shield topology. Not all* 12 *individual shielding meanders are depicted.*

different diameters and are stacked consecutively on top of each other, each separated by a sheet of fiberglass. Figure 4.5 documents the construction process. All disks with a larger outer diameter are connected with electron-beam welding along the outer circumference of the shield, while the disks with the smaller inner diameter are connected in the same way on the inner circumference of the shield. After the assembly of the shielding disks, there was an electrical short between the inner and outer disks that was removed by applying a large current which locally melted the metal that produced the electric bypass [48].

With the given dimensions of the meanders of $d_{in} = 257.5\,\mathrm{mm}$ and $d_{out} = 340.5\,\mathrm{mm}$, the dipole shielding factor A for the total of 12 disk pairs can be estimated based on Eq. (3.6) according to

$$A_{radial} = 20\log\left(\frac{B_{out}}{B_{in}}\right) = \prod_{i=1}^{12} A_{radial,i} = \prod_{i=1}^{12}\left(\frac{d_{out}}{d_{in}}\right)^2 \approx 58\,\mathrm{dB}\ . \tag{4.1}$$

The inductance L_p of the single-turn niobium pick-up coil is determined primarily by the nano-crystalline high-permeability core. At 4.2 K the inductance is between 10 and 100 µH up to a frequency of 100 kHz with an average inductance of 80 µH taken at 1 kHz (see Fig. 3.7) [12, 45]. Because of the large inductance of the core ($L_p \gg L_{par}$), any small parasitic inductance (e.g. of the wires) can be neglected. The signal of the pick-up coil is coupled to a single-stage dc SQUID

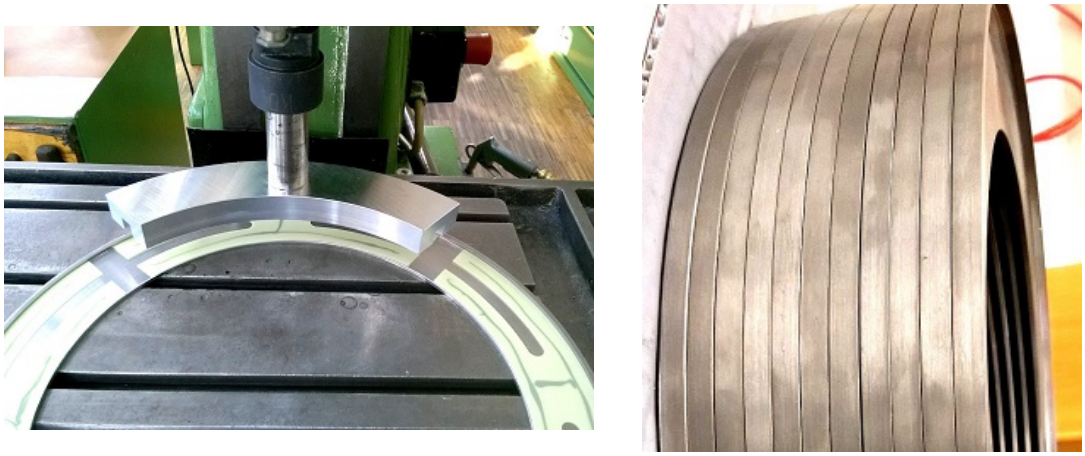

Figure 4.5: *(left) Installation of fiberglass spacers between the individual niobium shielding disks of the CRY–rCCC. (right) Assembled stack of shielding disks before welding. Both images courtesy of University Jena.*

from the Magnicon GmbH[1] with an input inductance of $L_i = 1\,\mu\text{H}$ via a flux transformer. See Table 4.1 for an overview of the CCC parameter.

All the components of the flux transformer were selected to optimize the impedance matching ($L_{t2} = L_i = 1\,\mu\text{H}$, $L_{t1} = L_p = 80\,\mu\text{H}$) (cp. Sec. 3.2). Figure 4.6 shows the resulting transfer function between the applied (beam) current I_a and the current I_{T2} through the input inductance of the SQUID in case of a matched coupling based on the flux transformer as well as for direct coupling. At frequencies smaller than roughly 100 kHz, the flux transformer leads to an increase of the magnitude of the current by a factor of $I_{T2}/I_a = 2.95$ (9.5 dB).

In addition to the general amplification of the signal, the flux transformer attenuates (and slightly shifts) the natural resonance of the pick-up circuit, which is necessary for a stable operation of the SQUID. A strong resonance can impair the stability of the FLL operation and generally should be avoided. Moreover, the effect of the decreasing magnetic permeability $\mu_r(f)$ of the core material at frequencies above roughly 10 kHz [12, 45] further dampens the resonance and stabilize the system. With the direct coupling of the SQUID to the pick-up coil, the resonance frequency f_0 of the pick-up circuit is dominated by the capacity of the shielding structure ($C_{shield} = 44\,\text{nF}$ [45, 48]) and by the input inductance

[1] 1-stage Current Sensor C5XL1W from Magnicon GmbH, 22339 Hamburg, Germany

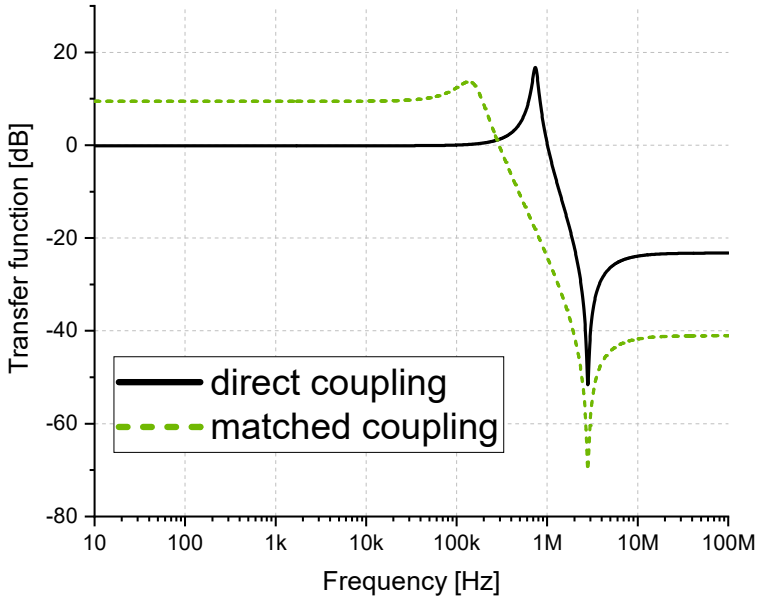

Figure 4.6: *The transfer function between the applied (beam) current I_a and the current I_{T2} at the input inductance L_i of the SQUID as a function of frequency simulated with LTspice. The transfer function is given for the direct coupling of the pick-up coil ($L_p = 80\,\mu$H) to the SQUID L_i (solid black) and for the coupling via a flux transformer (dashed green).*

of the SQUID ($L_i = 1\,\mu$H) according to

$$f_0 = \frac{1}{2\pi\sqrt{L_i C_{shield}}} \approx 760\,\text{kHz}\ . \tag{4.2}$$

However, with the flux transformer, the natural resonance moves to a frequency of 170 kHz (see Fig. 4.6). Frequencies larger than the resonance are attenuated which – together with the reduced magnetic permeability of the core – limit the bandwidth of the CCC system [27].

In addition to the external wire loop, the CRY–rCCC is equipped with an internal calibration line (single wire) embedded below the superconducting shield. The calibration line is accessible through a dedicated connector and can be used to adapt the frequency response of the pick-up circuit (e.g. by the installation of additional signal filters) even after the CCC was assembled and was installed inside the cryogenic support system.

4.3.2 SQUID parameter

The dc SQUID from the Magnicon GmbH is operated with a FLL electronics in current bias mode using the additional positive feedback (APF) method to increase the SQUID transfer function ($V_\Phi = |\partial V_{sq}/\partial \Phi_a|$) and to suppress intrinsic noise contributions. The readout consists of a FLL module containing the pre-amplifier and the integrator – which is mounted directly to the cryostat as close to the SQUID as possible – and of a control unit, which can be placed at a distance of up to 20 m from the FLL module. The data sheet of the SQUID model is attached in the appendix A.3. More details on SQUIDs from the Magnicon GmbH can be found in [33, 49]. A detailed setup routine for the working point of the SQUID is given in the appendix, together with an overview of the control software (see Figure A.2).

After the assembly of the CCC, the basic SQUID parameters were validated experimentally. The operating bandwidth and the maximum signal slew rate of the SQUID can be determined with a test current through the feedback coil of the FLL system. For the characterization of the SQUID, the FLL feedback is deactivated and the voltage V_{sq} at the SQUID is read out directly. Figure 4.7 shows the periodic voltage modulation V_{sq} in reaction to a magnetic flux Φ_a created by a drive current through the feedback coil $I_\Phi^{(\mathrm{fb})}$. The optimal working point, which minimizes the current noise of the SQUID and maximizes the possible slew rate of the system, is the combination of I_b and Φ_a that maximizes the SQUID transfer function $|\partial V_{sq}/\partial \Phi_a|$ (see Sec. 2.3). During the characterization, a maximum transfer function of

$$V_\Phi = |\partial V_{sq}/\partial \Phi_a| = 14.4\,\mathrm{mV/\mu A} = 318\,\mathrm{\mu V}/\Phi_0 \ , \tag{4.3}$$

was achieved with a bias current $I_b = 9.452\,\mathrm{\mu A}$. The value of the transfer function was obtained by a linear fit to the slope of the modulation (green line in Fig. 4.7), taking into account the signal amplification by the pre-amplifier by a factor 2000 and the mutual inductance M_f (see below).

The mutual inductance M_f of the SQUID and of the feedback coil can be determined from the period of the SQUID voltage modulation. According to Eq. (2.17) and (2.18), the modulation depicted in Fig. 4.7 has a period of

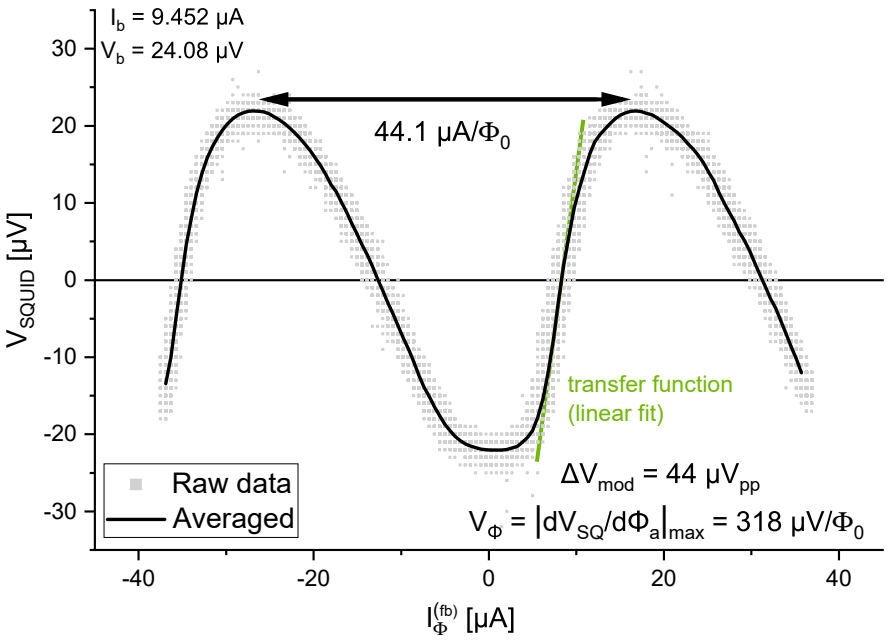

Figure 4.7: *The modulation of the voltage across the SQUID V_{sq} with a current through the feedback coil $I_\Phi^{(fb)}$. The bias current I_b is selected such that the transfer function V_Φ (green line) at the working point is maximized. Data collected inside the wide-neck cryostat at GSI.*

one magnetic flux quantum Φ_0. Thus, the current $I_\Phi^{(\mathrm{fb})}$ through the feedback coil which produces one magnetic flux quantum at the input inductance of the SQUID was equal to

$$\frac{1}{M_f} = 44\,\mu\mathrm{A}/\Phi_0\ . \tag{4.4}$$

The transfer function and the mutual inductance determine the signal gain G_{SQUID} of the SQUID between the FLL system output V_{FLL} and the input to the pre-amplifier V_{sq} with a given feedback resistor R_f [29]. For the Magnicon FLL electronics, the feedback resistor R_f can be varied between 0.7 and 100 kΩ during the measurement. For a feedback resistor of 10 kΩ, in the middle of the parameter range, this leads to a gain of, e.g.

$$G_{\mathrm{SQUID}} = \frac{V_{sq}}{V_{\mathrm{FLL}}} = \frac{V_\Phi M_f}{R_f} = 7.2 \times 10^{-4} \quad \text{with} \quad R_f = 10\,\mathrm{k}\Omega\ . \tag{4.5}$$

The 3 dB-bandwidth $f_{3\,\mathrm{dB}}$ is an estimate of the highest frequencies that the FLL feedback system can track without significant errors. In an idealized system, it is

solely determined by the signal gain G_{SQUID} and by the gain-bandwidth-product (GBP) of the pre-amplifier and the integrator. During the measurement, the gain-bandwidth-product can be set in a range between 0.23 and 7.2 GHz which result in a minimum and maximum bandwidth of, e.g.

$$\begin{aligned} f_{3\,\mathrm{dB}} \geq f_1 = G_s \times GBP &= 5.2\,\mathrm{MHz} \quad \text{with} \quad GBP = 7.2\,\mathrm{GHz} \\ &= 166\,\mathrm{kHz} \quad \text{with} \quad GBP = 0.23\,\mathrm{GHz}\ , \end{aligned} \tag{4.6}$$

for $R_f = 10\,\mathrm{k\Omega}$. While a higher bandwidth is not required to track slow variations of the dc beam current, the SQUID has to be capable to follow fast perturbation signals without losing its operating point [49]. Using the parameter set that allows a stable operation of the CCC at CRYRING, for an idealized system – which is not limited by loop delay or broadband noise – the maximum unity-gain frequency f_1 is 41 MHz with the lowest standard feedback resistor $R_f = 0.7\,\mathrm{kHz}$ and $GBP = 4\,\mathrm{GHz}$. However, a large unity-gain frequency does not always result in an high system bandwidth.

In practice, the bandwidth of the SQUID system is limited by the loop delay ($t_d \approx 20\,\mathrm{ns}$) of the measurement lines and is confined to a maximum possible bandwidth of around 9 MHz (cf. Eq. (2.20)). A small further reduction of the maximum bandwidth due to additional delay in the amplifier or depending on the usable flux range is likely. Assuming a maximum system bandwidth ($f_{3\,\mathrm{dB,\,max}}$) of 9 MHz, this value can be achieved with a unity-gain frequency f_1 of

$$f_1 = f_{3\,\mathrm{dB,\,max}}/2.25 \approx 4\,\mathrm{MHz}\ . \tag{4.7}$$

During the measurement, the combination of R_f and GBP – taking into account the achievable value for the transfer function V_Φ – need to be selected accordingly, to have a unity-gain frequency close to the optimal value. Larger values of GBP lead to an increase in noise and to instabilities of the working point (cf. Sec. 2.3.1).

Furthermore, the loop delay limits the maximum theoretical slew rate of the system $\dot{\Phi}_{f,\,\mathrm{max}}$ to [29, 32]

$$\dot{\Phi}_{f,\,\mathrm{max}} \lesssim \Phi_0 f_1 = \frac{\Phi_0}{4\pi t_d} = 4\ \Phi_0/\mu\mathrm{s} \approx 400\,\mathrm{nA/\mu s}\ . \tag{4.8}$$

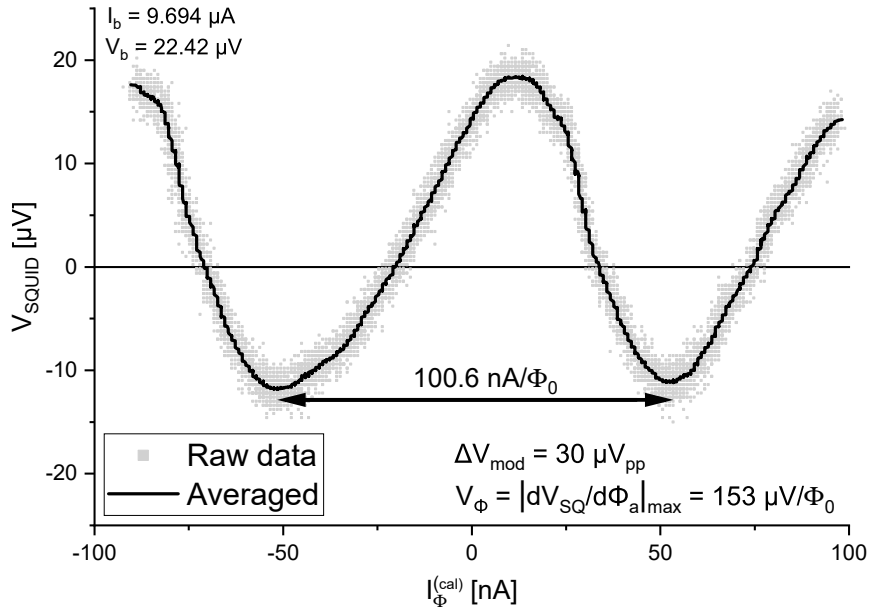

Figure 4.8: *Periodic modulation of the voltage V_{sq} across the SQUID with an applied current $I_\Phi^{(cal)}$ through the calibration line. Data collected inside the beam-line cryostat at the laboratory at GSI. There the amplitude of the modulation (and thus V_Φ) is reduced (cf. Chap. 5).*

The slew rate in terms of flux per µs was converted to the maximum change in current using the mutual beam inductance M_a (see below).

Finally, the sensitivity of the assembled CCC system with respect to the beam current was determined with a test current through the calibration wire, instead of using the internal feedback coil of the SQUID. The voltage variation V_{sq} of the SQUID with the applied current $\mathrm{I}_\Phi^{(cal)}$ is shown in Figure 4.8. For the CCC installed inside the beam-line cryostat, a current along the calibration line of

$$\frac{1}{M_a} \approx 100.6\,\mathrm{nA}/\Phi_0 \quad \text{for} \quad f \lesssim 10\,\mathrm{kHz}\ , \tag{4.9}$$

produced a flux of one magnetic flux quantum Φ_0 inside the SQUID. M_a is the so-called mutual beam inductance. The given value is valid for frequencies below 10 kHz at which the magnetic permeability of the core can be assumed to be constant.

4.3.3 Shielding factor

In order to confirm the estimated shielding factor A against external magnetic dipole fields [44], a known static magnetic field was applied laterally to the axis of the CCC. The response of the CCC was converted to a value for the measured magnetic field B_{in} at the pick-up coil inside the superconducting shield using the law of Biot-Savart (Eq. (2.1)), which then could be compared to the known field applied by the Helmholtz coils B_{out}.

In this way the attenuation factor was determined to be [50]

$$A_{radial} = \frac{|B_{out}|}{|B_{in}|} = 75\,\mathrm{dB}\ . \tag{4.10}$$

This is larger than expected from the theoretical estimate. The reason for the discrepancy could be an overestimation of the field of the Helmholtz coils at the position of the CCC, which would lead to an increase of the calculated shielding factor. The wide-neck cryostat surrounding the CCC can shield part of the applied field and produce the measured effect.

Overall, the magnetic shielding factor of the radial shield is rather low and makes the CCC susceptible to magnetic interference (e.g. from a neighboring dipole magnet).

4.3.4 Noise current spectral density

The spectral noise current density of the CCC measurement can be split into three components: the intrinsic noise of the SQUID (cf. Eq. (2.19)), the intrinsic noise of the high-permeability core of the pick-up circuit (see Sec. 3.4) and the external noise imposed by the environment. Figure 4.9 shows the current noise spectrum of the CRY–rCCC obtained inside the magnetically shielded room at University Jena, where the external noise component can be strongly suppressed.

The intrinsic noise of the single-stage dc SQUID (Magnicon C5XL1W) consists of the flux noise density of the SQUID of $\sqrt{S_\Phi} = 1$ to $2\,\mu\Phi_0/\sqrt{\mathrm{Hz}}$ (at 1 Hz – 50 kHz) and the white voltage noise density of the pre-amplifier of $0.33\,\mathrm{nV}/\sqrt{\mathrm{Hz}}$ (see datasheet of the SQUID in the appendix A.3). Using the transfer function of $V_\Phi = 318\,\mu\mathrm{V}/\Phi_0$, the amplifier noise can be converted to a flux noise according to

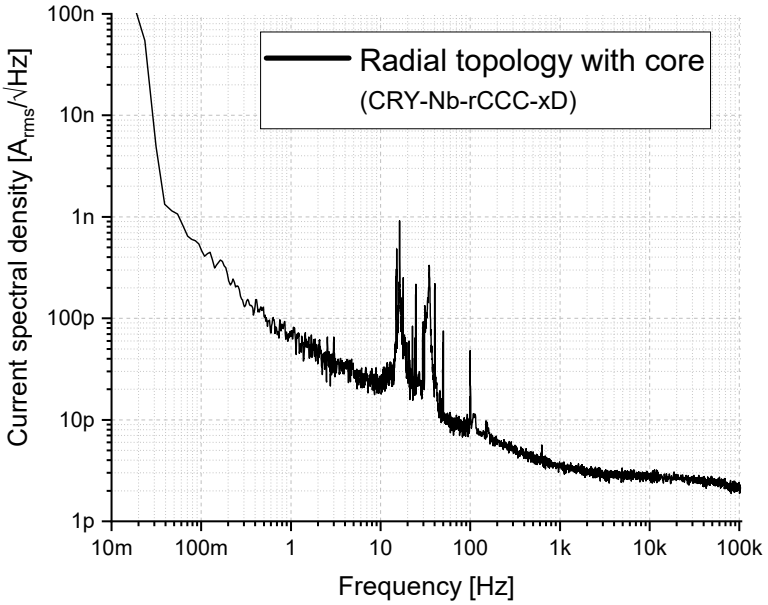

Figure 4.9: *The noise current spectral density (rms) of the radial CCC measured during the night in the magnetically shielded room at university Jena after three days at cryogenic temperatures. Mechanical perturbations between* 10 Hz *and* 100 Hz *and the noise of the high-permeability core are the prominent sources of noise. Data courtesy of V. Tympel at University Jena.*

$\sqrt{S_{\Phi,\,\mathrm{AMP}}} = \sqrt{S_{V,\,\mathrm{AMP}}}/V_\Phi$. The result is a total noise density of the bare SQUID below $3\,\mu\Phi_0/\sqrt{\mathrm{Hz}}$ at frequencies above 1 Hz, which translates to a current noise of $0.3\,\mathrm{pA_{rms}}/\sqrt{\mathrm{Hz}}$ or less. The mutual beam coupling $1/M_a \approx 100\,\mathrm{nA}/\Phi_0$ was used to convert the flux noise to a current noise. The contribution of the current noise of the amplifier was neglected. At very low frequencies ($f \leq 1\,\mathrm{Hz}$) the intrinsic noise of the SQUID increases to $1\,\mathrm{pA_{rms}}/\sqrt{\mathrm{Hz}}$ at a frequency of 0.1 Hz, following a $1/f^\alpha$-distribution. However, the noise contribution by the SQUID across the entire operating range of the CRY–rCCC ($\leq 200\,\mathrm{kHz}$) is much lower than the measured noise level (cf. Fig.4.9), which confirms that the detector resolution is not limited by the SQUID but by other effects.

In general, the flux noise from the high-permeability core – described by the fluctuation-dissipation theorem – dominates the noise spectrum of the CCC. The current noise density (cf. Fig. 4.9) is well described by the measurements of the noise of the magnetic core itself (cf. Fig. 3.7) [12]. On top of the noise of the core, there are several additional contributions which are specific to a certain frequency range and some of which exhibit strong variations with time.

At low frequencies (< 1 Hz), slow variations of the operating temperature of the liquid helium bath – which is connected to the vapor pressure above the helium bath – affect the signal and increase the noise density. At intermediate frequencies between 10 Hz and 100 Hz the CCC is sensitive to acoustic and mechanical perturbations from the environment (microphony), which are visible as prominent peaks at discrete noise frequencies. Detailed investigations at University Jena and at GSI could identify most of the noise sources (e.g. vacuum pump, air conditioner unit, etc.), which often makes a targeted reduction of the contributions possible (see Sec. 5.2.1) [48].

At high frequencies between 1 kHz and 200 kHz (the maximum bandwidth of the pick-up circuit), the surrounding cryostat forms a Faraday cage and shields the ambient electromagnetic field. The remaining high-frequency current noise was almost constant with a noise density of $3\,\mathrm{pA_{rms}}/\sqrt{\mathrm{Hz}}$ and is a combination of the magnetization noise from the high-permeability core and of Johnson-Nyquist (thermal) noise (cf. Eq. (1.1)) of electrical conductors inside the sensitive area.

The direct comparison of the spectral current density of the CRY–rCCC and the measured current density of the high-permeability core (see Fig. 3.7) makes it clear that the intrinsic current noise is dominated by its high-permeability core and that a removal of the core can lead to a significant improvement of the achievable current resolution.

4.4 Axial coreless topology

The CCC in the coreless axial shield design (CRY–aCCC) was constructed in 2019 in collaboration with the Leibniz Institute of Photonic Technology in Jena (Leibniz IPHT)[2], specifically for the use at CRYRING. Leading up to this model, a series of prototypes were designed and built at Leibniz IPHT. However, the two alternative detector topologies never were compared in detail.

The CRY–aCCC uses the axial shield topology with 12 coaxial screening layers made from lead placed at the inner diameter (see Figure 4.10). It has almost the same radial dimensions as the radial CCC ($D_{in/out} = 251.2\,\mathrm{mm}/350\,\mathrm{mm}$), but an increased length of 292.8 mm. There is no high-permeability core, which

[2] Quantum Systems Department, Leibniz Institute of Photonic Technology (Leibniz IPHT), 07745 Jena, Germany

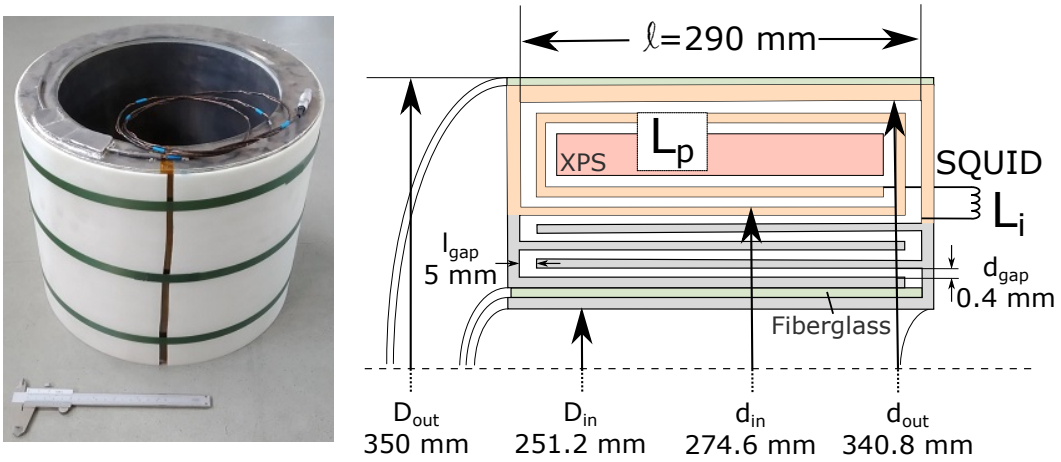

Figure 4.10: *(left) Photograph of the coreless CRY–aCCC. (right) Schematical cross section of the axial shield topology. The pick-up coil is highlighted in beige. Not all* 12 *individual shielding screens are depicted.*

leads to a significantly smaller beam coupling and, subsequently, makes the system much more susceptible to noise that couples in via parasitic inductances. Therefore, the reduction of the pick-up inductance needs to be compensated by a larger shielding factor and by a low-noise SQUID system. The advantages are an elimination of the flux noise of the core material and the possibility to track larger slew rates due to the smaller amplitude of the signal at the SQUID.

So far, only a few prototypes in the axial shield topology have been constructed and the manufacturing process can still be improved to obtain a better noise performance. Therefore, several adaptations of the construction process were implemented to measure their effect on the noise spectrum of the detector:

First, the inductance of the pick-up was increased with a nested two-turn pick-up coil in order to improve the SNR of the current signal. Second, a 2-stage SQUID system was installed to enhance the transfer function V_Φ of the readout, which consisted of a primary SQUID detecting the beam current and a secondary SQUID which was used as a ultralow-noise amplifier [51]. Third, the mechanical rigidity of the shield and of the pick-up was increased in order to combat the susceptibility to mechanical and acoustically introduced noise. Any relative movement of the layers of the shield or of the pick-up creates a change of the capacity and of the inductance, which was thought to be a major coupling mechanism of perturbations.

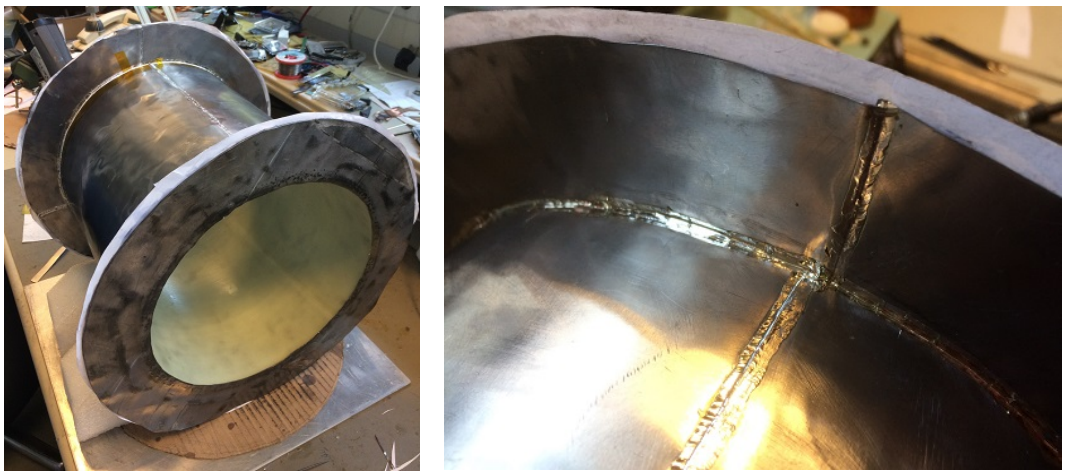

Figure 4.11: *Photographs of the CRY–aCCC during the construction. (left) The first screening ring is glued to the inner fiberglass support tube. (right) Close-up view of the soldering connection that has to form a superconducting interface between the lead sheets that is free of any pinholes.*

4.4.1 Construction and design

The manual construction of a CCC in the axial design relies on lead as the building material, since it is easy to obtain, to shape and to form stable superconducting interfaces between different parts. Lead as a construction material is very soft and will lose its form with time due to creep without a stable support structure. Therefore, the assembly is supported by a tube ($\ell_{\mathrm{FRP}} = 290\,\mathrm{mm}$) made of fiberglass-reinforced plastic (FRP) on the inner diameter and is protected by a similar tube that surrounds the assembled CCC at the outermost diameter (see Fig. 4.10). FRP offers a high mechanical stability at a very low weight and can be used in a cryogenic environment. Figure 4.11 shows the CCC during the construction.

On the inner radius of the tube of FRP, a sheet of pure lead, with a thickness of 1.4 mm, is glued to the surface and forms the innermost layer of the superconducting shield. Similarly, all surfaces on the outside of the shield (outermost diameter and end-caps) are made of pure lead. However, the individual inner shielding layers – which form the 12 screens of the shield – consist of hard lead foils (97.5Pb-2.5Sn) with a reduced thickness of 0.25 mm. The shielding layers each have a length ($\ell_{screens} = 285\,\mathrm{mm}$) which is slightly shorter compared to the overall inner length of the shield ($\ell = 290\,\mathrm{mm}$). Each layer is soldered only to

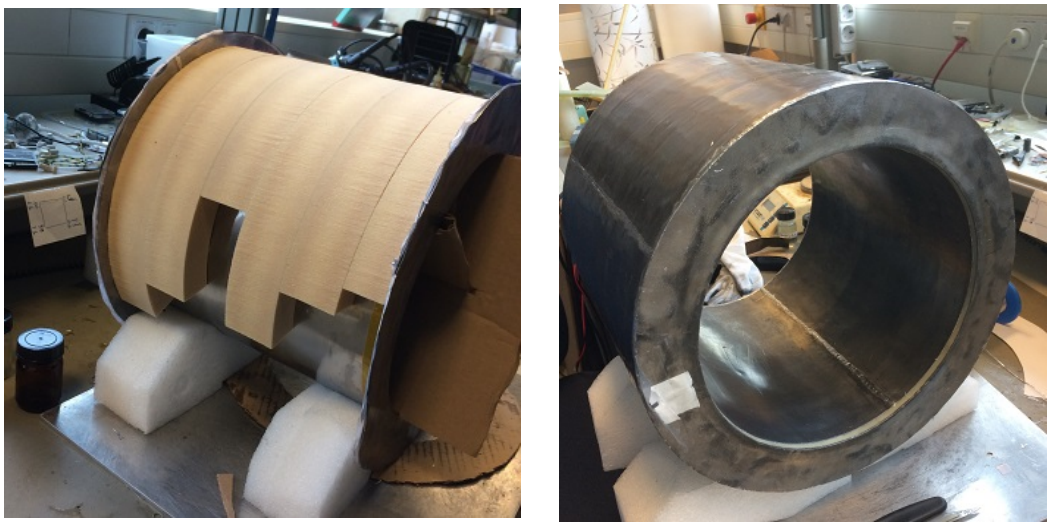

Figure 4.12: *Photographs of the coreless CRY–aCCC during the construction. (left) The pick-up volume is filled with XPS. (right) The shield is completed and the connecting wires are prepared for the connection of the SQUID.*

one end-cap and thus leaves a gap ($l_{gap} = 5\,\mathrm{mm}$) to the wall on the opposite end for the ring-symmetric magnetic field of the beam to enter. Consecutive layers have their gap at opposing ends and create a meandering path, thereby increasing the effective length l_e of the shield (see Fig. 4.10).

A soldering agent based on lead (60Sn-40Pb) guarantees a superconducting interface between the individual sheets. In this way, the screening sheets and the wall form one solid superconductor. The right side of Fig. 4.11 shows the interface between two sheets of lead after soldering. Sometimes bubbles or holes form along the seam during the soldering process. These can form pinholes in the superconducting shielding and must be identified and removed before subsequent layers are installed. A strip of polyimide foil (Kapton) is placed below the soldering seam of two layers to protect the underlying layers from the heat of the soldering process.

In addition, each sheet is separated radially by a non-conductive layer (a sheet of printing paper) with a thickness of roughly 0.1 mm and is connected to the next layer with epoxy glue type L to form a rigid connection. This bonding of the individual layers has the goal to prevent relative motion. It increases the overall stability of the lead construction and, in this way, reduces the sensitivity to microphonic perturbations. After the assembly, the average gap between the

separate layers was estimated to be around $d_{gap} = 0.4\,\mathrm{mm}$. Based on Eq. (3.8), the expected screening factor A can be calculated – using a mean radius of the screening layers of $r_{mean} \approx 133\,\mathrm{mm}$ and the effective number of shielding screens of $N_{sc} = 12$ – according to

$$A_{axial} = \exp(\sum_{i=1}^{N_{sc}} \frac{l}{r_i}) \approx \exp(\frac{l_e}{r_{mean}}) = 219\,\mathrm{dB}\,, \tag{4.11}$$

with the effective length $l_e = N_{sc} \times (l - 2l_{gap}) = 12 \times 280\,\mathrm{mm}$ [11].

In the radial design, the pick-up coil is a superconducting torus that is enclosed inside (and electrically separated from) the superconducting shield. In contrast, in the axial design the superconducting inner surface of the walls of the shield and of the last screening layer form the pick-up coil (see beige section of the shield in Fig. 4.10). This eliminates the need for a separate pick-up structure. In order to increase the inductance of the pick-up coil, the last screening layer was extended to produce a nested two-turn pick-up coil (cf. Fig. 4.10). By raising the inductance of the pick-up, while keeping the same value for any parasitic inductance, the relative strength of any parasitic effects is decreased.

The entire volume between the last screening layer and the inner surface of the wall was filled with extruded polystyrene (XPS) for mechanical support (see Fig. 4.12). XPS is a lightweight cryo-compatible plastic with closed pores to prevent contamination of liquid helium with trapped water or gases and to avoid damage connected to the freezing of the water. The assembled pick-up structure extends over a diameter (d_{in}/d_{out}) of 275.4 mm/340 mm and stretches across the inner length of the shield ($\ell = 290\,\mathrm{mm}$). With the given dimensions and assuming a relative magnetic permeability ($\mu_r = 1$), the inductance of the pick-up coil with the number of turns $N = 2$ can be estimated according to [10]

$$L_p \approx N^2 \times \frac{\mu_0 \mu_r \ell}{2\pi} \ln\left(\frac{d_{out}}{d_{in}}\right) = 4 \times 12.2\,\mathrm{nH} \approx 50\,\mathrm{nH}\,. \tag{4.12}$$

Looking at Eq. (4.11) and (4.12), during the design of a CCC, the overall length ℓ and the radial height ($\Delta R = R_{out} - R_{in}$) should be maximized in order to increase both the shielding factor and the pick-up inductance for a maximum signal-to-noise ratio.

Sources of parasitic inductances are the coaxial screening layers of the superconducting shield and the wiring of the pick-up circuit: The first parasitic inductance of the coaxial sheets of the shield L_{par1} can be estimated using $R_{in}^{(screens)} = 130\,\mathrm{mm}$ and $d_{gap} \approx 0.4\,\mathrm{mm}$ to be [10]

$$L_{par1} \approx \frac{\mu_0 \pi d_{gap}}{4\ell} R_{in}^{(screens)} \approx 0.2\,\mathrm{nH}\ . \tag{4.13}$$

A small hole on the end-cap of the shield carries the niobium wires that connect the pick-up coil to the input inductance of the SQUID. The second parasitic inductance of this superconducting wire connection is known from similar setups and is in the order of $L_{par2} \approx 6\,\mathrm{nH}$ [10].

In order to optimize the signal coupling to the SQUID, its input inductance L_i should match the inductance of the pick-up circuit L_p (including the parasitic inductance) according to $L_i = L_p + L_{par}$ (cf. impedance matching in Sec. 3.2). Therefore, a supracon Model CN4 2-stage dc SQUID[3] with an input coil inductance $L_i = 44\,\mathrm{nH}$ was selected and is directly coupled to the pick-up circuit (see Tab. 4.1).

With the input inductance L_i of the SQUID and the measured capacity of the shield ($C_{\mathrm{shield}} = 413\,\mathrm{nF}$), the resonance frequency f_0 of the pick-up circuit was estimated to be

$$f_0 = \frac{1}{2\pi\sqrt{L_i C_{\mathrm{shield}}}} \approx 1.2\,\mathrm{MHz}\ , \tag{4.14}$$

which needs to be damped with an adequate filter in order to guarantee a stable operating point of the SQUID. A LC-filter with $R = 0.5\,\Omega$ and $C = 330\,\mathrm{nF}$ provides a good compromise between the damping of the resonance and the additional noise input due to the thermal noise of the resistor. The simulated transfer function between the input and the output current of the pick-up circuit as well as the expected contribution to the spectral current noise density are given in Figure 4.13. The simulation shows that the resonance peak in the transfer function is strongly attenuated by the signal filter. However, the resistor adds a significant amount of white (Nyquist-Johnson) current noise below 1 MHz, which is reduced by the added capacity. Nevertheless, the noise at the resonance

[3] 2-stage Current Sensor CN4 (3048–36A2) with VCblue (2965–45) as a ultralow-noise amplifier SQUID from supracon AG, 07751 Jena, Germany

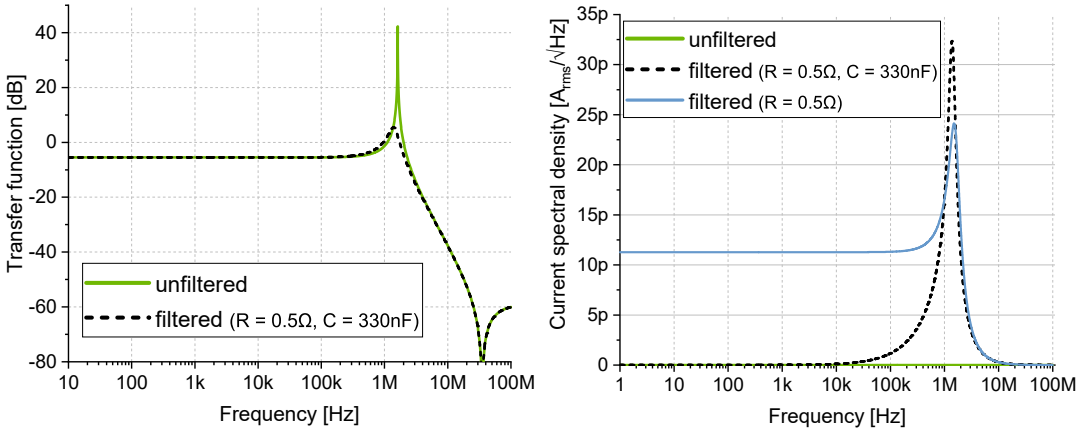

Figure 4.13: *(left) The transfer function between the applied (beam) current I_a and the current I_T at the input inductance L_i of the SQUID. (right) The spectral current noise density (right) as a function of frequency simulated with LTspice. The functions are given for the direct coupling of the pick-up coil L_p to L_i without any filter (solid green) and with an LC-filter ($R = 0.5\,\Omega$ & $C = 330\,\mathrm{nF}$) (dashed black).*

frequency is slightly increased. The resonance frequency is substantially larger than the typical frequency range of interest for the application at the accelerator of 10 kHz or lower. Therefore, as long as the stability of the FLL feedback is not undermined, the noise at the resonance frequency can easily be removed from the analog output signal of the FLL electronics with a low-pass filter.

4.4.2 SQUID parameter

The 2-stage dc SQUID from the supracon AG is controlled by their Jena SQUID System (JESSY) and is operated in the FLL readout mode. Similar to the FLL electronics from Magnicon GmbH, JESSY consists of a FLL module (including the pre-amplifier and the integrator) – placed as close to the SQUID as possible – and of a separate control unit. The setup routine follows the same principle as the electronics from the Magnicon GmbH and therefore the same guideline can be used (see Appendix). An overview of the SQUID parameter can be found in Tab. 4.1.

After the construction, the SQUID transfer function, the operating bandwidth and the maximum slew rate of the SQUID were determined using a test current $I_\Phi^{(\mathrm{fb})}$ through the feedback coil of the SQUID. With the FLL feedback switched off, the periodic modulation of the voltage V_{sq} across the SQUID – in reaction

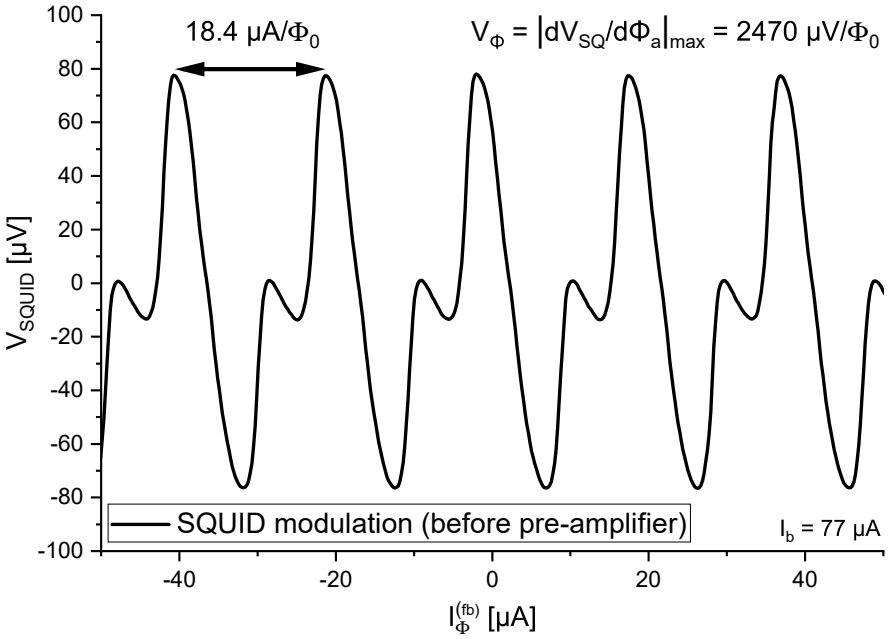

Figure 4.14: *Periodic modulation of the output voltage V_{sq} of the 2-stage SQUID with an applied magnetic flux created by the current $I_\Phi^{(fb)}$ through the feedback coil.*

to an applied magnetic flux via the feedback current $\left(\Phi_a \propto I_\Phi^{(\mathrm{fb})}\right)$ – becomes visible (see Fig. 4.14). Since a double-stage SQUID configuration was used for this CCC, the voltage modulation deviates from the simple sinusoidal relationship. Nevertheless, the voltage of the SQUID V_{sq} oscillates with a period of one magnetic flux quantum (Eq. (2.17) & (2.18)), which yields the inverse mutual inductance of the feedback coil of

$$\frac{1}{M_f} = 18.4\,\mu\mathrm{A}/\Phi_0\ . \tag{4.15}$$

The optimal working point is located at the steepest slope of the modulation, where the transfer function V_Φ of the SQUID is at the maximum of

$$V_\Phi = \left|\partial V_{sq}/\partial\Phi_a\right|_{\max} = 134\,\mu\mathrm{V}/\mu\mathrm{A} = 2470\,\mu\mathrm{V}/\Phi_0\ , \tag{4.16}$$

already taking into account the amplification by the pre-amplifier. Compared to the single stage SQUID of the radial CCC, the 2-stage SQUID configuration yields a significantly larger transfer function V_Φ and thus achieves a substantial reduction of the voltage noise introduced by the amplifier ($S_{V,\,\mathrm{AMP}}$). Further-

more, the gain G_{SQUID} between the FLL output V_{FLL} and the input from the SQUID to the pre-amplifier V_{sq} can be calculated according to

$$G_{\mathrm{SQUID}} = \frac{V_{sq}}{V_{\mathrm{FLL}}} = \frac{V_\Phi M_f}{R_f} = 6.7 \times 10^{-4} \quad \text{with} \quad R_f = 200\,\mathrm{k\Omega}\ . \tag{4.17}$$

In the FLL readout system JESSY, the gain-bandwidth-product (GBP) is fixed at 6 GHz and a static feedback resistor R_f is selected before the measurement campaign to achieve the desired system bandwidth. Considering the loop delay of $t_d = 20\,\mathrm{ns}$ expected at CRYRING, the maximum system bandwidth of $f_{3\,\mathrm{dB,\,max}} = 9\,\mathrm{MHz}$ (cf. Eq. (2.20)) can be obtained with the feedback resistor $R_f = 200\,\mathrm{k\Omega}$ according to

$$f_{3\,\mathrm{dB,\,max}} = 2.25 f_1 = 2.25\ (G_s \times GBP) = 9\,\mathrm{MHz} \quad \text{with} \quad GBP = 6\,\mathrm{GHz}\ , \tag{4.18}$$

with a unity-gain frequency $f_1(R_f, GBP) = 4\,\mathrm{MHz}$ ($f_1 t_d = 1/(4\pi)$). According to Eq. (2.24), the maximum slew rate of the system is given by

$$\dot{\Phi}_{f,\,\mathrm{max}} = \delta\Phi/2t_d \lesssim \Phi_0 f_1 = 4\ \Phi_0/\mu\mathrm{s} \approx 13.2\,\mu\mathrm{A}/\mu\mathrm{s}\ , \tag{4.19}$$

using the mutual beam inductance M_a (see below). However, for a 2-stage SQUID the linear flux range $\delta\Phi^{(\text{2-stage})}$ is reduced by the flux gain $G_\Phi = \partial\Phi_{\mathrm{amp}}/\partial\Phi_a$ according to $\delta\Phi^{(\text{2-stage})} = \delta\Phi/G_\Phi$ [29, 51]. The flux gain is the relationship between the flux at the primary SQUID Φ_a and at the amplifier SQUID Φ_{amp}. Therefore, a balance between the maximum slew rate and the reduction in the overall noise has to be found. In the ongoing development a focus is on increasing the stability of the SQUID when faced with the large slew rates which are expected at FAIR (e.g. during the injection) by using a combination of two parallel SQUIDs with different current sensitivities [52]. A robust, less sensitive SQUID which can keep track of the signal baseline and a second 2-stage SQUID with an optimized current resolution that can measure the small variations of the signal with maximum precision, thus eliminating the need to find a compromise between the maximum slew rate and the noise performance.

The quantities above characterize the SQUID itself by sending a test signal through the internal feedback coil. By applying a calibration current, the cur-

rent sensitivity of the assembled CCC can be determined. The period of the voltage modulation of the SQUID due to the magnetic flux (created by the calibration current) yields the (beam) current sensitivity

$$\frac{1}{M_a} = 3.3\,\mu\mathrm{A}/\Phi_0 \ . \tag{4.20}$$

with the mutual beam inductance M_a of the SQUID with the beam current.

4.4.3 Shielding factor

The estimated shielding factor of the CCC against an external non-azimuthal magnetic field was confirmed experimentally. A uniform magnetic field B_a at the location of the CCC was created by a Helmholtz coil enclosing the cryostat (see Fig. 4.3). The field was oriented with the primary field direction either in parallel or orthogonal to the axis of the CCC with field strengths of up to 225 µT (orthogonal) and 1 T (axial). The strength of the field was modulated according to $B_a(t) = B_0 \sin(2\pi f\, t)$ with fixed frequencies between 1 Hz and 10 Hz. This excitation frequency was selected in a way to measure primarily the screening effect of the superconducting shield of the CCC, rather than the shielding by the walls of the cryostat or any external magnetic field disturbances. The higher the frequency, the stronger the eddy currents which are induced in the metal of the cryostat that surrounds the CCC, which then acts as a magnetic shield and alters the determined screening factor.

From the response of the CCC to this external excitation, an effective parasitic sensing area $A_{eff}^{(\mathrm{par})}$ in the plane of the applied field was calculated according to

$$A_{eff}^{(\mathrm{par})} = \frac{\Delta\Phi_{sq}}{\Delta B_a} \ . \tag{4.21}$$

In this measurement configuration, the signal of the CCC in response to the external field was 2.8±0.6 Φ_0/T in an orthogonal and 10.4±0.4 Φ_0/T in the axial direction which corresponds to an effective parasitic area of $5.8 \times 10^{-15}\,\mathrm{mm}^2$ and $2.2 \times 10^{-14}\,\mathrm{mm}^2$ respectively. These values were then compared to the effective area of the pick-up coil $A_{eff}^{(\text{pick-up})}$ for the detection of the field from an ion beam.

It can be estimated according to

$$A_{eff}^{(\text{pick-up})} = \frac{\Delta\Phi_{sq}}{\Delta B_a} \approx \frac{\sqrt{L_i L_{sq}}}{L_p + L_i + L_{par}} N A_{geom} \approx 450\,\text{mm}^2, \tag{4.22}$$

with the geometric area of the pick-up of $A_{geom} = (R_{out} - R_{in})\ell = 9600\,\text{mm}^2$ and the inductance of the SQUID of $L_{\text{sq}} = 50\,\text{nH}$. Equation (4.22) is derived by using the relationship for the magnetic flux at the pick-up coil $I_a L_p = N A_{geom} B_a$ and replacing I_a with the flux expected at the SQUID after the flux transformer (Eq. (3.2)) with coupling factors set to $k = 1$ [10].

With the effective area of the pick-up and of the parasitic coupling, the attenuation factor for external magnetic fields was determined according to

$$A_{shield} = \frac{A_{eff}^{(\text{pick-up})}}{A_{eff}^{(\text{par})}}\ , \tag{4.23}$$

to be $A_{axial} = 207\,\text{dB}$ in axial direction and $A_{orthogonal} = 215\,\text{dB}$ in orthogonal direction, which is in good agreement with the predicted value.

4.4.4 Noise current spectral density

The noise density of the coreless CCC is a sum of the intrinsic noise of the SQUID, the thermal noise of the signal filter and the external perturbation from the environment. Figure 4.15 shows the rms spectral current noise density of the coreless CRY–aCCC measured in thermal equilibrium inside the magnetically shielded room at university Jena. The voltage output of the SQUID was converted to a current using the current to voltage calibration factor of $11.7\,\mu\text{A/V}$ that was determined experimentally.

First, the intrinsic flux noise density of the 2-stage SQUID (supracon CN4) using the JESSY readout is specified as $S_\Phi < 2.5\ \mu\Phi_0/\sqrt{\text{Hz}}$ and the white voltage noise density of the pre-amplifier is given as $S_{V,\,\text{AMP}} = 0.33\,\text{nV}/\sqrt{\text{Hz}}$. This results in a total noise density of the SQUID below $2.83\ \mu\Phi_0/\sqrt{\text{Hz}}$ (cf. Eq. (2.19)), which is equivalent to a current noise lower than $9.4\,\text{pA}_{\text{rms}}/\sqrt{\text{Hz}}$, using $1/M_a = 3.3\,\mu\text{A}/\Phi_0$. In Fig. 4.15, the measured white noise level of the SQUID of $4\,\text{pA}_{\text{rms}}/\sqrt{\text{Hz}}$ can be extracted at frequencies of around 10 kHz, at

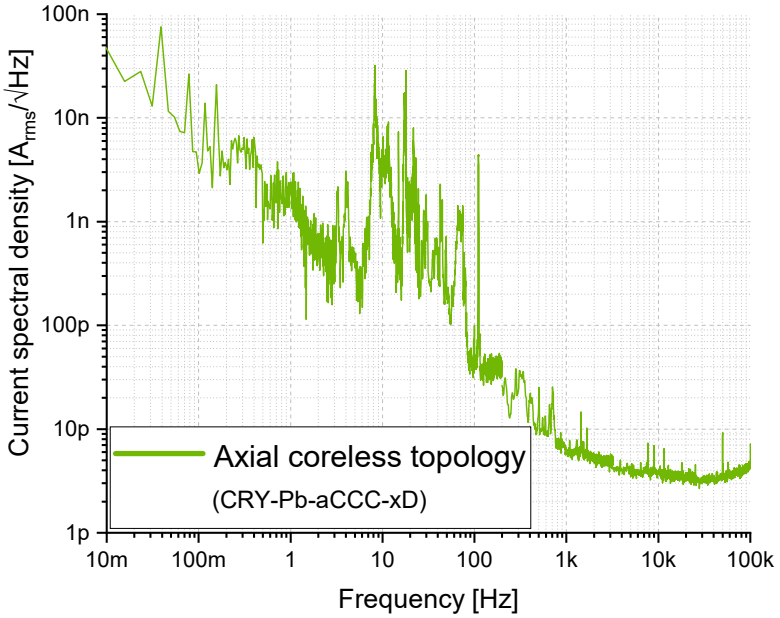

Figure 4.15: *The noise current spectral density (rms) of the coreless CRY–aCCC measured during the night in the magnetically shielded room at University Jena after three days at cryogenic temperatures. Mechanical perturbations between* 10 Hz *and* 100 Hz *are the prominent source of noise. An intrinsic white noise level of* $4\,\mathrm{pA}/\sqrt{\mathrm{Hz}}$ *is visible at frequencies of around* 10 kHz*.*

which external (electromagnetic) perturbations are strongly suppressed by the surrounding cryostat.

Furthermore, looking at the simulated noise density of the signal filter (see Fig. 4.13), its thermal current noise is very localized around the resonance frequency of 1.2 MHz. There are no significant contribution below 100 kHz. In the measured noise spectrum (Fig. 4.15) a small increase of the noise level is visible as the frequency approaches 100 kHz, which is in good agreement with the simulated spectrum. In combination with some noise sources (e.g. with the helium level sensor installed), the SQUID showed problems to maintain a stable operating point, which can indicate the need for a cleaner connection to ground potential or an insufficient damping of the resonance of the pick-up circuit and subsequently a large amount of noise at that frequency. Stronger damping should be evaluated for future models.

Nevertheless, the noise density at frequencies below 1 kHz is much larger than expected and cannot be attributed to either the SQUID or the signal filter.

Instead it originates in external perturbations of the environment, which can loosely be separated in thermal (including pressure) and in mechanical noise. The noise density at low frequencies ($< 10\,\mathrm{Hz}$) is characterized by a $1/f^{\alpha}$ noise contribution. One of the noise sources are temperature effects (e.g. drifts) of the operating environment, which produce a corresponding signal in the SQUID. Since the coreless CCC is still strongly susceptible to changes of the operating temperature, this indicates that the contribution of the core to the temperature susceptibility of the system is negligible and that the variations in the SQUID itself are the primary cause. However, fluctuations of the temperature or of the pressure above the helium bath are highly variable and linked to the measurement environment and thus are difficult to quantify. Further experiments are required to identify other noise sources which have a contribution at low frequency in order to find means to reduce their effect on the signal.

The noise spectrum between 10 Hz and 100 Hz is dominated by acoustic and mechanical vibrations (visible as spikes in the measured current noise density). Contrary to the expectations, the rigid connection between the individual layers of the shield with epoxy glue had no significant impact on the susceptibility against mechanical perturbations. Thus, the relative motion between the screening layers can be excluded as the primary cause of the microphony. At the same time the magnetostriction of the high-permeability core could be excluded as the primary coupling mechanism of mechanical vibrations. The mechanism of coupling of mechanical movement to the SQUID remains unclear and needs to be investigated further to eliminate this noise source.

4.5 Comparison of detector types

Both detector configurations have their unique advantages. A list of the design parameter of both CCC systems is given in Table 4.1. First of all, the measured shielding efficiency against magnetic fields – with the same dimensions of the shield and of the pick-up volumes – was confirmed to be much higher for the axial (ring) shield than for the radial (disk-shaped) meanders for the geometries required at FAIR [11], which is one of the key advantages of the new shield topology. This becomes apparent, when comparing the shielding factors of the

two detector models of 75 dB (radial design) and of 207 dB (axial design). It has to be noted, that the length of the CRY-aCCC is slightly larger than that of the radial design (210 compared to 290 mm), which makes the direct comparison of the two measured screening factors more difficult. However, this does not affect the general conclusion as shown in Sec. 4.1. Therefore, in an environment with large magnetic perturbations the axial design has a clear advantage.

Furthermore, a stronger coupling of the pick-up coil to the beam current (c.f. radial CCC) leads to larger signal amplitudes at the SQUID. More precisely, the mutual beam inductance of the radial CCC is $100\,\mathrm{nA}/\Phi_0$ compared to $3.3\,\mu\mathrm{A}/\Phi_0$ for the axial design. While a high current sensitivity is excellent to precisely measure low-intensity signals, for fast changing, high-amplitude signals (e.g. at injection) it increases the requirements towards the SQUID to cope with larger slew rates. Due to the reduction of the inductance of the high-permeability core at frequencies beyond 10 kHz, the mutual beam inductance of the radial design is decreased, which reduces the slew rate of high-frequency signals. Nonetheless, for larger amplitudes of the beam current the slew rate may become a problem for the radial CCC ($\dot{\Phi}_{f,\,\mathrm{max}}^{(\mathrm{radial})} \lesssim 400\,\mathrm{nA}/\mu\mathrm{s}$), while larger slew rates can be tracked with the coreless CRY-aCCC ($\dot{\Phi}_{f,\,\mathrm{max}}^{(\mathrm{axial})} \lesssim 13.2\,\mu\mathrm{A}/\mu\mathrm{s}$). While the mutual beam inductance is fixed for the CCCs under investigations, in principle it can be adapted for future models by changing the beam coupling (e.g. via the flux transformer) in order to adapt to the expected slew rates.

Moreover, the bandwidths of both detector models, as defined by the pick-up circuit, are comparable. The resonance frequencies – followed by the frequency cut-off – are 760 kHz for the CRY–rCCC (reduced to 170 kHz by the flux transformer) compared to 1.2 MHz for the axial CCC. Below the resonance frequency, the system gain of the coreless CCC is very linear. However, in the CRY–rCCC the change of the inductance of the high-permeability core leads to a non-linear gain at frequencies above 10 kHz, which needs to be taken into account for high-frequency measurements. In both systems, the 3dB-bandwidth $f_{3\,\mathrm{dB}}$ of the SQUID readout is limited by the loop delay to around 9 MHz.

Finally, the strongest indicator for the expected current resolution at the accelerator, is the spectral current noise density of the two detector models. Figure 4.16 provides a comparison of the current noise densities of the two prototypes. In

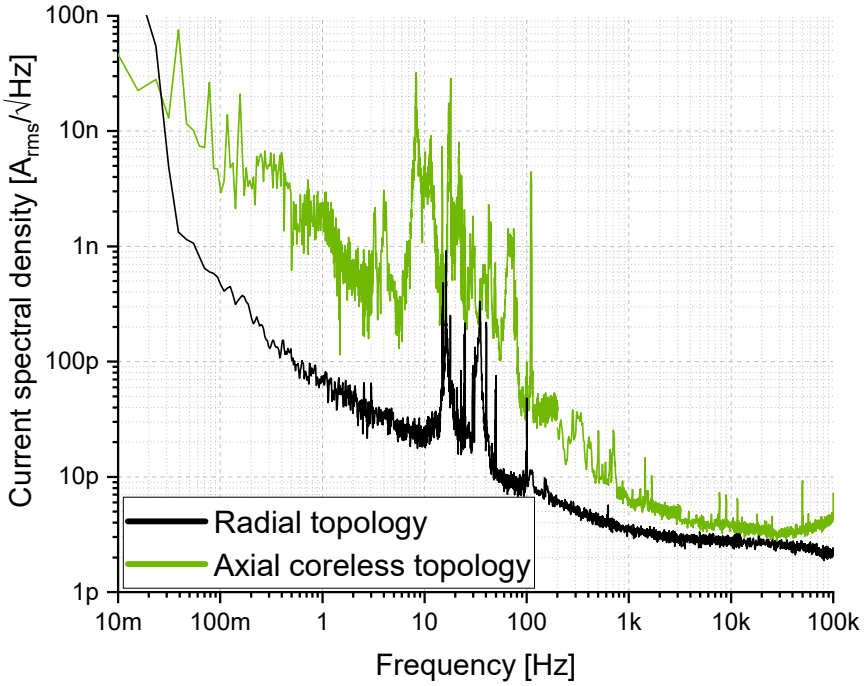

Figure 4.16: *Comparison of the rms spectral current noise density of the radial design (CRY–rCCC) and of the coreless axial design (CRY–aCCC) for CRYRING.*

the coreless CCC, the noise contribution of the high-permeability core could be eliminated and the intrinsic noise of the system is defined primarily by the flux noise of the SQUID. Contrary to the expectations, the susceptibility to external perturbations was not reduced in a similar manner and adds a significant amount of low-frequency ($f < 100\,\mathrm{Hz}$) noise to the low intrinsic noise level of the SQUID. As a result, at frequencies between 0.1 Hz to 100 Hz the noise density of the coreless CCC in the laboratory environment is larger by a factor 5 to 20. This factor is fluctuating with changes in the environment despite the large shielding factor and the cause is not yet fully understood.

One of the reasons is that the coreless CCC is affected strongly by temperature drifts. Moreover, both designs are susceptible to mechanical and acoustic perturbations between 10 Hz and 100 Hz. Although the CRY–aCCC exhibits a higher noise density in the laboratory environment, it is difficult to draw a final conclusion about the expected noise level at the accelerator, since not all the individual noise contributions and their individual coupling factors could be resolved. The effect of individual noise contributions on the spectral noise density

of the axial design will be investigated in more detail in the future.

Nevertheless, in both systems the intrinsic white noise at higher frequencies ($f > 1\,\mathrm{kHz}$) – where there is little influence of the environment – is almost identical. This indicates that it is possible to achieve the same noise performance without the use of a high-permeability core. With further measures to reduce the coupling of noise to the axial CCC, it seems feasible that the noise level of the radial CCC at lower frequencies can be matched with a coreless design.

In practice, for the implementation of the CCC as a standard diagnostic tool the cost of the apparatus is an important factor. The construction of the CCC in the axial design using sheets of lead is possible with very moderate costs and in a short amount of time. The primary limitation is the experience required for the delicate process of connecting the individual screens without deteriorating the shielding performance. In contrast, the material and manufacturing cost as well as the construction time, which are required for a radial CCC made from Niobium, are rather high and rely on elaborate machining and welding of the individual parts. This gives virtually no flexibility for experimenting with the detector configuration.

With the goal to maximize the current sensitivity and the stability of the detector for the measurement at CRYRING, it was decided to use the CCC in the radial design and with a high-permeability core because of the smaller spectral noise density. In a follow-up work, the coreless axial design will be improved further with the intention to test it with beam at the accelerator.

	Radial design	**Axial design**
Model	CRY–rCCC–xD	CRY–aCCC–xD
Material	Nb	Pb
Length [mm]	207	292.8
Inner/outer diameter [mm]	250/350	251.2/350
Mass [kg]	$\sim$ 65	$\sim$ 18
Gap meanders [mm]	1	~ 0.4
Meander/wall thickness [mm]	3	0.25/1.4
Inductance (pick-up) L_t	80 µH (@ 1 kHz) core	13.7 nH coreless
SQUID	Magnicon GmbH (C5XL1W)	Supracon AG (CN4, 2-stage)
Inductance L_{in} [nH]	1000	44
Input coupling $1/M_{in}$ [µA/Φ_0]	0.29	0.79
Feedback sensitivity $1/M_f$ [µA/Φ_0]	40.5	19
Current sensitivity $1/M_a$ [µA/Φ_0]	0.1	3.3
Max. slew rate $\dot{\Phi}_{f,\,\max}$ [µA/Φ_0]	$\lesssim 0.4$	$\lesssim 13.2$
Flux noise (@ 100 Hz) [µ$\Phi_0/\sqrt{\text{Hz}}$]	1.22	< 2.5
Pre-amplifier noise (white) [nV/$\sqrt{\text{Hz}}$]	0.33	0.33
Screening (dipole, lateral/axial)	≥ 58 dB	215/207 dB

Table 4.1: *Specifications of CCC systems for CRYRING@ESR.*

Chapter 5

Cryogenic support system

A custom made beam-line cryostat paired with a local helium liquefier provides the stable cryogenic environment for the operation of the CCC at the accelerator. As part of this project, an entirely new design for the beam-line cryostat was developed jointly with the Institut für Luft- und Kältetechnik gGmbH[1] [53]. After delivery to GSI, the cryostat was combined with the helium re-liquefier, was tested extensively and subsequently was installed in the accelerator beam-line at CRYRING@ESR. At all stages of operation, the cryogenic system has continuously been optimized to improve the operating parameter.

5.1 General design aspects

The signal background of the CCC determines the achievable current resolution and is directly connected to the mechanical and electrical conditions of the operating environment. Therefore, the demands on the cryogenic support system exceed the basic need to provide a continuous cryogenic temperature. In fact, the cryostat acts as a first layer of defense against perturbations.

It is documented that SQUIDs are sensible to variations of their operating temperature and, strongly linked with it, to the pressure above the liquid helium bath [14, 29]. It was shown for a CCC system, that temperature effects can result in a variable error in the order of 33.5 nA/mK, which is equivalent to

[1] Cryogenics and Low Temperature Physics Department, Institut für Luft- und Kältetechnik gGmbH, 01309 Dresden, Germany

73.7 nA/mbar [14]. This strong dependency shows the need for a well-controlled and stabilized operating pressure and temperature.

Moreover, any mechanical vibrations that couple to the CCC create a signal in the SQUID. Either directly by relative motion of the SQUID inside the surrounding magnetic field or indirectly by moving magnetic materials around the SQUID changing the magnetic flux at the detector itself. In order to minimize the transport of vibrations to the CCC, these excitation frequencies need to be damped before they can deteriorate the detector signal. At the same time, the eigenfrequencies of the cryostat should not align with any excitation frequencies that are expected in an accelerator environment.

Finally, the installation of the CCC as part of an accelerator beam-line imposes a set of mechanical constraints. The cryogenic volume holding the CCC has to surround the beam tube and bring the detector as close to the beam as possible while maintaining a strong thermal insulation between the cryogenic chamber and the beam tube which is at room temperature. In case the CCC is installed in a machine with high demands on the quality of vacuum (e.g. the UHV beam-line at CRYRING), the vacuum of the beam-line needs to be separated from the insulation vacuum of the cryostat. Moreover, to achieve vacuum pressures below 1×10^{-11} mbar in the internal UHV beam tube, it needs to be baked up to 200 °C without damaging the heat-sensitive CCC detector. A selection of general design criteria is given in Table 5.1. The sum of all these restrictions made the design of a suitable cryostat extremely challenging.

5.2 Design study

The temperature required to operate the CCC depends on the critical temperature of its superconducting shield and on the type of the built-in SQUID. For the lead and the niobium shield of the CCCs that are investigated in this thesis, the critical temperatures (T_c) are 7.2 K (Pb) and 9.25 K (Nb) [29]. The SQUIDs which are used in the CCCs are all low-temperature SQUIDs based on niobium and have similar temperature restriction as the superconducting niobium shield.

Furthermore, in an accelerator environment the whole instrument is subject to magnetic stray fields from neighboring dipole magnets and from a number

Parameter	**Requirement**
Temperature	Operating temperature below 6 K
Temperature & pressure stability	Variations smaller than 1 mK and 1 mbar per minute
Mechanical vibrations	Decoupling from surrounding, non-magnetic materials $\mu_r \approx 1$, no resonances below 15 Hz
CCC detector volume	Space available close to beam-line ($R_{in} = 125$ mm, $R_{out} = 175$ mm)
Vacuum quality	UHV-compatible bake-able beam-line (DN100)
Operating time	Longer than three days (no additional cooling) Continuous (with helium liquefier)
Materials	Non-magnetic, preferably non-(electrically)-conducting

Table 5.1: *List of general design aspects of the CCC beam-line cryostat.*

of other devices. Still it need to maintain its superconducting state despite a moderate surrounding field. The critical fields of these materials $B_c\,(T = 0\,\mathrm{K})$ – which indicate the maximum field strength that can be applied without any magnetic flux entering the bulk of the superconductor – are 80 mT (Pb) [54] and 180 mT (Nb) [55]. Since niobium is a type-II superconductor, it has a second critical field of $B_{c2}(0\,\mathrm{K}) = 410\,\mathrm{mT}$ [55]. When magnetic fields between the two critical field strengths B_{c2} and B_c are applied, the flux can penetrate through the bulk of the superconductor while the superconducting state (with a resistance of zero) is maintained.

As long as the temperature is well below the critical temperature of the superconducting material which is used, the critical field strengths of niobium as well as lead are large compared to the values that are expected at the detector location of significantly below 1 mT. As a consequence, to fulfill the demands on the operating temperature using helium with a boiling temperature of 4.2 K at ambient pressure as a coolant is necessary to reach the temperatures required.

In a preliminary study, different cooling options for this operating temperature were investigated including a platform cooled with a cryocooler, a gas-flow or liquid-flow cryostat and a bath cryostat. The use of cryocoolers as a primary cooling source has to be excluded because even low-vibration pulse-tube type cryocoolers introduce mechanical movements to the system that significantly affect the SQUID such that any direct mechanical connection to a cryocooler has

to be avoided. While all of these options can provide the desired temperature, the highest thermal stability is obtained with a helium bath cryostat, which makes it the cooling option which was selected for this application [56]. However, the use of a liquid helium bath requires (local) helium re-liquefaction to allow for continuous operation for at least several months of beam time.

At GSI some experience has been collected with the operation of a CCC inside a bath cryostat. The first CCC at GSI was operated in a 20 l helium bath cryostat that was constructed in 1993 [57] and which was used until 2015. The cryostat was designed to house a CCC with an inner diameter of 130 mm at the beam transfer lines at GSI. It combines its insulation vacuum with the vacuum of the beam-line, which made it perfectly suitable for the installation in the transfer lines where vacuum requirements typically are less stringent. The thermal shield was cooled by a cryocooler which had to be switched off during measurements due to the large mechanical perturbation. In 2017 a helium bath cryostat with a non-removable CCC detector paired with a mechanically decoupled cryocooler-based helium re-liquefier was constructed for the Antiproton Decelerator ring at CERN [58, 59]. The thermal shield is cooled by the evaporating helium gas and the liquefier allows cryogenic operation for months. Although both these cryogenic platforms are based on design choices that are very different from the ones required for FAIR (e.g. transfer line (GSI) vs. storage ring (CRYRING/FAIR), nonexchangeable single CCC detector for application (CERN) vs. multiple detector prototypes for CCC development (FAIR)), the experience collected during their construction and operation could be integrated in the design of the cryogenic support system for FAIR.

An elegant alternative cooling solution is a gas-flow cryostat with the helium gas being cooled by a remote cryocooler. Such a solution is promising, since there are some indications that the operation of a CCC inside the gas phase rather than the liquid phase leads to a decrease in the external noise coupled to the SQUID. Therefore, the principles of a gas-flow cryostat for the use with a CCC are recently being investigated at CERN and this option might become interesting for CCC systems in the future [60].

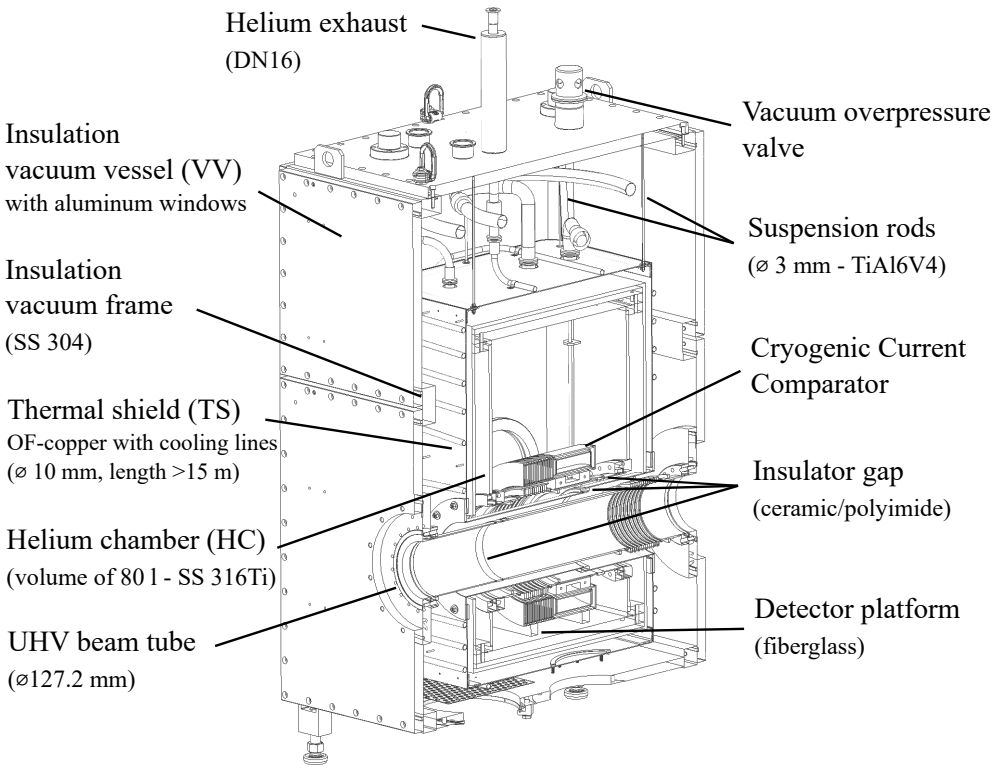

Figure 5.1: *3D model of the FAIR CCC beam-line cryostat. The CCC detector encloses the beam tube and is mounted inside the helium chamber. The helium exhaust on the top is connected to a helium re-liquefier. On both sides the cryostat is connected to the beam-line via a DN150CF flange.*

5.2.1 Mechanical design

The beam-line bath cryostat for CRYRING ($850 \times 850 \times 1200$ mm) incorporates an UHV-compatible beam-line with an inner diameter of 127.2 mm. Figure 5.1 shows the 3D model of the cryostat surrounding the CCC detector. The insulation vacuum vessel forms the outer layer of the cryostat and consists of a support frame of stainless steel (AISI 304) that is closed by two aluminum windows on each side that allow easy access to perform maintenance.

Inside the vacuum vessel, a thermal shield made of oxigen-free copper with more than 15 m of gas cooling lines ($\varnothing\, 12 \times 1$mm) protects the helium chamber from thermal radiation (see Figure 5.2). The shield is suspended from the lid of the vessel by four suspension rods ($\varnothing\, 3$ mm) made of grade 5 titanium (TiAl6V4). TiAl6V4 has a larger tensile strength than stainless steel (AISI 316) with almost half its thermal conductivity and, therefore, is a good choice for cryogenic applications.

Similar to the thermal shield, the enclosed helium chamber made of AISI 316Ti stainless steel is carried by four suspensions of TiAl6V4 with a diameter of 3 mm (see Fig. 5.2). On the bottom of the chamber four additional rods connect it to the vacuum vessel to stabilize its position. Both the thermal shield and

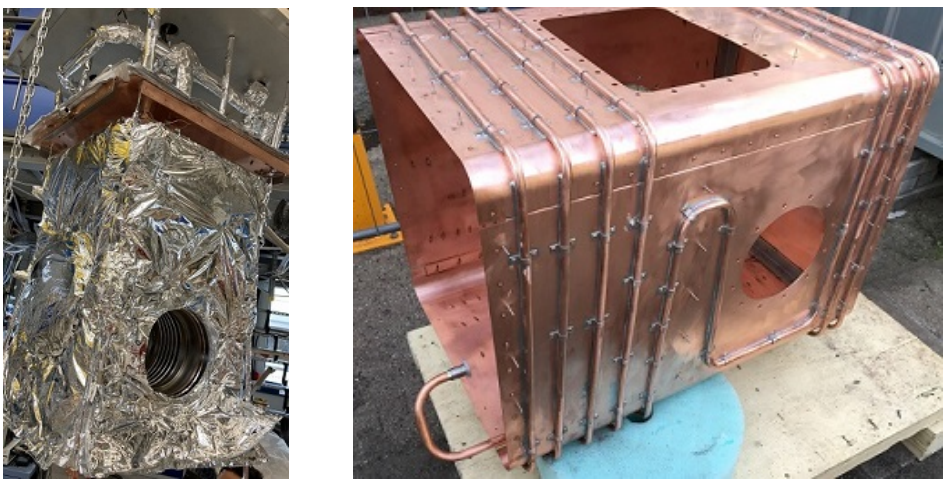

Figure 5.2: *(left) Helium chamber mounted to the lid of the vacuum vessel and covered with super-insulation (MLI). (right) Thermal shield during the production and before it is covered with MLI (courtesy of ILK gGmbH). The shield is cooled by the flow of the cold helium gas through the cooling line soldered to its surface.*

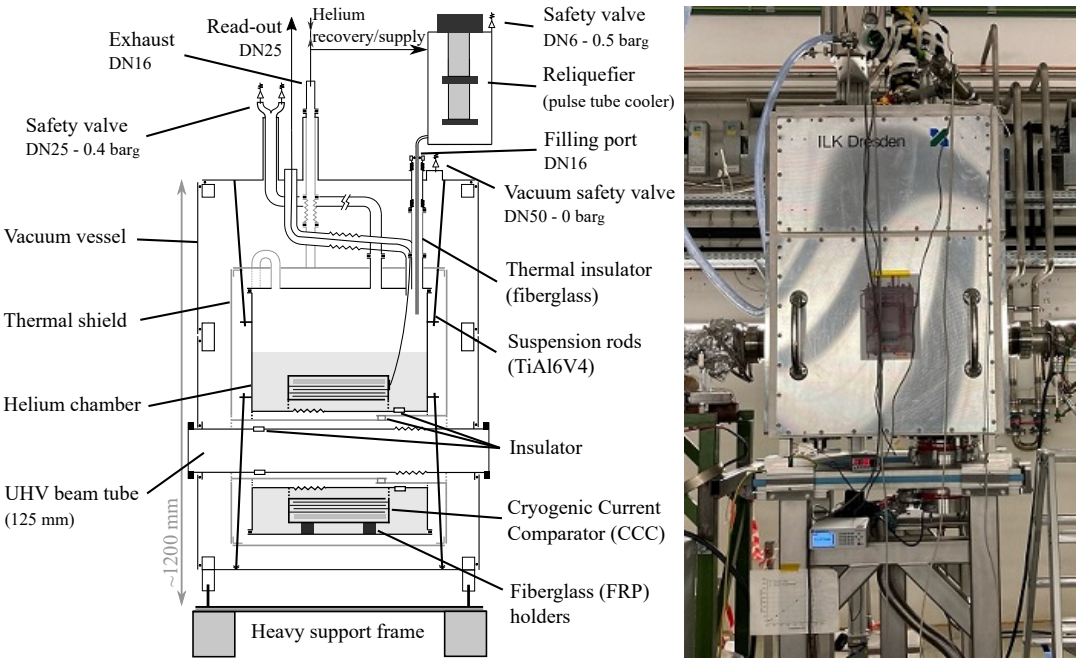

Figure 5.3: *(left) Schematic of the FAIR CCC beam-line cryostat. (right) Image of the vacuum vessel with part of the helium re-liquefier (on top) installed at the CRYRING.*

the helium chamber have maintenance windows on the two sides perpendicular to the beam propagation. The total capacity of the empty helium chamber is slightly above 80 l. It can be equipped with a CCC with a minimum inner diameter of 250 mm, a maximum outer diameter of 350 mm and a length of up to 235 mm. For a map of possible detector volumes please refer to Figure A.1 in the appendix. Inside the helium chamber the CCC is placed on two u-shaped platforms made from fiberglass.

In order to isolate the cryostat from mechanical vibrations in the vicinity at CRYRING, the entire cryostat was placed on a heavy support frame filled with sand. Figure 5.3 shows the entire assembly installed at the beam-line. In practice, the connection of the cryostat to the heavy support structure was useful to dampen the eigenmode oscillation and a complete decoupling from the ground was not advisable, since this drastically increased the amplitude of the vibration at the eigenfrequency of the cryostat. A damping mat[2] with a height of 25 mm

[2]Sylomer SR28 damping mat (900×850 mm with central hole of ⌀640 mm, load of 1000 kg), Getzner Spring Solutions GmbH, Germany. Insulation factor was calculated using Freqcalc

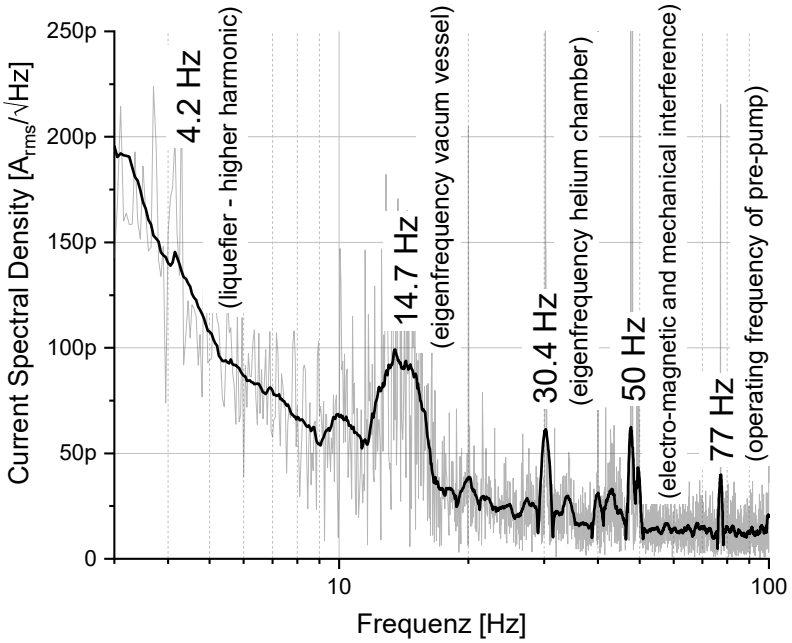

Figure 5.4: *Current noise density spectrum from* 3 *to* 100Hz *calculated from a background measurement of the CCC installed at CRYRING. Notable perturbations are labeled with their respective source.*

between the support and the cryostat insulated the setup from vibrations with frequencies above 25 Hz with a damping factor larger than 30 dB for frequencies beyond 125 Hz. Furthermore, at the interface between the cryostat and the accelerator beam-line, diaphragm bellows were installed. The helium liquefier was mounted on a separate support and the helium lifter was decoupled mechanically from the cryostat by a diaphragm bellow stabilized by rubber feet.

After the installation at CRYRING, a spectral analysis of the CCC signal of the final assembly confirmed that the decoupling of mechanical vibrations, while not perfect, is highly efficient (see Figure 5.4). It limited the mechanical perturbation to a small set of perturbations with a known source: First, there was a moderate contribution around 14.7 Hz, which was identified as the eigenfrequency of the vacuum vessel by looking at the frequency response of an accelerometer[3] (connected to the surface of the vacuum vessel) after a mechanical excitation pulse [50]. Second, there was a narrow signal at 30.4 Hz, which could be linked

by Getzner (apps.getzner.com).

[3] Accelerometer KS813B, Metra Meß- und Frequenztechnik e.K., 01435 Radebeul, Germany

to the eigenmode of the helium vessel. Using a simplified geometry of the cryostat, the mechanical eigenmodes of the different vessels were simulated at TU Darmstadt [61]. The results showed three eigenmodes with frequencies in the range of 32 Hz to 34 Hz. Taking into account the error due to deviations of material properties and due to the crude model of the cryostat, the measured peak could be associated with the simulated eigenmodes of the helium vessel. Finally, a small perturbation by the pre-pump – which operates at 77 Hz – could be observed.

The vibrations at 14.7 Hz (vacuum vessel), at 77 Hz (pre-pump) and slightly below 50 Hz (general electro-mechanic background) were present in the frequency spectrum of the accelerometer when it was connected to the outside of the vacuum vessel. Therefore, a mechanical coupling of the vibrations to the CCC signal was evident. However, the vibration by the pulse-tube cryo-cooler of the helium liquefier (1.44 Hz) and the signal exactly at 50 Hz were strongly suppressed at the vacuum vessel, such that a different coupling mechanism to the CCC signal (via gas pressure and via electromagnetic interference respectively) was indicated.

5.2.2 Insulator gap – beam tubes

All electric conductors bridging the incoming and the outgoing beam tube may cause a disruptive electric current flowing through the CCC and thus require a non-conductive insulator gap. In particular the beam-, the shield- and the helium tube are equipped with ceramic or synthetic gaps. The insulator suppresses mirror currents which flow along the beam tube and which would shield the magnetic field of the beam.

The standard implementation for a vacuum-compatible, cryogenic insulator is a ceramic ring (Al_2O_3) with metallized end caps. The ceramic is soldered to an intermediary flange made of Invar or Kovar, which both are alloys with a small thermal expansion coefficient similar to the one of ceramic. The intermediary flange is welded to the rest of the beam tube (e.g. 316LN stainless steel for the UHV beam-tube). When the temperature of the tube is altered – e.g. during the cool-down or as part of the vacuum baking – the homogeneous change of the dimension of the ceramic and of the alloy due to the thermal expansion,

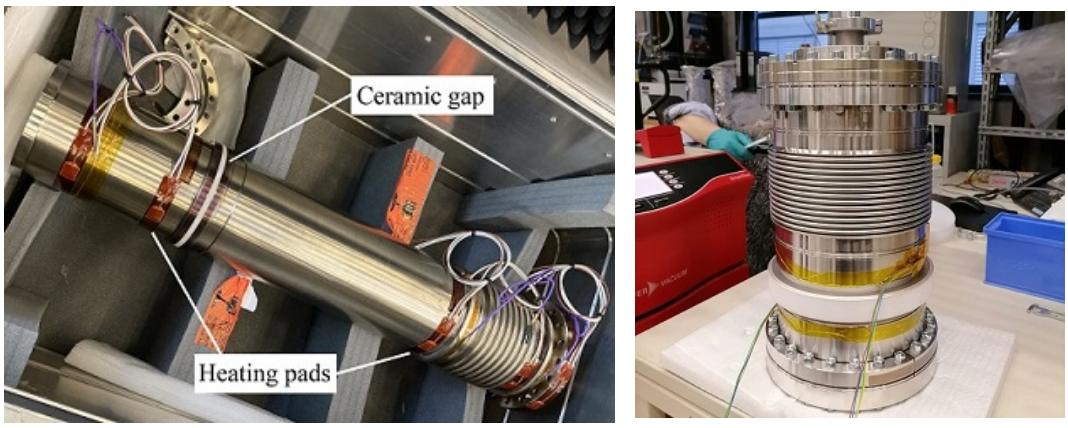

Figure 5.5: *(left) The UHV beam tube (inner ⌀ 127.2 mm) enclosed by the cryostat with the ceramic insulator gap and heating pads for the vacuum bake-out. (right) Cryogenic helium beam tube (inner ⌀ 200 mm) during the helium leak test after cryogenic testing. The ceramic insulator and the corrugated bellow are shown.*

keeps the mechanical forces at the interface to a minimum. If the thermal expansion coefficients of the materials are quite different or the interface between the various parts is designed poorly, the dynamic forces lead to a break of the ceramic or of the soldering connection. In order to prevent longitudinal forces and to allow a small axial compression during the installation of the tube inside the cryostat, a corrugated bellow is included in the tube. Figure 5.5 shows the assembled vacuum and the helium tube.

Before a cryogenic ceramic gap became available, instead an insulator gap made of polyimide[4] had to be designed as part of this thesis as a temporary workaround for the helium tube during the installation at CRYRING. Polyimide was selected for its thermal expansion coefficient, which is reasonably close to the one of AISI 304 stainless steel ($\alpha(293\,\mathrm{K}) = 15.1 \times 10^{-6}\,\mathrm{K}^{-1}$ [56]) compared to other standard polymers. The beam-tube and the polyimide insulator are connected with epoxy resin. A drawing of the insulator gap is given in Figure 5.6. To increase the flexibility of the insulator and to reduce the force on the glued interface when there is some deformation, the material thickness of the polyimide ring was reduced by a groove at half the total height. At the interface to the beam tube, the polyimide ring – on each end – has a notch to accept the tube. The

[4]Tecasint 2011 natural ($\alpha(50\,^\circ\mathrm{C}$ to $200\,^\circ\mathrm{C}) = 43 \times 10^{-6}\,\mathrm{K}^{-1}$) by Ensinger Sintimid GmbH, 4863 Seewalchen, Austria

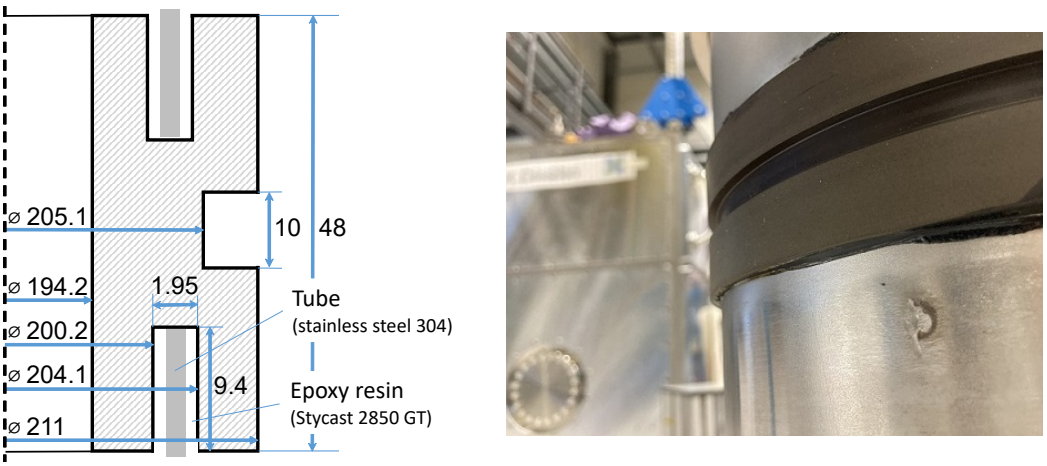

Figure 5.6: *(left) Cross-section of the electrical insulator made of a polyimide ring that is glued to the beam tube of the helium chamber. (right) Photograph of the polyimide insulator glued to the stainless steel tube.*

inner surface of the notch is sand blasted and treated with coarse sand paper to produce a rough surface in order to maximize the adhesion of the epoxy glue. The section of the beam tube, which is inserted in the notch, was machined to a inner/outer diameter of ($\varnothing$ 200.4/203.9 mm) and to have concentric grooves to increase the contact surface of the glue.

The epoxy resin Stycast 2850GT is used to connect the two elements. It shows a good cryogenic stability and bridges the thermal expansion properties between polyimide and stainless steel [56, 62]. Subsequent vacuum leak tests show a leak rate below 7×10^{-9} mbar l/s across multiple cool-downs and throughout several months of cryogenic operation. This solution is an excellent alternative to the traditional ceramic insulators, however, extreme care has to be taken during the installation since the interface between the polyimide and the epoxy resin is very fragile compared to the strong forces that are applied during the mounting of a stainless steel DN200CF flange.

5.2.3 Cryogenic design

The primary goal of the cryogenic design is to reduce the evaporation rate of the helium bath to a value which can be processed by a local helium re-liquefier to achieve an extended cryogenic operating time. During the design phase a simplistic heat estimation was done by the company ILK for the beam-line

cryostat, however more detailed heat input calculations – taking into account the entire cryogenic support system including the helium liquefier and the data collected during cryogenic operation – were done as part of this work.

The primary sources of heat transport toward the helium chamber are *heat conduction* across solids, convective heat transfer through gas and heat radiation of surfaces. The conductive heat flow $\dot{q}_{cond}$ along an isotropic solid with a cross-section A, a total length l and a thermal conductivity $\lambda(T)$ can be calculated according to the so-called heat integral

$$\dot{q}_{cond} = \frac{A}{l} \int_{T_1}^{T_2} \lambda(T)\, dT \ , \tag{5.1}$$

where the temperatures on opposing ends of the solid are fixed at T_1 and T_2 [56]. The thermal conductivity $\lambda(T)$ of stainless steel (304 and 316) and titan grade 5 (TiAl6V4) which are used in the construction of the cryostat are well described in literature [56, 63, 64]. Along all ports to the helium chamber the stainless steel tubes were interrupted by diaphragm bellows or thermal insulator tubes made of fiberglass and, wherever possible, the total length of the connection was increased in order to reduce the amount of conducted heat. Diaphragm bellows are made from thin metal sheets which decreases the cross-section available for the heat transport while at the same time increasing the effective length of the connection. At temperatures below room temperature fiberglass has a lower thermal conductivity than stainless steel by approximately one order of magnitude [56], which leads to a reduction of the heat flow. All suspensions between the vacuum vessel and the helium chamber were thermally coupled to the heat shield to absorb the majority of the heat flux and to minimize the heat input at the helium chamber

Convective heat transport by the gas between the vacuum vessel at room temperature and the cold thermal shield or the helium chamber is strongly reduced by a good insulation vacuum. The heat conduction across the gap between the individual layers of the cryostat with a distance between the surfaces of around 10 mm in the area of the beam tube and up to 90 mm at all other locations is

$$\dot{q}_{conv} < 1 \times 10^{-6}\,\mathrm{W/(m^2\,K)}, \tag{5.2}$$

	Surface area [m^2]	Emissivity ϵ	Emittance factor E
Vacuum vessel	5	0.3	
Thermal shield	3.3	0.15	0.09 (VV→TS)
Helium chamber	2.3	0.2	0.11 (TS→HC)

Table 5.2: *Emissivity values to determine the heat radiation were adapted from [56, 65].*

with an insulation vacuum in the order of 5×10^{-7} mbar [56]. This amounts to a total heat load below 1 mW on the thermal shield and, thus, can be neglected. The heat flow from a surface at a temperature T and with an area A due to *thermal radiation* is described by the Stefan-Boltzmann equation

$$\dot{q}_{rad,Boltzmann} = \sigma \epsilon A T^4 \ , \tag{5.3}$$

with the emissivity ϵ of the surface and the Stefan-Boltzmann constant $\sigma = 5.67 \times 10^{-8}\,\mathrm{W/(m^2\,K^4)}$. The effective heat transport between two surfaces at different temperatures (T_1, T_2) can be calculated with

$$\dot{q}_{rad} = \sigma E A \left(T_2^4 - T_1^4\right) \quad \text{with} \quad E = \frac{\epsilon_1 \epsilon_2}{\epsilon_1 + \epsilon_2 - \epsilon_1 \epsilon_2} \, , \tag{5.4}$$

where A is the surface of the smaller area and E is an emittance factor (see Tab. 5.2), which combines the emissivity of the two parallel plates (ϵ_1, ϵ_2) [56]. While the specific heat of materials to calculate thermal conduction are well defined, the situation for the emissivity of surfaces is different. There are values of the thermal emittance of surfaces for different temperatures (and wavelengths) in literature [56, 65], however there is a large spread depending on the quality of the surface. Additionally, several layers of aluminized polyester foils, so called Multilayer Insulation[5] (MLI), are installed on the surface of the thermal shield (20 layers) and of the helium chamber (30 layers) and further reduce the heat input by a factor of $\dot{q}_{rad} \propto 1/(N+1)$ depending on the number N of total layers [65]. As a result, in any practical setup the calculated heat radiation can only provide a good assumption of the expected heat input. The effective value always needs to be confirmed experimentally.

[5]RUAG Coolcat 2 NW by RUAG Space GmbH, 1120 Vienna, Austria (www.ruag.com/thermal)

	Heat input [W] (TS/HC)	
Component	basic instrumentation (TS @ 115 K)	with CCC & liquefier (TS @ 100 K)
Suspension rods	0.9/0.07	1.0/0.06
Ports	1.6/0.20	1.7/0.16
Instrumentation	0.2/0.12	0.3/0.22
Liquefier (lifter)	-	0.0/0.07
Thermal radiation	7.9/0.07	8.0/0.04
Total	10.6/0.46	11.0/0.55

Table 5.3: *Estimated heat load on the thermal shield (TS) and on the helium chamber (HC) of the cryostat with the basic instrumentation (temperature sensor, helium-level sensor) and with the CCC, the calibration line and the re-liquefier installed (measurement configuration).*

With the known geometry of the cryostat, the total heat load on the thermal shield and on the helium chamber can be calculated. Table 5.3 gives an overview of the individual heat contributions. For the thermal shield the only source of cooling is the cold helium gas, which leaves the helium chamber at a temperature of 20 K and flows through the OF-copper cooling lines. The temperature of the outer vacuum vessel is assumed to be 300 K.

With the *basic instrumentation* of the cryostat (temperature sensors, helium-level sensor) the average temperature of the shield at the thermal equilibrium was measured to be 115 K with the individual parts (bottom plate, side plates and tube around UHV beam-line) all within ± 5 K. The available cooling power (or change of enthalpy dH) between 20 K and 115 K at a constant pressure of the helium gas can be calculated to be $dH_{(20\text{–}115\,\mathrm{K})} = 494\,\mathrm{J/g}$ [66]. The total heat load at the helium chamber for the equilibrium temperature sums up to 0.46 W. Given the latent heat of evaporation of helium at 1 bar of 20.75 J/g [56], the heat input leads to an estimated evaporation rate of 15.2 l/d or 79 g/h. At GSI an evaporation rate of 15.4 l/d could be measured.

In the *measurement configuration* – with the CCC, the calibration line and the re-liquefier installed – the additional heat input to the helium chamber is around 90 mW. The increased heat input is equivalent to an evaporation rate of 18.2 l/d or 95 g/h. The higher evaporation drives the cryostat to a new thermal equilibrium with the shield at roughly 100 K ($dH_{(20\text{–}100\,\mathrm{K})} = 416\,\mathrm{J/g}$) [66].

5.3 Cryogenic operating performance

In order to monitor the cryogenic operating performance, the cryostat was equipped with a total of 10 temperature sensors (four Carbon Ceramic Sensors[6] and six PT1000) distributed throughout the helium chamber and the thermal shield. Moreover, the evaporation rate was measured by a gas flow meter at the exhaust and, additionally, was calculated from the decline of the helium level, which was measured by a resistive helium level sensor[7] inside the helium bath. Finally, the pressure in the helium chamber and in the helium return line was documented with a pressure transducer[8]. The operation of the cryostat together with the helium liquefier turned out to be more challenging than expected and required a more detailed analysis of the operating parameter and, in particular, the gas flow inside the closed helium cycle.

5.3.1 Helium re-liquefier and self-sufficient operation

The evaporating helium gas leaves the cryogenic helium chamber through a hole at the top. From there a copper cooling line runs to the bottom of the thermal shield and only then is connected to the surface of the shield with a silver-based soft soldering agent. Then the cooling line winds in a spiral around the outer surface of the shield and leaves the cryostat through an exhaust at the lid of the vacuum vessel. The gas is guided to a Cryomech helium re-liquefier[9] with a specified liquefaction power from room temperature helium gas of 19.23 l/d (0.85 W @ 4.2 K). After the liquefaction, the liquid helium is transferred back to the helium chamber through a double-walled vacuum-insulated helium transfer channel (so-called helium lifter). The helium cycle was always operated at a small over-pressure to prevent contamination with other gases. Any contaminants will accumulate at the cryocooler and reduce the capacity of the liquefier. A schematic of the entire helium cycle is given in Figure 5.7.

In preliminary experiments of the liquefier with a standard helium dewar as well as with the 20 l GSI CCC cryostat from 1993, in practice, liquefaction rates

[6] SCB-CCS04 Carbon Ceramic Sensor from Cryoandmore GbR, 41472 Neuss, Germany
[7] Helium Level Sensor (635 mm active length, 4.488 Ω/cm) from Cryoandmore GbR
[8] P51UL (relative) Pressure Sensor, SSI Technologies LLC, Wisconsin 53546, USA
[9] Cryomech HeRL15, Cryomech Inc., Syracuse, NY 13211, USA (www.cryomech.com)

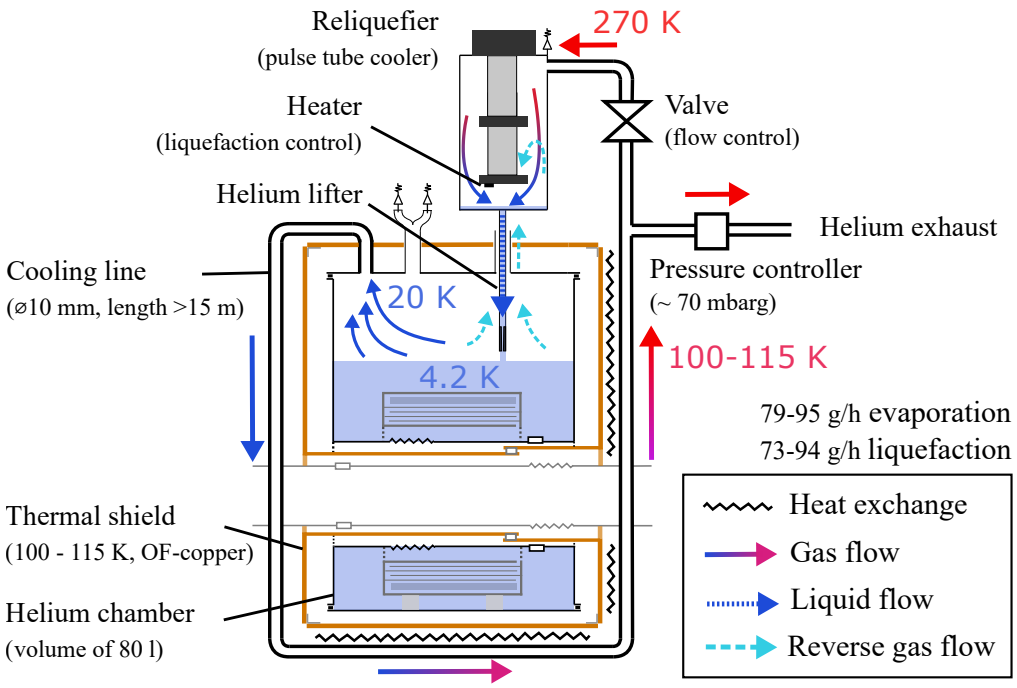

Figure 5.7: *Schematic of the closed helium cycle of the cryogenic support system of the CCC. The evaporating helium gas flows through the cooling line to the helium liquefier and absorbs heat from the thermal shield.*

between 14 l/d and 18 l/d were achieved [57]. Since the stand-alone evaporation rates of both of these setups were significantly below the maximum capacity of the liquefier, additional helium gas was introduced to the gas return line of the liquefier. In a first approximation, the achieved liquefaction rate is the sum of (1) the additional liquid helium inside the chamber after some time of operation at a stable pressure – measured with the helium level sensor or calculated from the increase of the total weight of the setup – and (2) the stand-alone evaporation rate of the setup without the liquefier. As a reference, the total amount of gas that is added to the system is measured with a flowmeter and gives another measurement of the additional liquid inside the chamber. However, the rate of liquefaction determined in this way omits the additional heat input and the increased evaporation rate due to the connection of the liquefier to the system. Therefore, the true liquefaction rates during the experiment were higher than calculated and, thus, are in agreement with the specified liquefaction power.

The additional heat load from the liquefier is a combination of the heat conduction along the liquid helium lifter and an excessive circulation of helium gas

through the helium chamber, the shield and the liquefier. To minimize the heat input via heat conduction, the lifter is not inserted into the liquid, but is placed close to its surface where it is cooled by the evaporating gas. The heat transport by convection of the helium gas is driven by the liquefaction process and is more difficult to mitigate. During the liquefaction, the cryocooler cools down helium gas which increases its density, such that some of it sinks down along the lifter to the helium chamber before it can be liquefied. The opposite process takes place in the cooling lines of the shield, where the gas warms up which reduces its density so that it tends to rise to the highest point in the system which is the liquefier (see Fig. 5.7). The resulting natural convection, also called thermosiphon, increases the gas circulation beyond the amount of gas which is evaporating and which is condensed by the liquefaction process itself. While the heat conduction along the lifter can be estimated with reasonable accuracy, the heat load due to the excessive gas flow is difficult to quantify without knowledge of the precise gas flow. Nevertheless, in order to minimize the additional convective heat load, the total gas circulation must be carefully controlled with a valve in the helium gas return line. By constricting the gas flow, the amount of gas which reaches the liquefier should be kept close to its liquefaction capacity.

However, the total pressure drop along the cooling line followed by the gas return line ($\varnothing\,20\,\mathrm{mm}$) between the cryostat and the liquefier was estimated to be a few millibar at a shield temperature of 100 K and with a gas flow equivalent to 20 l/d (104 g/h). While the absolute pressure drop is small, the drop along the unobstructed liquid helium lifter of the liquefier is of a similar magnitude. In the case that the flow resistance along the gas return line is increased (e.g. with the flow control valve), it opens up the possibility for part of the gas to flow to the liquefier through the liquid helium lifter and to bypass the cooling lines. The consequence is a strong instability of the system parameters (shield temperature, gas pressure, evaporation rate) as soon as the gas circulation is constricted.

Therefore, while in a first simple approximation the liquefaction power of the liquefier is sufficient to compensate the helium evaporation of 15.4 l/d of the basic cryostat, it was impossible to find a configuration with an effective helium loss smaller than 1 to 5 l/d. Figure 5.8 shows the resulting temperature dis-

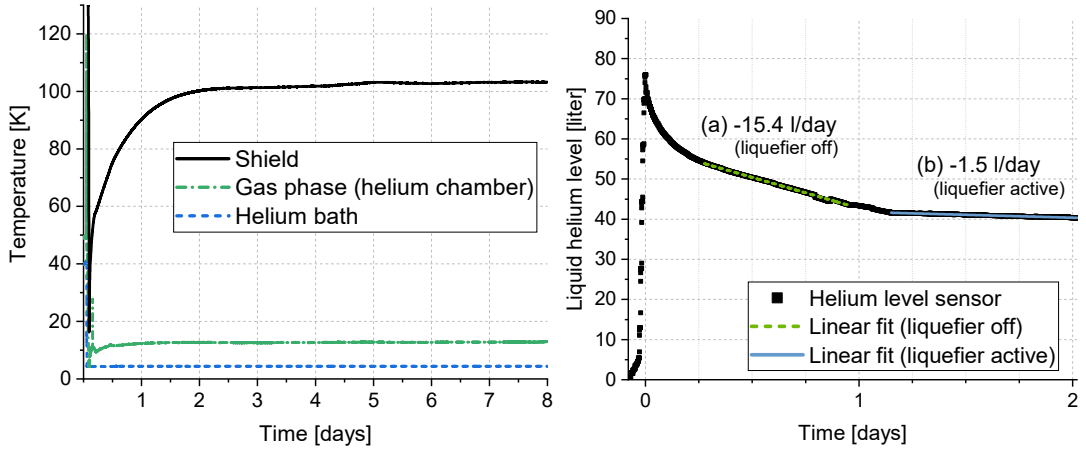

Figure 5.8: *(left) Evolution of the temperatures at different sections of the beam-line cryostat in the measurement configuration after helium filling. A nozzle is installed at the helium lifter to reduce the excessive gas circulation. (right) The decline of the helium level measured with a resistive helium level sensor. Section (a) shows the stand-alone evaporation of the cryostat with the basic instrumentation. Section (b) gives the reduced evaporation when the helium re-liquefier is active.*

tribution of the cryostat throughout a week of operation as well as the decline of the liquid helium level with and without the liquefier in operation. Some of the helium loss remaining after the liquefaction was discovered to be due to a gas leakage through the metal-sealed cryogenic safety valves. The valve will be replace with a rubber-sealed one with a lower leakage rate in the future.

In order to stabilize the operating pressure despite the insufficient liquefaction power, excess gas left the system via a passive pressure controller. In case the liquefaction power is larger than the evaporation rate and the pressure drops below a certain setpoint – typically 70 mbar above atmospheric pressure – the liquefaction rate will be reduced by a heater at the cryocooler to keep the pressure at the setpoint value.

5.3.2 System stability

The cryogenic support system in the measurement configuration can sustain a stable operating environment for 11 days in the case that the gas circulation through the shield is restricted. However, the existence of two equivalent paths for the helium gas to flow – through the shield and through the liquid helium lifter – makes the system unstable in this operating conditions. In practice, the

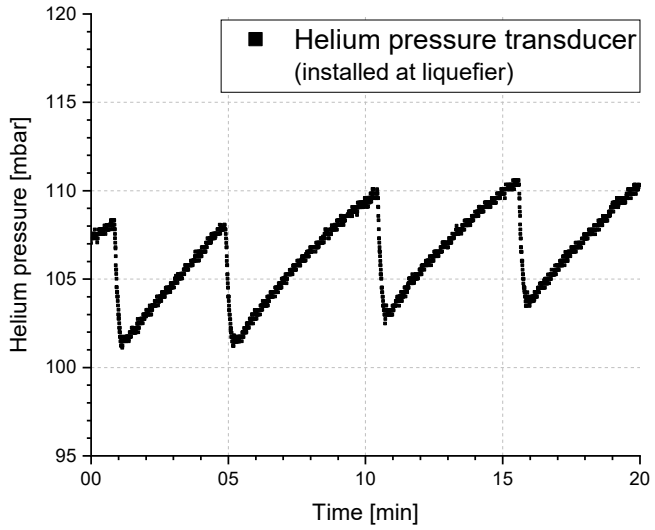

Figure 5.9: *Measurement of the pressure of the helium gas at the helium return line close to the liquefier by a P51UL pressure transducer from SSI Technologies. The periodic collapse of the helium circulation creates a saw-tooth-shaped pattern when the system is in the oscillating operating mode.*

cryostat shows two different modes of operation and can jump between them spontaneously:

In the *oscillating mode*, the pressure above the helium bath as well as the temperature within the cryostat both oscillate with a period of several minutes in a saw-tooth-like pattern (see Figure 5.9). The period depends on the amount of additional flow resistance due to the valve in the helium return line to the liquefier. The peak-to-peak amplitude of these oscillations are typically below 10 mbar, but also values of 32 mbar were observed. The temperatures throughout the cryostat show an identical pattern, which is a gradual rise followed by a sharp drop. Interestingly, the temperature at the cryocooler exhibits the opposite behavior, which is a sharp rise of the temperature followed by a gradual decline. An explanation could be a sudden release of liquid helium which has built inside the liquefier, however further investigations are necessary to confirm this hypotheses.

In cryogenic systems a typical source of similar behavior are thermo-acoustic oscillations (TAOs) [56, 67, 68]. However, the geometries in which they are likely to appear according to literature (tubes with a radius of around 1 mm in combination with a large temperature difference between its ends) are not present

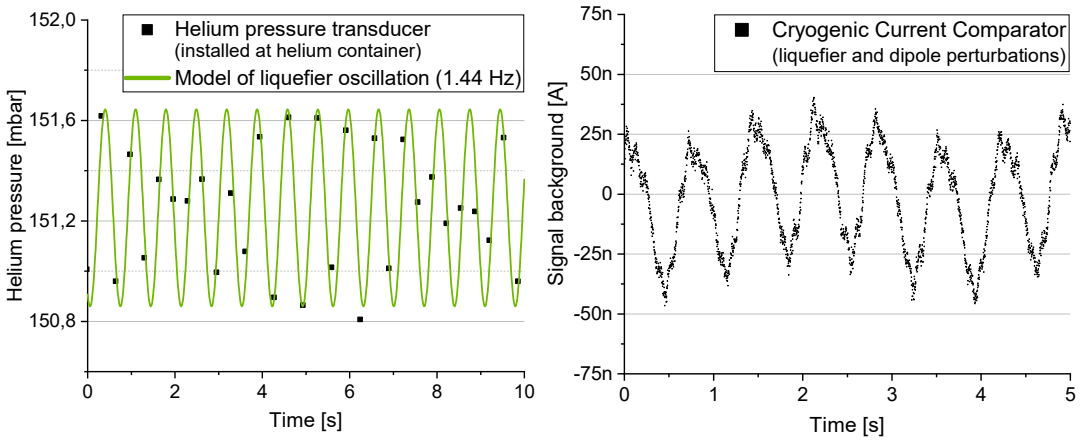

Figure 5.10: *(left) Pressure above the helium bath inside the helium chamber (black rectangles). The data points show a good agreement with a sinusoidal pressure fluctuation of the liquefier with the known operating frequency of* 1.44 Hz *(green). (right) CCC measurement taken at CRYRING showing the sinusoidal perturbation by the liquefier with an amplitude of around* 60 nA.

in our cryostat. More importantly, no significant periodic signals at acoustic frequencies (0.1 kHz to 20 kHz) could be identified in the Fourier spectrum of the CCC signal. However, measurements with a faster and more precise pressure sensor are ongoing during the preparation of this thesis to fully exclude TAOs as a source for these oscillations.

The *smooth operation mode* (see Fig. 5.8) does not exhibit any oscillations and is characterized by a colder shield temperature and gas return line, indicating a larger gas flow. For measurements with the CCC, the cryostat has to be kept in the smooth operating mode to avoid large perturbations due to the constant change of both the system pressure and the temperature.

In order to suppress the gas flow through the lifter of the liquefier, a nozzle made of polyvinyl chloride (Trovidur®) is mounted to the end of the lifter and reduces the local diameter to 1 mm for a length of 30 mm. This adds a flow resistance along the lifter equivalent to a pressure drop along the nozzle at a hypothetical gas flow of 95 g/h (all the gas goes through the lifter) of around 1 mbar. In operation, the result is an extension of the smooth operating mode to configurations with a smaller gas circulation (gas return value is closed more). Due to the reduced gas flow through the shield, a small increase of the shield temperature was observed. However, there was not enough time to set the gas circulation

to the optimal value and an evaluation of the effect on the evaporation rate is foreseen in the future.

In addition to the oscillations caused by the unstable gas flow, the pulsed nature of the cryo-cooler of the helium liquefier creates a periodic oscillation of the system pressure. During the cooling and the condensation of gas, the volume of the helium – and with it the local pressure at the liquefier – is reduced and gas is pulled periodically from the helium chamber to the cryocooler. The pressure at the liquefier shows an oscillation with a peak-to-peak pressure swing of 1 to 2 mbar measured at the gas transfer line. The operating frequency of 1.44 Hz was confirmed by a spectral analysis of the CCC signal (see Fig. 6.18 in Chap. 5). The nozzle attenuates the pressure oscillation to a peak-to-peak pressure change below 0.8 mbar at the helium chamber (see Figure 5.10 (left)). At CRYRING the pressure oscillation translates to a signal in the CCC measurement with a peak-to-peak amplitude of around 45 nA to 60 nA (see Figure 5.10 (right)).

5.3.3 Perturbation by the beam-line

During the tests in the laboratory, the CCC was operated inside a wide-neck cryostat and the area enclosed by the CCC was free of any electric conductors apart from the calibration wire. Inside the beam-line cryostat, the CCC encloses the vacuum beam-line, the helium chamber, the thermal shield and multiple layers of thermal insulation. Although all these elements are interrupted by an electric insulator as they pass through the CCC, still they emit thermal magnetic noise due to thermal movement of charge carriers on their surface (Johnson-Nyquist noise) [69]. Moreover, they can act as an antenna and carry electromagnetic noise to the CCC. Furthermore, the gap in the beam tubes creates a hole in the Faraday cage formed by the cryostat and allows external electric perturbations to enter.

To evaluate the effect of the beam-line cryostat, the performance of the CCC inside the beam-line cryostat was compared to the values obtained in the wide-neck cryostat at the laboratory (refer to Section 4.3). Inside the beam-line cryostat at the CCC test stand at GSI, the maximum amplitude of the voltage modulation (V–Φ) of the SQUID was reduced significantly, which led to a smaller

maximum transfer function of

$$V_{\Phi}^{(\text{beam-line cryostat})} = 153\,\mu\text{V}/\Phi_0\,, \tag{5.5}$$

at an optimal bias current of $I_b = 9.694\,\mu\text{A}$ (compared to $V_\Phi = 318\,\mu\text{V}/\Phi_0$ with $I_b = 9.452\,\mu\text{A}$ in the wide-neck cryostat). A reduction of the amplitude of the SQUID voltage modulation is usually caused due to high-frequency electromagnetic interference. For more information bout the coupling mechanism refer to [29, 70]. A smaller value of V_Φ negatively affects the maximum bandwidth, slew rate and the noise level of the SQUID (see Chapter 2). During the transfer of the beam-line cryostat to CRYRING, the transfer function was reduced further, which indicates that it is not only the cryostat that affects the SQUID, but there is an external component as well. While the gap in the beam-lines is required by design, an alternative rasterized thermal insulation with a small flux noise[10] is available and is planned to be installed during the next maintenance period.

Overall, during this project a versatile cryogenic operating platform was constructed and characterized in order to serve as a test bench for many different CCC detector models and to be used as a prototype for future CCC systems throughout the FAIR accelerator complex. It guarantees a strong damping of external perturbations during the operation at a UHV beam-line and – in the smooth operating mode – offers an excellent temperature stability. There remain some open questions, in particular regarding the long-time operation, however already in the current state it is ready to be operated at the beam-line and enabled the CCC detector to achieve superior current resolutions at CRYRING.

[10] Coolcat 2 NI by RUAG Space GmbH, 1120 Vienna, Austria

Chapter 6

The CCC at CRYRING@ESR

Once the initial tests of the cryogenic support system were completed, the CCC in the radial design and with a high-permeability core was installed at the storage ring CRYRING@ESR to serve as a beam current monitor. After an initial calibration of the detector, beam intensity data for a variety of different ion beams ($^2D^+$, $^{20}Ne^{2/3+}$, $^{16}O^{6+}$, $^{208}Pb^{78+}$, $^{238}U^{91+}$) was collected over the course of half a year. During this time, a low-pass filter was added to the pick-up loop to allow the CCC to cope with higher slew rates.

In this chapter, the performance of the CCC detector is documented and compared to other diagnostic tools at CRYRING. First, the experimental setup – with the CCC inside the cryogenic support system at the beam-line – is presented. Then, the effect of the accelerator environment on the signal of the CCC is discussed. Finally, the results of the measurements of the ion beam are evaluated.

6.1 CRYRING@ESR

The heavy-ion storage ring CRYRING was constructed at the Manne Siegbahn Laboratory (Sweden) in the late 1980s, where it was a key facility for atomic and molecular physics research [71]. In the 2010s, CRYRING became an in-kind contribution to FAIR and thus part of the GSI accelerator facility, where experiments can take advantage of the wide range of ion species and charge states up to bare uranium which the accelerator complex – most notably the Experimental

Circumference	54.18 m
Magnetic rigidity	0.054 to 1.44 T m
Typ. vacuum pressure	$< 1 \times 10^{-11}$ mbar
Acceleration frequency	130 kHz – 2.4 MHz
Injection energy (local injector)	up to 300 keV/u
Beam energies	30 keV – 96 MeV/u (protons) ($E_{max} \approx 96\ (q/A)^2$ MeV/u)
Typ. beam lifetime	3 s – days (depends on ion species)

Table 6.1: *List of basic properties of CRYRING@ESR [72].*

Storage Ring (ESR) – offers as an injector. Table 6.1 gives a list of the basic properties of CRYRING@ESR.

CRYRING@ESR was designed for experiments with highly-charged ions at energies between several tens of keV/u and 96 MeV/u for protons ($E_{max} \approx 96\ (q/A)^2$ MeV/u). An electron cooler is available to improve the beam quality. The accelerating frequency at GSI is 130 kHz to 2.4 MHz. However, the revolution frequency after injection can be as low as a few kHz. Furthermore, it has a local injector which features either an electron cyclotron resonance (ECR) or a duoplasmatron (MINIS) ion source and a radio-frequency quadrupole (RFQ) with an operating frequency of 108.48 MHz ($\frac{m}{q} \leq 2.85$), which accelerates the ions to an energy of up to 300 keV/u.

At the moment, CRYRING hosts several atomic physics experiments [72] and serves as a test environment for the FAIR accelerator control system [73]. In the future, CRYRING might become part of the deceleration chain for antiprotons within the low-energy antiproton program at FAIR [74]. A schematic of the storage ring – including its beam instrumentation – is given in Figure 6.1.

6.2 Experimental setup

The CCC system at CRYRING comprised the CCC detector itself (i), the surrounding beam-line cryostat (ii) and the helium liquefier that was connected to the cryostat from the top. A schematic of the CCC setup is given in Figure 6.2. The liquefier had its own support structure and could be removed temporarily in order to refill the system with liquid helium. The signal of the SQUID was

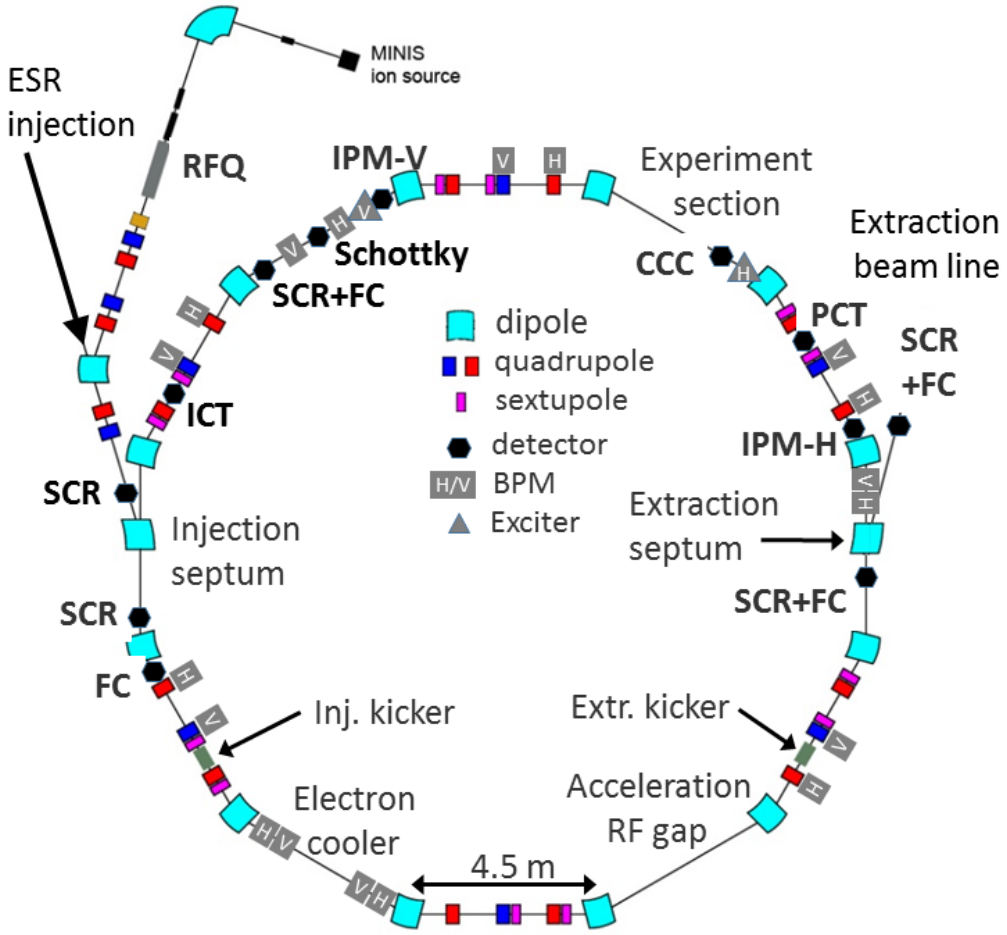

Figure 6.1: *Schematic of CRYRING@ESR [15] including its beam instrumentation. These are Faraday Cups (FC), Beam Position Monitors (BPM), an Integrating Current Transformer (ICT), Scintillation Screens (SCR), Schottky monitor, a Parametric Current Transformer (PCT) and a vertical and horizontal Ionization Profile Monitor (IPM).*

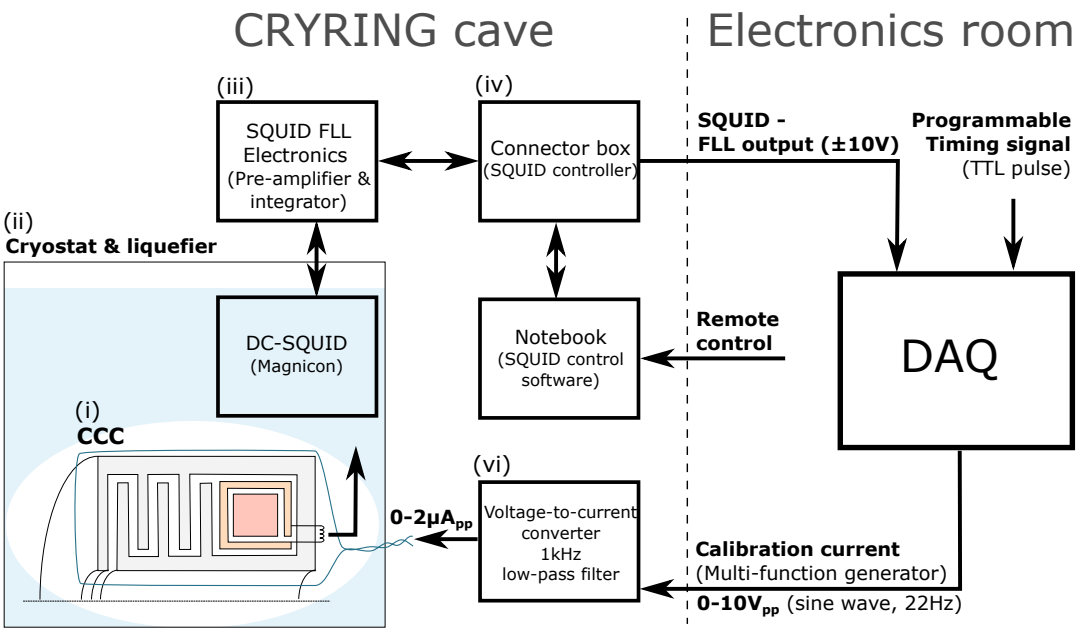

Figure 6.2: *Schematic of the CCC setup at CRYRING.*

read out using the FLL electronics (iii) and the parameters (R_f, GBP) were controlled by a separate connector box (iv). During this experimental run, a notebook next to the accelerator beam-line was used to remotely run the control software of the SQUID supplied by the manufacturer. An overview of the SQUID control software is given in the Appendix A.2. The output of the FLL electronics was sent to a DAQ system at the electronics room.

Throughout the data taking, the cryogenic support system was operated in the smooth operating mode by allowing some excessive gas circulation in order to avoid oscillations of the operating parameter. The subsequent increase of the heat input and of the evaporation rate was tolerated and led to an effective cryogenic operating time of around seven days, which made it necessary to refill liquid helium regularly. In this way, a very stable cryogenic operating environment for the CCC could be provided.

6.2.1 Data acquisition

The CCC was embedded in the data acquisition system of CRYRING based on the Large Analogue Signal and Scaling Information Environment for FAIR (LASSIE) [21]. Figure 6.3 provides an overview of the data acquisition. The

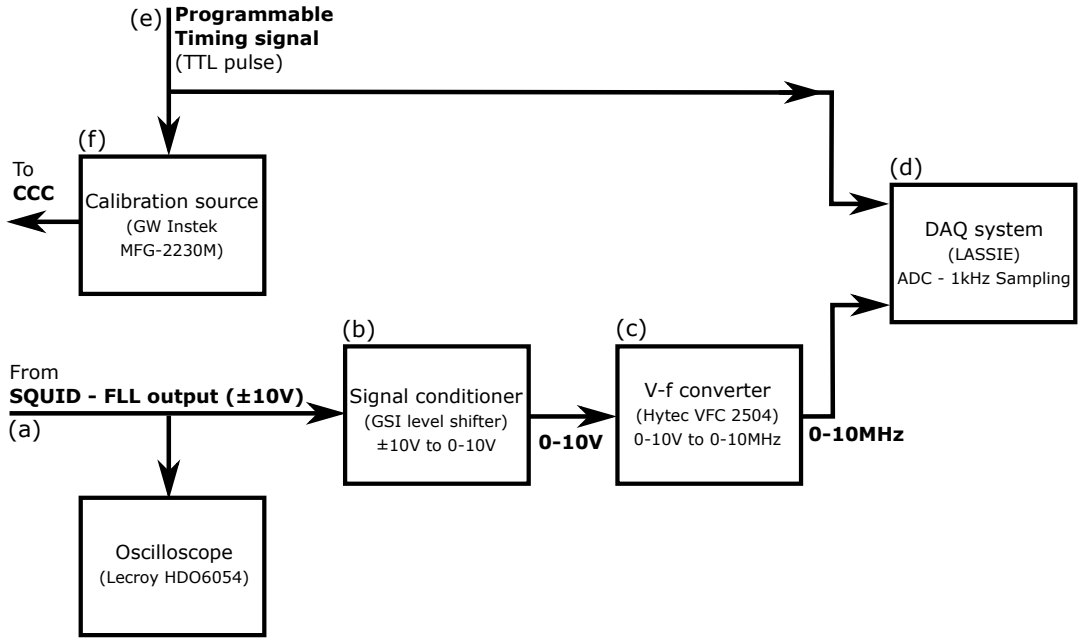

Figure 6.3: *Schematic of the data acquisition at CRYRING.*

output signal after the FLL electronics (a) had a range of ±10 V (10 MΩ termination) and was directed via a semi-rigid RG214 cable from the accelerator cave to a custom-made signal conditioner (b) in the electronics room, which shifted the signal to a positive output range between 0 and 10 V. This was the input range of a voltage-to-frequency converter[1] (c), which transformed the signal to pulses with a frequency between 0 and 10 MHz before it was digitized in the LASSIE scaler system (d).

For each accelerator cycle the output of the CCC could be displayed and saved (with a sampling rate of 1 kHz) for future data analysis together with the signals from other beam diagnostic instruments. Alternatively, the signal of the CCC was often read out directly by a 12-bit oscilloscope[2] during the commissioning. The accelerator control system provided a programmable TTL timing signal (e) connected to the status of the accelerator, which was used to trigger the data acquisition and the function generator (f) that generated a calibration current. The parameters of the FLL readout electronic of the SQUID were controlled independently of the accelerator timing. A specialized control software based

[1]VFC 2504, Hytec Electronics Ltd., UK.
[2]HDO6054 oscilloscope, Teledyne LeCroy

on the Front-End Software Architecture (FESA) used at FAIR is under development in order to control SQUID settings based on the accelerator cycle and to include post-processing algorithms (e.g. baseline correction, signal filters).

6.2.2 Calibration source

Within the cryostat, a single manganin calibration wire with a resistance of 54.6 Ω (during cryogenic operation) passed through the CCC to carry the electric calibration current (see Fig. 6.2). Both ends of the wire loop were accessible through a feed-through on top of the cryostat. The calibration current was generated by a multi-function-generator[3] (MFG) followed by a custom-made passive voltage-to-current converter. While the function generator was located at the electronics hut outside the accelerator cave, the signal converter was installed directly at the cryostat. The converter consisted of a low-pass filter with a cut-off around 1 kHz and a voltage divider which reduced the output of the function generator with a maximum peak-to-peak voltage of 10 V to a voltage in the order of micro-volt. The low-pass filter removed any high-frequency noise which originated in the generator or which was picked up by the long signal cable (> 15 m) between the electronics hut and the position of the CCC. This allowed high-precision, low-frequency calibration current signals with a peak-to-peak amplitude up to around 2 µA.

However, knowledge of the precise calibration current is required for an accurate calibration of the CCC signal. Therefore, the transfer function of the voltage-to-current converter between the input voltage of the function generator and the calibration current through the wire loop was determined during the commissioning. A series of sinusoidal calibration signals ($V_0 \sin(2\pi f t)$) with a peak-to-peak voltage between 0.75 V and 10 V and with a frequency of 0.1 Hz was applied to the voltage-to-current converter. The resulting calibration current was logged with a Keithley 2701 Multimeter for several minutes. Afterwards, the data was fitted with a sine function using gnuplot to extract the peak-to-peak current. Figure 6.4 shows the resulting calibration current as a function of the voltage settings at the function generator. A linear fit of the data points – taking into account the standard error of the measured calibration current –

[3]MFG-2230M, GW Instek, New Taipei City 236, Taiwan

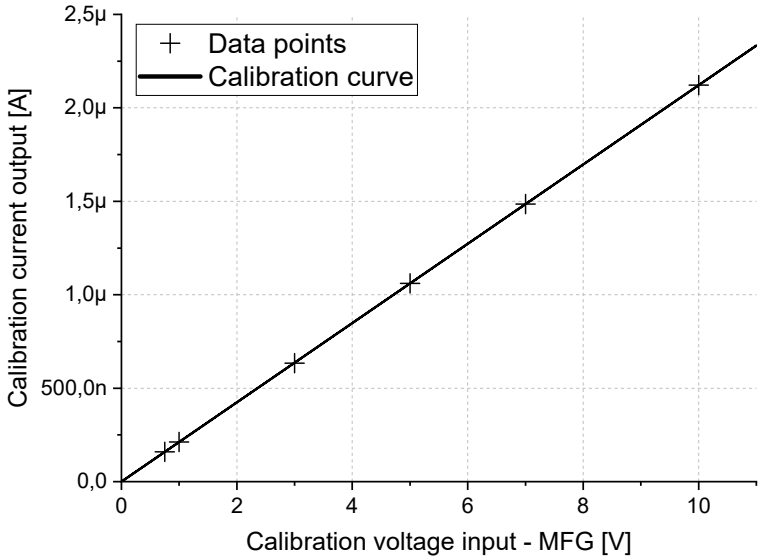

Figure 6.4: *Peak-to-peak calibration current applied to the CCC for a given peak-to-peak input voltage setting at the function generator. The test function was a sine wave with a frequency of* 0.1 Hz. *The current signal was collected by a Keithley 2701 multimeter.*

yields the transfer factor between the peak-to-peak voltage which was set at the function generator and the resulting calibration current of

$$\frac{\mathrm{I_{cal}}}{\mathrm{V_{MFG}}} = (212.1 \pm 0.2)\,\mathrm{nA/V} \qquad \text{for} \qquad f < 1\,\mathrm{kHz}\ . \tag{6.1}$$

6.2.3 CCC calibration

With a well-defined calibration current, the voltage output of the CCC V_{FLL} in FLL mode can be converted to a current I_a through the detector. Time-varying currents in the form of a sine wave with frequencies of 20 Hz, 60 Hz and 200 Hz and with peak-to-peak values between 100 nA and 550 nA were applied to the calibration wire according to

$$I_\mathrm{cal}(t) = I_0 \sin(2\pi f t)\ . \tag{6.2}$$

The amplitude of the resulting SQUID signal was extracted by fitting a sine wave to the output using *gnuplot*. Figure 6.5 shows the resulting peak-to-peak voltage output of the CCC with a feedback resistor of $R_f = 10\,\mathrm{k\Omega}$. A linear fit

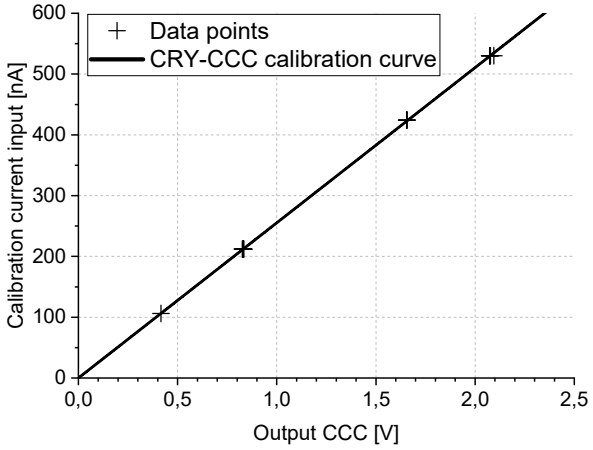

Figure 6.5: *Calibration of the CCC inside the beam-line cryostat valid for a feedback resistor* $R_f = 10\,\mathrm{k\Omega}$ *and for frequencies below* 10 kHz.

R_f [kΩ]	I_{beam} [nA/V]	Meas. range [µA]
0.7	3648 ± 3	73
1	2553 ± 2	51
3	851.1 ± 0.7	17
7	364.8 ± 0.3	7
10	255.3 ± 0.2	5.1
30	85.11 ± 0.07	1.7
100	25.53 ± 0.02	0.51

Table 6.2: *List of calibration factors and of the measurement range for different* R_f*. The available measurement range was calculated assuming the full use of the available output range of the SQUID of* $\pm 10\,\mathrm{V}$.

of the obtained data points confirmed the linear response of the CCC at this input amplitudes and was used to extract the final signal calibration. The errors of the calibration current input and of the SQUID voltage measurement were taken into account as part of the fitting routine. With a feedback resistor of $R_f = 10\,\mathrm{k\Omega}$ – which is in the middle of the available parameter range – the conversion factor was determined to be

$$\frac{\mathrm{I_{beam}}}{\mathrm{V_{FLL}}} = (255.3 \pm 0.2)\,\mathrm{nA/V} \quad \text{with} \quad R_f = 10\,\mathrm{k\Omega}\ . \tag{6.3}$$

The error of the calibration corresponds to a stochastic uncertainty of the measured current of $\pm\,0.08\,\%$. Please note, that this calibration factor could only be confirmed for input current signals with a frequency below the cut-off frequency of the low pass filter of the voltage-to-current converter of 1 kHz. However, it is expected to be valid up to frequencies of 10 kHz. At larger frequencies, the decline of the magnetic permeability of the high-permeability core and the influence of the flux transformer will lead to a different frequency-dependent calibration factor. For different feedback resistors the conversion factor scales linearly according to $U = R\,I$. The corresponding calibration factors for a selection of feedback resistors R_f are listed in Table 6.2.

The determined value is subject to multiple systematic errors, some of which are the deviation of the output of the measurement devices from the metrological

current/voltage standard and signal drifts of the equipment, in particular of the custom-built voltage-to-current converter. Moreover, the surrounding beam-line cryostat – and most notable the beam tubes enclosed by the CCC – can affect the magnetic flux created by the calibration pulse at the CCC, such that a small deviation of the calibration factor for the value determined inside the wide-neck cryostat at University Jena was observed.

6.2.4 Signal background

Before there was any beam injected into CRYRING, the stability and the current noise of the CCC were investigated with all accelerator components in routine operation. Figure 6.6 shows the CCC data collected in a background measurement during one accelerator cycle with a duration of around 30 s. For this measurement the helium liquefier was switched off. Moreover, the dc component of the ambient magnetic field was static in the time between the magnetic ramps of the dipole (signal dips at the start and the end of the cycle) and the output of the CCC was not affected.

With the major noise contributions removed, the baseline drift throughout a typical accelerator cycle can be determined. Whenever the operating environment was stable and the cryogenic support system was in equilibrium, there were very little variations of the temperature and of the pressure such that the drift of the baseline of the signal was confined to

$$\Delta I_{\mathrm{drift}} \leq 30\,\mathrm{pA/s}\ . \tag{6.4}$$

However, much larger drifts were observed when the temperatures inside the cryostat were changing. In the future, drifts that originate in a change of temperature or pressure will be corrected using the temperature and pressure monitoring of the cryogenic support system.

At the same time, the typical current noise I_{rms} of the CCC signal can be quantified in terms of the root mean square of the measured time series. Without the perturbation of the liquefier and of the dipole ramp, the root mean square

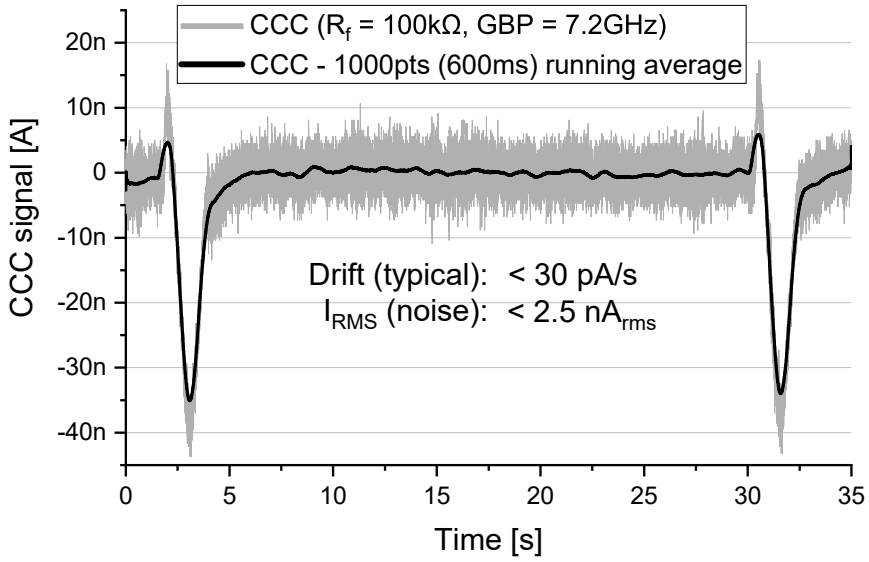

Figure 6.6: *Background measurement without the liquefier and during an empty accelerator cycle with the maximum sensitivity and largest gain-bandwidth-product ($R_f = 100\,\mathrm{k\Omega}$ and $GBP = 7.2\,\mathrm{GHz}$). The average baseline drift with a constant dipole field and with the cryogenic setup in equilibrium was below $30\,\mathrm{pA/s}$. At a bandwidth of $10\,\mathrm{kHz}$ the measured current noise I_{rms} was below $2.5\,\mathrm{nA}_{rms}$.*

of the CCC data throughout the beam time was

$$\mathrm{I_{rms}} = \sqrt{\frac{1}{n}\sum_{i}^{n} x_i^2} \;\leq\; 3.2\,\mathrm{nA_{rms}}\ . \tag{6.5}$$

Since the arithmetic mean of the selected data was zero, the determined value is equivalent to the standard deviation of the signal. The noise level fluctuated with the amount of perturbations from the environment and may be lower than $3.2\,\mathrm{nA_{rms}}$ as depicted in Fig. 6.6. The current noise leads to a signal-to-noise ratio (SNR) for a current signal of $10\,\mathrm{nA}$ of

$$\mathrm{SNR}_{10\,\mathrm{nA}} = \left(\frac{I_{signal}}{I_{noise}}\right)^2 = \left(\frac{10\,\mathrm{nA}}{3.2\,\mathrm{nA}}\right)^2 = 9.8\ . \tag{6.6}$$

6.3 Operating environment

The CCC system was installed close to the center of the experiment section of CRYRING (see Figure 6.7). The accelerator environment – with a multitude of electromagnetic and mechanical noise sources – imposed a set of perturbations on the detector system, which affected the performance of the SQUID sensor and reduced the noise-limited current sensitivity of the CCC.

6.3.1 SQUID performance deterioration

It is well documented, that high-frequency electromagnetic interference negatively affects the amplitude of the voltage modulation ($V-\Phi_a$) of the SQUID and thus its operating performance (e.g. maximum bandwidth, intrinsic flux noise) [29, 70]. Such an additional reduction of the voltage modulation – and thus the transfer function $V_\Phi = |\partial V_{sq}/\partial\Phi_a|$ – was observed after the cryostat was moved from the laboratory to the beam-line. Figure 6.8 shows the modulation of V_{sq} with an applied current $\mathrm{I}_\Phi^{(\mathrm{fb})}$ at CRYRING. There, the maximum transfer

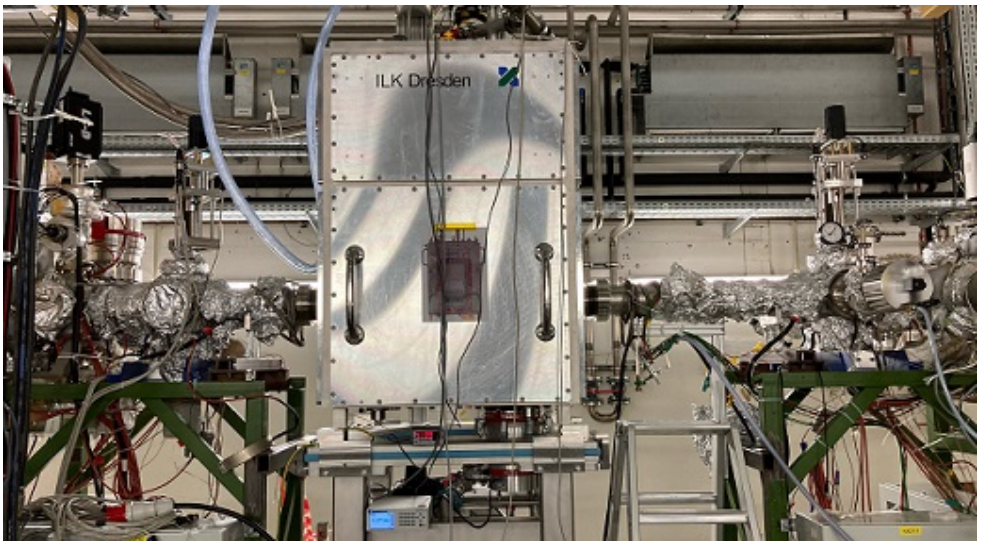

Figure 6.7: *The CCC system installed at CRYRING@ESR. The cryostat is mechanically decoupled from the beam-line by diaphragm bellows and from the sand-filled support frame by a rubber mat (blue). Maintenance windows allow access to the CCC. The beam enters from the right.*

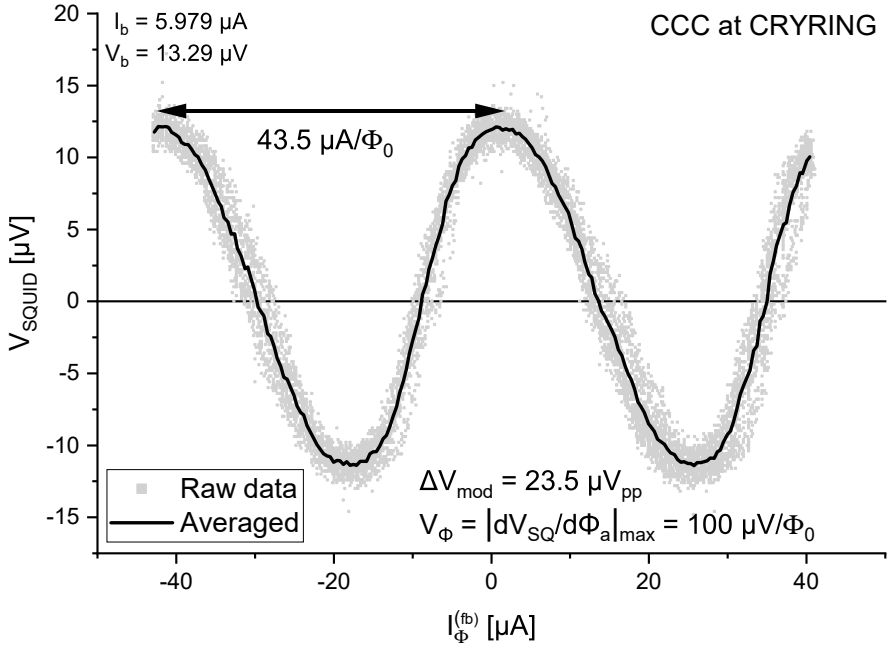

Figure 6.8: *Periodic modulation of the voltage V_{sq} across the SQUID (pre-amplifier gain of* 2000*) with an applied current $I_\Phi^{(fb)}$ through the feedback coil. During the data taking the CCC was installed inside the beam-line cryostat at CRYRING.*

function was reduced from $153\,\mu\mathrm{V}/\Phi_0$ to

$$V_{\Phi,\,\mathrm{CRYRING}} \approx 100\,\mu\mathrm{V}/\Phi_0\ . \tag{6.7}$$

As a result, the maximum unity-gain frequency f_1 with stable SQUID operation was 13 MHz (with $R_f = 0.7\,\mathrm{k}\Omega$ & $GBP = 4\,\mathrm{GHz}$). However, the bandwidth $f_{3\,\mathrm{dB}}$ of the FLL readout with the lowest intrinsic current noise was still limited by the loop delay to below 9 MHz. A list of the estimated maximum slew rates for all possible combinations of R_f and GBP using the reduced transfer function is given in Table A.1 in the Appendix.

In addition, the reduction of V_Φ increased the effect of the intrinsic voltage noise $S_{V\,\mathrm{AMP}}$ of the pre-amplifier of the FLL electronics and led to a corresponding flux noise density of $\sqrt{S_{\Phi,\,\mathrm{AMP}}} = \sqrt{S_{V,\,\mathrm{AMP}}}/V_\Phi = 3.3\,\mu\Phi_0/\sqrt{\mathrm{Hz}}$ (cf. Eq. (2.19)). Together with the intrinsic flux noise of the SQUID itself, a total SQUID-related noise density of $5.3\,\mu\Phi_0/\sqrt{\mathrm{Hz}} = 0.53\,\mathrm{pA_{rms}}/\sqrt{\mathrm{Hz}}$ was calculated for frequencies above 1 Hz. However, even after the increase of the noise contribution of the

SQUID, it was still much smaller than the noise from the high-permeability core. Furthermore, the optimal bias current I_b with the largest V_Φ was reduced significantly from $I_b = 9.45\,\mu A$ in the laboratory to $I_b = 5.98\,\mu A$ at CRYRING. Such a behavior is not well-documented in literature and further investigations are necessary to determine the mechanism behind this deterioration.

6.3.2 Dipole perturbation

The most apparent signal perturbation at CRYRING was caused by the dipole magnets. Two dipole magnets enclosed the experiment section and ramped up to a nominal field strength of up to 1.2 T during the acceleration. The overall deviation of the magnetic field at the location of the CCC – at a distance from the dipole of about 1 m – was measured by a Hall sensor to be in the order to 50 µT. The change of the magnetic field was strongly attenuated by the superconducting shield of the CCC. However, the remaining change of the field led to a perturbation of the CCC signal with an amplitude equivalent to 23 nA. Figure 6.9 shows the field strength of the dipole magnets during the acceleration at CRYRING and the output signal of the CCC.

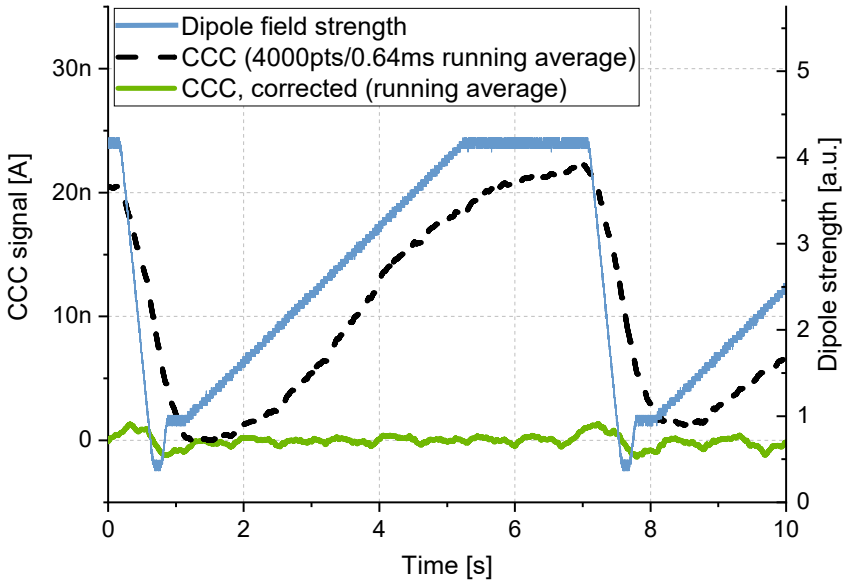

Figure 6.9: *The strength of the dipole magnets at CRYRING (blue, right y-axis) measured by a Hall sensor, compared to the resulting background perturbations of the CCC before (dotted black) and after (solid green) the background correction.*

Due to the orientation of the CCC detector, the signal induced by the dipole had the opposite polarity compared to the signal from the ion beam. The shape of the perturbation followed the rise of the magnetic field and was identical for subsequent acceleration cycles as long as the same parameters for the magnetic ramp (ramp speed, ramp duration, length of plateaus) were used. Therefore, the perturbation created by the dipole was cataloged before the measurement run and could be subtracted from subsequent measurements to successfully remove the influence of the dipole. The characterization of the background – including the data shown in Fig. 6.9 – was performed with no beam in the storage ring, but with all accelerator components (including the dipoles and the acceleration cavity) in operation. An attempt to find a universal transfer function – which can be applied to arbitrary magnetic ramps without the need of performing dedicated background measurements – was not yet successful.

6.3.3 Noise current spectral density

In addition to the perturbation by the dipole magnets and by the liquefier, the CCC was affected by a significant level of broadband noise. At the beam-line, the floor of the noise current spectral density at frequencies above 100 Hz was measured to be around $40\,\mathrm{pA_{rms}}/\sqrt{\mathrm{Hz}}$, which was notably higher than the level inside the wide-neck cryostat and inside the magnetically shielded room in Jena of $3\,\mathrm{pA_{rms}}/\sqrt{\mathrm{Hz}}$ (cf. Fig. 4.9). The measured noise spectrum at CRYRING across the operating bandwidth of the CCC is shown in Fig. 6.10. If known, the peaks in the noise spectra are labeled with their corresponding source. The resonance of the pick-up circuit produced a broad peak around 170 kHz.

Some of the perturbations did not originate from the CRYRING environment but either were created by the CCC setup itself (e.g. the cryogenic support system) or they were eigenmodes of the setup driven by the environment. Particular attention was given to proper shielding of instrumentation cables and their connectors against electromagnetic interference. Ground loops did not seem to be a particular problem since the noise spectrum was largely unaffected when all electric components, which would drive the ground loops, were disconnected from the system. Extensive investigations with an isolation transformer showed no significant improvement.

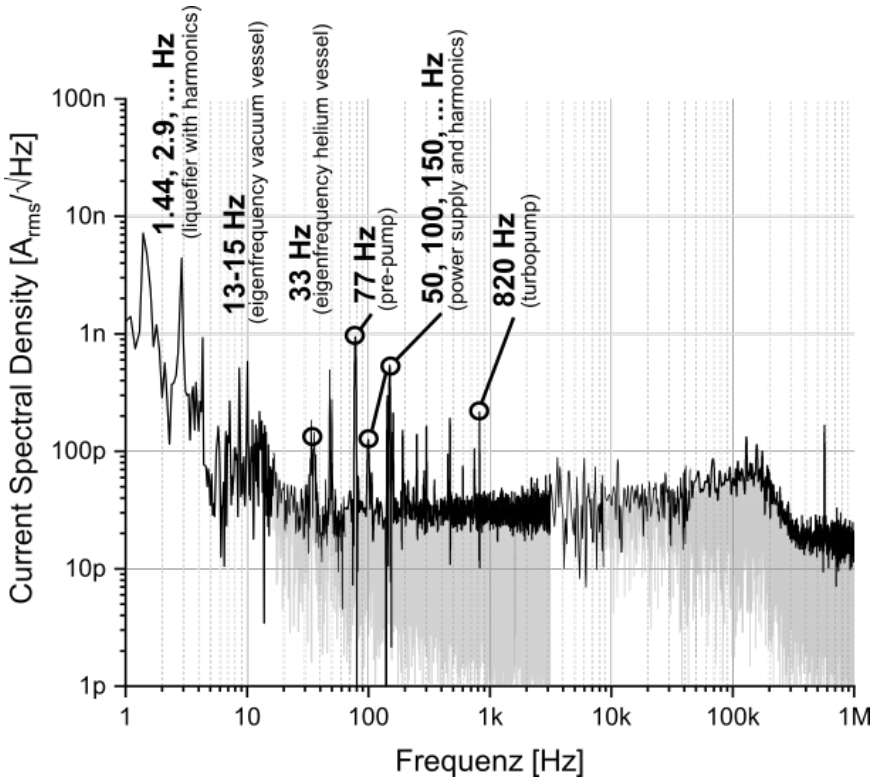

Figure 6.10: *Noise current spectral density of the CCC at CRYRING calculated from two different time series using a Fourier transformation. Wherever possible, known perturbation sources are marked. The resonance of the pick-up circuit is visible at* 170 kHz*.*

No single noise source to explain the significant increase of broadband noise could be identified in the scope of this thesis and an interference of the combined electromagnetic background at the CRYRING beam-line is assumed. In particular the increase of the noise around the resonance frequency – where ambient radio-frequency interference can couple into the system most effectively – can be explained in this way. Moreover, high-frequency interference can be responsible for low-frequency noise components in the SQUID spectrum as well, as is presented here [29, 70].

6.3.4 Liquefier perturbation

The final characterization of the CCC system and the test of the filtering methods for the perturbation by the helium liquefier were performed with a set of

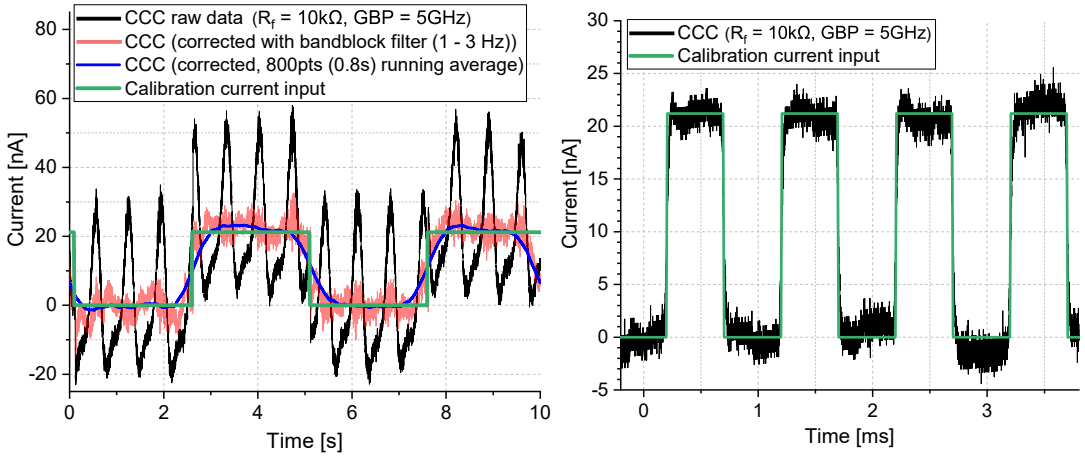

Figure 6.11: *CCC measurement of two square wave tests signals with a peak-to-peak current of* 21.2 nA *and frequencies of* 0.2 Hz *(left) and* 1 kHz *(right). For long measurement times the perturbation introduced by the liquefier was removed with a digital band-stop filter.*

test signals applied to the calibration line. Figure 6.11 shows the response of the CCC to a calibration current in the form of a square wave with a peak-to-peak current of 21.2 nA and with two different frequencies of 0.2 Hz and 1 kHz.

With short measurement times (right hand side of Fig. 6.11), the low-frequency perturbation of the liquefier is less apparent. In this example the standard deviation of the signal was determined to be 2.2 $\mathrm{nA_{rms}}$. However, with measurement times larger than a few milliseconds the perturbation of the liquefier significantly affected the measurement. The perturbation was periodic ($f = 1.44$ Hz) with a sine-like structure and, therefore, a digital band-stop filter with a stop-band between 1 to 3 Hz was used to remove its first and second harmonic, which formed the majority of the perturbation signal. After the correction, the standard deviation (rms) of the CCC signal was successfully reduced to 3.2 $\mathrm{nA_{rms}}$.

In general, the noise figure of the corrected current measurement was very close to the noise of signals which were taken without the liquefier (see Eq. (6.5)). While this method led to a clear improvement of the signal, the filter also removed a small part of the actual current signal. As a result, when there were sharp rising or declining edges, the filter could lead to artifacts in the measurement with the time scale of the filter. However, these artifacts have a substantially smaller amplitude than the original perturbation by the liquefier.

6.4 Intensity measurement with beam

During the beam time CRYRING was commissioned and operated with several different ion species with beam currents between 5 nA up to roughly 20 µA in order to fulfill the demands of the experiments. Table 6.3 shows a list of ions which were used in experiments at CRYRING and which were measured by the CCC.

6.4.1 Boundary conditions

For the measurement of the ion current the SQUID was operated in FLL mode. Then the CCC provides a current measurement relative to a reference (working) point, which is defined in the moment when the SQUID enters the feedback loop. At the reference point the output signal of the FLL electronics is zero volt. Usually, the flux-lock was activated when there was no beam inside the ring, which means that an output of zero volt was equivalent to an empty ring. As soon as any ions were injected in the ring, the FLL electronics tracked the beam current throughout the accelerator cycle and returned back to the zero baseline when there was no more beam stored in the ring. Therefore, the voltage output of the CCC is linearly proportional to the current deviation from the reference point. For signals with a frequency component that is larger than the bandwidth of the CCC pick-up circuit, their high-frequency component was strongly attenuated and only their low frequency components were detected. This was the case for the majority of bunched beams.

However, the baseline of the CCC measurement was not entirely stable during long term operation and there was a small drift due to temperature or pressure variations (e.g. day-night cycle) (see Sec. 6.6). Moreover, current offsets (flux jumps[4]) were observed in case the feedback loop was confronted with signals that exceeded its slew rate limit. These effects led to an offset of the output signal which was corrected in the digital post-processing or by regularly resetting

[4]Flux jumps of the SQUID are caused by large slew rates (or high frequency components) of the beam signal, which exceed the feedback capabilities of the FLL electronics. As a result, the working point along the voltage modulation is lost temporarily, until the slew rate decreases to nominal values and the feedback loop is able to lock to a new, different working point. With the loss of the original working point, the reference point to allow an absolute current measurement is lost.

Ion	Max. current	Stored particles	Max. energy [MeV/u]
$^{2}D^{+}$	15 µA	$2.0 \cdot 10^{8}$	5
$^{20}Ne^{2+}$	150 nA	$8.3 \cdot 10^{6}$	0.98
$^{16}O^{6+}$	100 nA	$5.1 \cdot 10^{5}$	10
$^{208}Pb^{78+}$	15 µA	$2.0 \cdot 10^{7}$	11.34
$^{238}U^{91+}$	20 µA	$2.6 \cdot 10^{7}$	10

Table 6.3: *List of ion beams measured with the CRY–rCCC at CRYRING.*

the flux-locked loop (defining a new zero-voltage reference point). During the measurement campaign, this reset was done manually between accelerator cycles whenever the offset became too large. In the future, this can be automatized to define a new baseline at the beginning of every accelerator cycle.

6.4.2 Full bandwidth measurements

Following the characterization with artificial calibration signals, the CCC was tested with a deuterium $^{2}D^{+}$ beam from the local ion source which had routinely been used at CRYRING for commissioning and machine tests. It was well known to the operators and allowed for storage and acceleration of a wide range of beam intensities. During the measurement run, the energies of the $^{2}D^{+}$ ions were between 0.3 MeV/u at injection and 5 MeV/u at the flat top after the acceleration. Starting at an intensity at the flat-top of around 10 µA, the current amplitude of consecutive acceleration cycles was reduced step-wise down to 6 nA.

Figure 6.12 shows the measurement of a stored $^{2}D^{+}$ beam with a maximum current at the flat top close to 80 nA. With the maximum bandwidth of the CCC of around 200 kHz, the injection (multi-turn injection of 10 bunches) is visible as a sharp jump in the dipole-corrected data. Following the injection, the beam was bunched by the RF cavity at a revolution frequency of roughly 130 kHz. At this revolution frequency, the CCC can partly resolve the individual passing of the single stored bunch, which is visible as an oscillation of the CCC current signal and which is responsible for the broad signal envelope visible for several seconds following the injection.

After bunching, the beam was accelerated to 5 MeV/u (f_{rev} = 405 kHz) and the revolution frequency became larger than the bandwidth of the CCC such

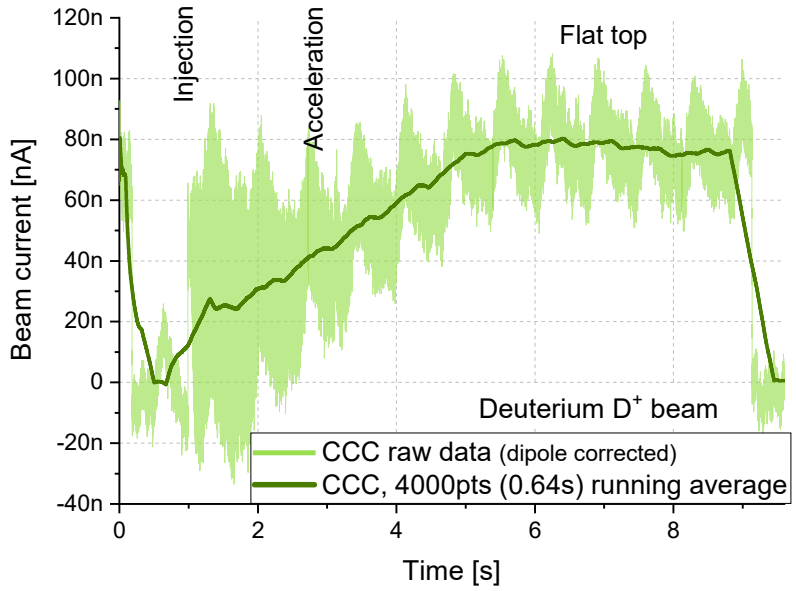

Figure 6.12: *Stored, bunched $^2D^+$ beam at CRYRING measured by the CCC with an intermediate feedback sensitivity and a large gain-bandwidth-product ($R_f = 7\,\mathrm{k\Omega}$, $GBP = 5\,\mathrm{GHz}$). The dipole correction was applied. The perturbation by the liquefier is shown.*

that only the low-frequency current deviations were measured. During the acceleration the beam current amplitude rises due to the increasing velocity of the ions. At the flat top, the RF cavity remained active and thus the stored ions continued to be bunched. The prominent oscillation of the signal ($f = 1.44\,\mathrm{Hz}$) was created by the liquefier. At the end of the beam cycle, the field strength of the dipole steering magnets was ramped down which led to a controlled beam loss distributed throughout the walls of the beam-line of the entire storage ring. In the CCC, the beam dump was visible as a jump from the current at the flat top down to the zero current baseline.

In summary, it was shown that the CCC can successfully track the current amplitude of low-intensities beams across the entire acceleration cycle. At small revolution frequencies, it was possible to observe the time-structure of the bunched beam. In case only the dc component of the beam is of interest, a low-pass filter (e.g. with a cut-off frequency at 100 Hz) can be installed after the FLL electronics to remove high-frequency beam components and to improve the current noise of the measurement. Alternatively, a running average can be calculated (shown as dark green curve in Fig. 6.12) in order to smooth the data and thus

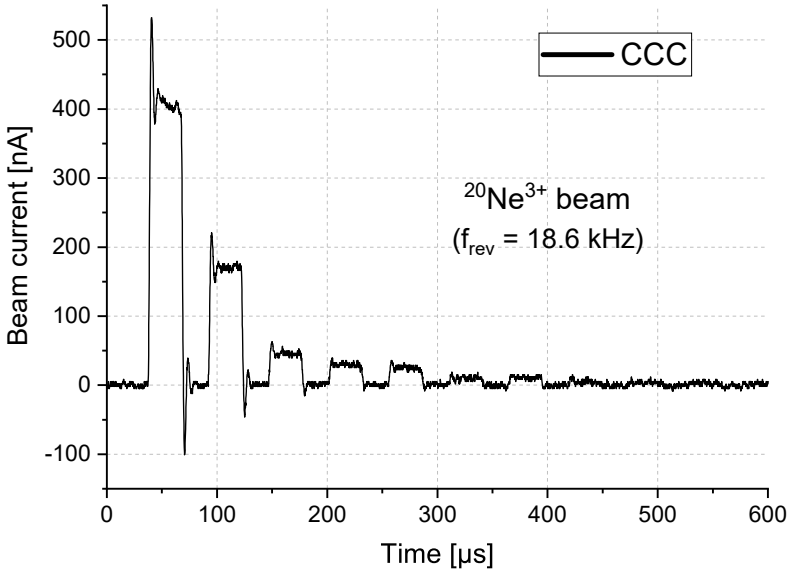

Figure 6.13: *First turns of a $^{20}Ne^{3+}$ beam at CRYRING during the commissioning immediately after injection (f_{rev} = 18.6 kHz). FLL readout with an intermediate feedback sensitivity and the maximum gain-bandwidth-product (R_f = 3 kΩ, GBP = 7.2 GHz).*

remove perturbations. The running average for a given point p is defined as the arithmetic mean of all data points within an averaging window w (in this case w = 0.64 s, equivalent to 4000 data points) around p. At the beginning and at the end of the data set, the averaging window became smaller such that the first and the last point of the data only had a one-sided averaging window of $w/2$ = 0.32 s.

In the (rare) case that the revolution frequency of the ions was much smaller than the bandwidth of the detector, the CCC could be used to measure the individual bunches. Figure 6.13 shows the signal from a single bunch of low-energy $^{20}Ne^{3+}$ ions immediately after the injection from the local ion source. The measured ion bunch filled about half of the circumference of the ring and circulated with a frequency of 18.6 kHz. Since at that point during the commissioning the ring was not yet optimized to store the neon beam, there was a large beam loss which produced the strong decline of the measured current amplitude with each revolution in the ring. The large slew rate of the ion bunch led the feedback loop of the FLL electronics to overshoot, followed by some ringing as it succeeded to maintain the stable working point. This measurement demonstrates the band-

width of the CCC up to 200 kHz for transfer-line applications (e.g. beam-loss monitoring, slow-extracted beam) and for beam commissioning.

6.4.3 Small current amplitudes

At very low beam intensities below 10 nA the intrinsic noise of the CCC became relevant. At these amplitudes it was required that both the perturbations of the dipole and of the liquefier were removed before a meaningful beam current could be extracted from the measurement. Moreover, care had to be taken to define an accurate zero-current baseline. Ideally, a time window of several seconds with an empty ring (e.g. after the dump) was dedicated to perform the baseline calibration. Otherwise, the uncertainty of the baseline was a major limitation for the accuracy of the absolute measurement.

Figure 6.14 shows the beam intensity of a weak $^2D^+$ beam with a maximum current close to 10 nA throughout the accelerator cycle. The small oscillation at the end of the flattop is an artifact of the band-stop filter which removed the liquefier noise. In this example, the standard deviation of the CCC signal was $I_{\mathrm{rms}} = 2.4\,\mathrm{nA}$. Assuming a constant beam intensity at the flat-top (5.4 s and 7 s), there the mean beam intensity was determined with a linear fit to be

$$\langle I_{beam} \rangle_{t,\,\text{flat-top}} = \left(11.73 \pm 0.01^{(\text{rand})}_{\text{calibration}} \pm 0.02^{(\text{rand})}_{\text{flat-top}} \pm 0.03^{(\text{rand})}_{\text{baseline}}\right) \text{nA} \ . \quad (6.8)$$

All errors are $1\,\sigma$ standard errors, which amounts to a total error of the signal of 0.6 %. The baseline was determined as the mean of the measured current in the time before the injection (0 s and 0.95 s) and after the dump (9.6 s and 9.85 s). The systematic error due to the typical linear drift of the baseline throughout the entire measurement time of 10 s was calculated to be in the order 0.3 nA (peak-to-peak) and is not included in the errors above (cf. Eq. (6.4)). However, performing measurements of the baseline before and after the accelerator cycle potentially allows for a correction of any linear drift error.

Overall, an excellent low-intensity current resolution could be shown with beam. In case one is mainly interested in the low frequency dc component of the stored beam, low-pass filtering after the FLL electronics can further improve the measurement resolution. Alternatively, the mean beam current is depicted as the

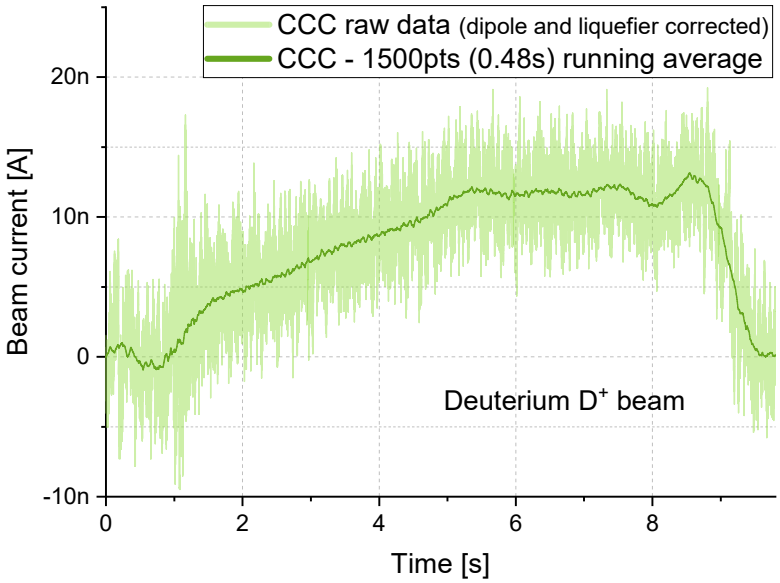

Figure 6.14: *Stored $^2D^+$ beam at CRYRING. Both the dipole correction and the liquefier band-stop filter are applied. Readout with a large feedback sensitivity and an intermediate gain-bandwidth-product ($R_f = 23.1\,\mathrm{k\Omega}$ and $GBP = 1.04\,\mathrm{GHz}$).*

running average (dark green curve in Fig. 6.14) with a standard deviation of the signal of $0.2\,\mathrm{nA_{rms}}$.

6.4.4 Limitations at large current amplitudes

First and foremost, the CCC is designed to measure the current amplitude at small beam intensities ($\ll 1\,\mu\mathrm{A}$). While it is attractive to have a single device which can be used on the entire intensity spectrum at CRYRING, using the CCC with beam intensities larger than 500 nA (see Table 6.2) will reduce the available signal resolution. The large dynamic range – which is required to monitor local changes of the beam current in the order of nA while at the same time keeping track of the absolute beam current of tens of µA – puts unrealistic demands on the ADC that is used to process the output of the CCC. While the SQUID (with the FLL readout) offers a large dynamic range, in the majority of cases it is the ADC which limits the achievable current resolution. Moreover, with increasing amplitudes it becomes more likely that changes of the beam current exceed the slew rate limitation of the FLL electronics. Therefore, it is always a compromise between the requested measurement range and the achievable cur-

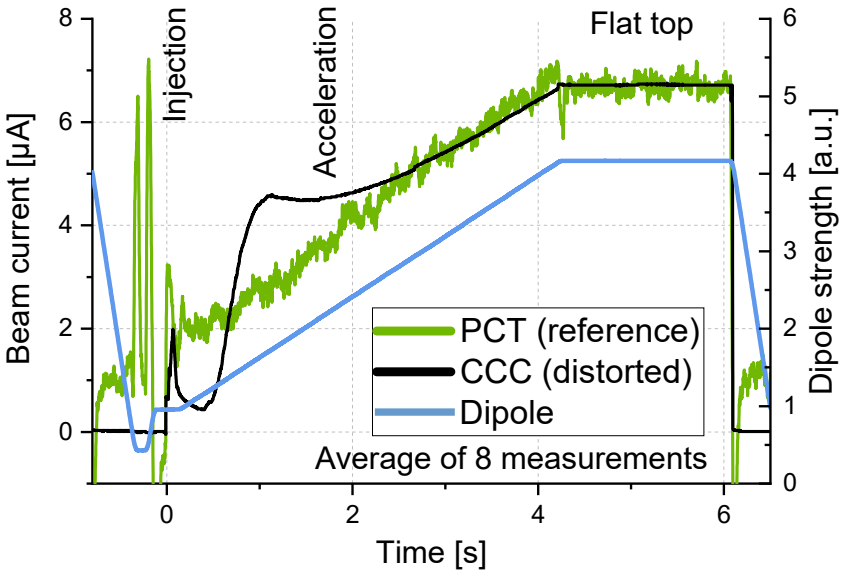

Figure 6.15: *Average of eight consecutive measurements of stored bunched $^2D^+$ beam by the CCC (black) with a small feedback resistor and gain-bandwidth-product ($R_f = 0.7\,\mathrm{k\Omega}$, $GBP = 0.23\,\mathrm{GHz}$) and by the PCT (green). The field strength of the dipole magnets is given in blue. The voltage output of the PCT was converted to current via the calibration factor* $100\,\mu\mathrm{A/V}$. *After the injection the output of the CCC is distorted due to the large slew rate of the beam current.*

rent resolution. Future measurement configurations with two parallel SQUIDs of different sensitivities might be able to circumvent this situation.

In practice, to capture a large current signal with the static input range of the ADC, a small feedback resistor R_f needs to be selected (cf. Tab. 6.2). The high-intensity limits of the CCC were investigated with a bunched beam of $^2D^+$ from the local ion source. During the injection the estimated slew rate of the beam current was as high as $5\,\mathrm{mA/\mu s}$, taking into account a measured rise time of the particle bunch of around 10 ns and an amplitude of around $50\,\mu\mathrm{A}$. In case a cooled beam is injected from the ESR the current rise times can be even many magnitudes larger. However, the amplitude of the high-frequency signal (and thus the slew rate) at the SQUID was strongly reduced by the declining inductance of the high-permeability core (e.g. factor 10 at 1 MHz) and the diminished gain of the pick-up circuit (e.g. factor 30 at 1 MHz) at larger frequencies. Even with this reduction of the slew rate, the signal at the SQUID still exceeded the limitation of the FLL electronics ($\dot{\Phi}_{f,\,\mathrm{max}} \lesssim 400\,\mathrm{nA/\mu s}$).

Figure 6.15 shows the average of eight consecutive measurement of the $^2D^+$ beam with an amplitude at the flat-top of around 6.5 µA. The signal from the CCC is compared to the signal from the PCT, which was used as a reference. For the PCT the measured currents were close to its detection limit (standard deviation of 1.9 μA_{rms}) and the averaging of multiple accelerator cycles was required to extract a meaningful current signal. Moreover, it had a varying offset, which was corrected by aligning the flat-top with the flat-top measured by the CCC.

The large slew rates of the ion beam at injection and of the bunches during the acceleration (f_{rev} = 130 kHz to 405 kHz) led to a distortion of the CCC measurement. For the majority of the accelerator ramp, the active feedback of the FLL could not keep a stable operating point and the output of the CCC did not follow the linear increase in current measured by the PCT. In particular at the injection, the flux jump led to an arbitrary offset of the current measurement and a loss of the zero-current baseline. In contrast, the beam dump led to a smaller slew rate at the SQUID and was resolved accurately in all the performed measurements. Therefore, the measurement of the empty ring after the dump can be used to assign an absolute scale to the current measurement of the CCC.

A quicker recovery of the working point along the accelerator ramp was achieved by reducing the bandwidth of the FLL electronics (selecting smaller values for R_f and GBP). In general, the active feedback loop is able to ignore certain high-frequency perturbations (e.g. due to the bunching of the beam) without losing its working point, as long as the noise frequency is larger than its maximum operating bandwidth [49]. With a reduced bandwidth, lower noise frequency could be ignored and thus a faster recovery of the working point was observed.

In summary, the CCC lost its absolute calibration when it was confronted with excessive slew rates of high-intensities signals. However, as soon as the slew rate decreased to nominal values, the signal was tracked accurately. During regular operation the beam dump was resolved correctly and allowed for the absolute current calibration to be restored, using the signal baseline of the empty ring after the beam dump. Therefore, with adequate signal processing an absolute measurement of high-amplitude beams throughout the majority of the beam cycle could be achieved.

6.4.5 System adaptation

With the goal to increase the maximum slew rate of the system, a low-pass filter was introduced to the pick-up circuit of the CCC. In this way, high-frequency components are strongly attenuated before they reach the SQUID and, thus, cannot disrupt the feedback loop. The filter was connected in series to an internal calibration line which offered the possibility to couple inductively to the pick-up circuit. The single-wire loop is incorporated inside the niobium shield of the CCC and winds around the pick-up coil (see Figure 6.16).

Any resistor of the filter introduces some amount of thermal (Johnson-Nyquist) noise (see Eq. (1.1)) and will degrade the ultimate current resolution of the CCC. Therefore, the advantages of a larger maximum slew rate should be weighted against the decrease in measurement resolution, before such a filter is installed. To estimate the resulting transfer function of the low-pass filter and the amplitude of the additional current noise, the modified pick-up circuit was simulated using the electric circuit simulator *LTspice*. Figure 6.16 gives the wiring diagram of the simulated circuit.

The results of the simulation (R_{lp} between $0.2\,\Omega$ to $2\,\Omega$ & $C_{\mathrm{lp}} = 10\,\mu\mathrm{F}$) are provided in Fig. 6.17. The smaller the resistance, the more the cut-off frequency is reduced. In order to keep the additional noise to a minimum, a low-pass filter based on a resistance of $2\,\Omega$ and without any additional capacitor was selected.

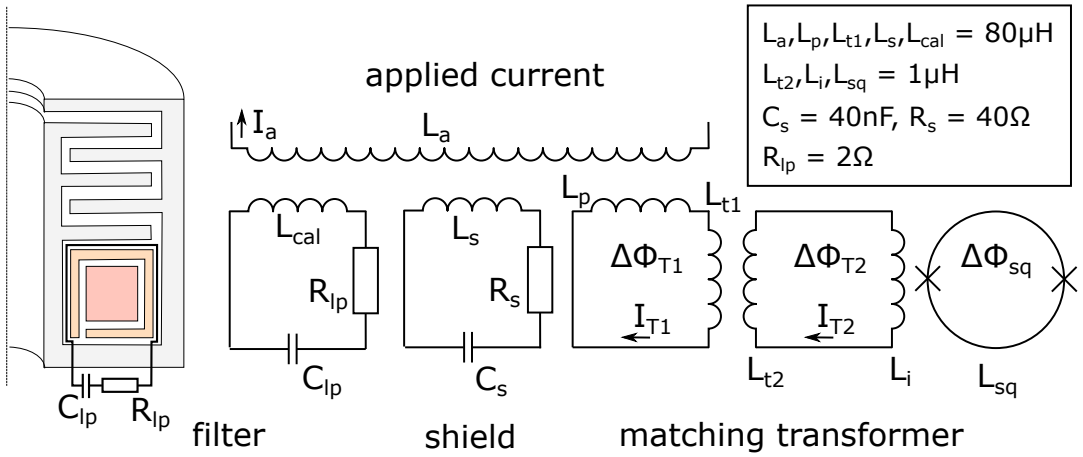

Figure 6.16: *Wiring diagram of the CRY–rCCC pick-up circuit with core simulated in LTspice for $R_{lp} = 0.2\,\Omega$ to $2\,\Omega$ and with and without a capacity $C_{lp} = 10\,\mu\mathrm{F}$.*

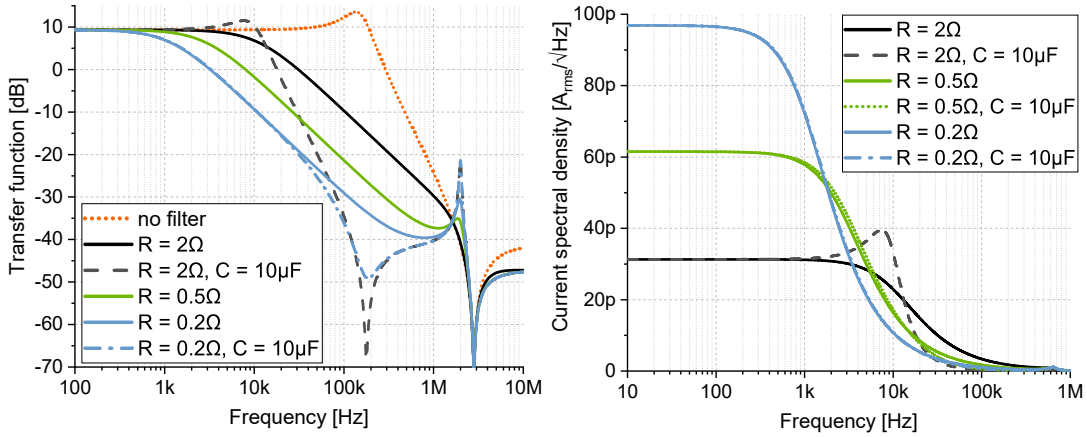

Figure 6.17: *The influence of a resistance R_{lp} and a capacity C_{lp} connected to the internal calibration winding on the transfer function (left) and on the noise level due to the thermal noise of the resistor at* 4 K *(right).*

The filter lowers the expected cut-off frequency ($f_{3\,\mathrm{dB}}$) of the pick-up circuit from 219 kHz (unfiltered) to 11.3 kHz (cf. Fig. 6.17 (left)). At the same time, the resistor adds a thermal noise current spectral density of 31 $\mathrm{pA_{rms}}/\sqrt{\mathrm{Hz}}$, which is still below the measured floor of the spectral current noise of the unfiltered system at CRYRING of 40 $\mathrm{pA_{rms}}/\sqrt{\mathrm{Hz}}$. Before the installation, the final resistance of the prepared resistor was measured at 4.2 K inside a liquid helium bath at University Jena to be $R_{\mathrm{lp}} = 1.94\,\Omega$ [48].

The resulting noise current spectral density of the CCC after the installation of the low-pass filter is depicted in Fig. 6.18. At frequencies above 100 Hz the noise level clearly follows the trend predicted by the simulation with the cut-off frequency close to $f_{3\,\mathrm{dB}} = 11.3\,\mathrm{kHz}$. Apart from that, there is hardly any change to the overall noise floor compared to the situation without the filter installed (cf. Fig. 6.10). In general, the measurement of the absolute values of the spectral current noise in the buzzing accelerator environment was very volatile and two consecutive measurements already showed small changes of the overall noise level.

Subsequent measurements of a $^2\mathrm{D}^+$ beam confirmed that the duration of the instability during the acceleration was reduced. However, there was still a jump of the signal baseline during the injection of $^2\mathrm{D}^+$ bunches from the local ion source. In order to reduce the slew rates which couple to the SQUID during the

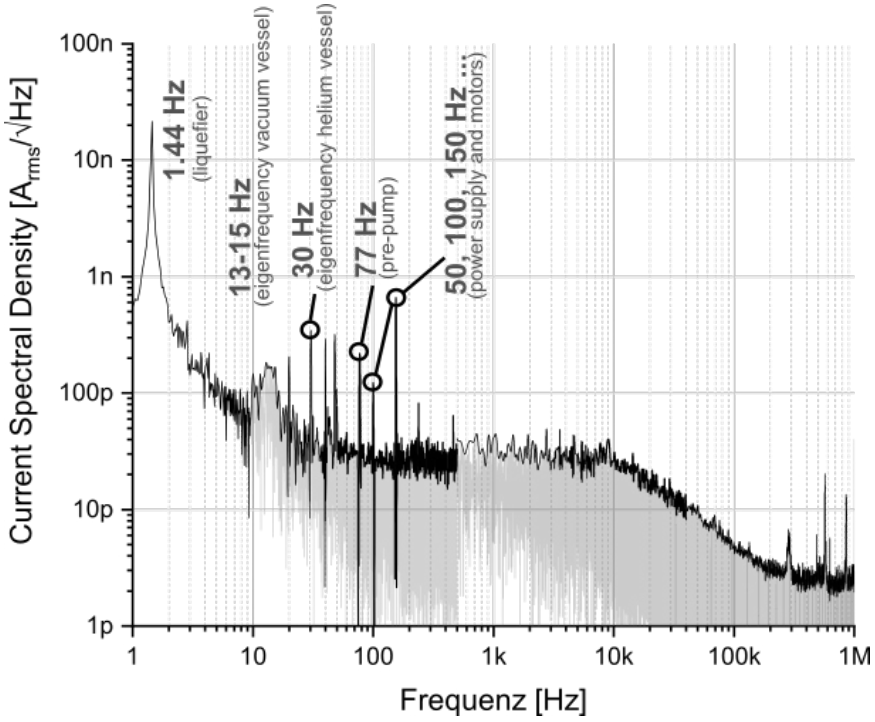

Figure 6.18: *Current spectral density of the CCC at CRYRING calculated from two different time series by a Fourier transformation. The resonance of the pick-up circuit around* 170 kHz *is hidden by the low-pass filter installed at the pick-up circuit with a cut-off frequency around* 10 kHz*.*

injection to values below the maximum threshold of the feedback loop, a lower cut-off frequency or a higher-order low-pass filter with a larger attenuation factor at higher frequencies are required.

6.5 Comparison with standard diagnostics

A comparison of the CCC measurement with the standard beam instrumentation is interesting in order to highlight the key advantages of the CCC and its best use cases. Moreover, the comparison provided an additional consistency check and proved how the CCC data can be used to calibrate beam diagnostics which otherwise require tedious calibration procedures or precarious assumptions of machine and beam properties.

6.5.1 Coasting beam (PCT and IPM)

Many experiments at CRYRING require coasting beams with a homogeneous interaction of the stored ions with their detectors to be most effective. In Figure 6.19, the measurement of the CCC, the PCT and the IPM of the beam intensity of an unbunched $^{208}Pb^{78+}$ beam after the injection from the ESR is shown. Following the injection, the lead ions were stored unbunched (coasting beam) with a constant magnetic dipole field for around 23 s.

Looking at the measurements, the data of all three detectors was consistent and described the exponential beam loss of the stored ion beam. At the injection the CCC loses its working point due to the large slew rate of the beam current. However, without bunching of the beam the duration of the instability is limited to a time window smaller than 100 ms. A new zero-current baseline for an absolute current measurement of the CCC was determined from the collected data after the beam dump. With a constant magnetic field and with the liquefier switched off, the two prominent sources of perturbations were eliminated and no digital signal filters were necessary. Moreover, a calibration pulse was applied to the CCC during the measurement and confirmed the linearity of the signal.

The signal from the PCT was affected by a significant amount of noise despite a stored beam current of around 10 µA, which is among the larger intensities at CRYRING. Moreover, the PCT is subject to a variable offset, which was corrected based on the zero-current baseline of the PCT before the beam injection. In this measurement, the standard deviation of the PCT signal around the mean beam current of the stored beam (5 s to 24 s) was determined to be $\Delta I_{\mathrm{noise}}^{(\mathrm{PCT})} = 1.9\,\mu A_{\mathrm{rms}}$ with a bandwidth of 100 Hz, which is about three orders of

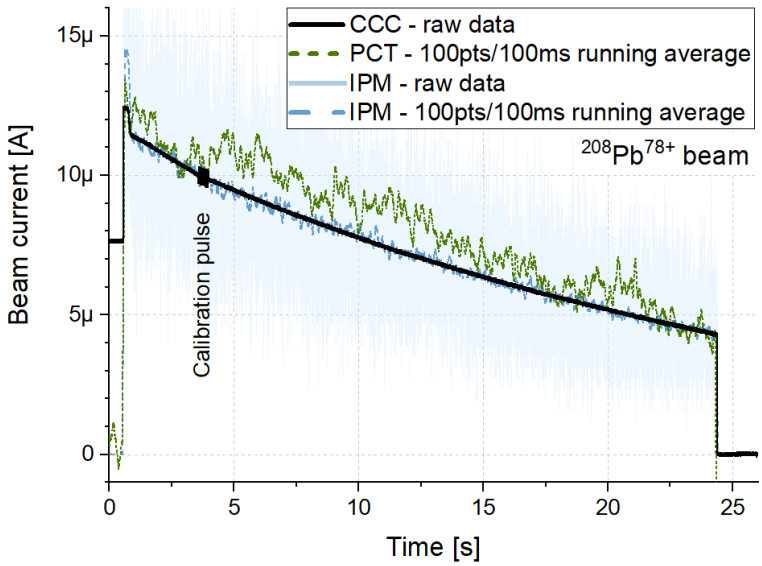

Figure 6.19: *A stored coasting beam of $^{208}Pb^{78+}$ measured by the CCC (unfiltered, black) with a low feedback sensitivity and the maximum gain-bandwidth-product ($R_f = 3\,\mathrm{k\Omega}$, $GBP = 7.2\,\mathrm{GHz}$), by the PCT (averaged, green) and by the horizontal IPM (blue). The CCC data was used to assign an absolute current scale to the IPM.*

magnitude larger than the one of the CCC data. An exponential fit of the CCC data on the same time span provided the mean reference beam current, which was used to calculate the standard deviation (rms) of the measurement.

For the IPM, there was no straightforward calibration factor available since it depends on a number of different parameters including the ion properties, the residual vacuum pressure and the integration time of the number of counts. Therefore, the CCC current data was used to convert the count rate $\dot{N}$ of the IPM to an absolute current signal. In order to obtain a linear calibration factor k, first, an exponential function ($I(t) = I_0\, e^{-t/\tau}$) was fitted to the slope of the CCC data to determine the amplitude I_0 and the time constant τ of the stored beam. On the same time interval, the count rates $\dot{N}^{(IPM)}(t)$ of the IPM were fitted with the same exponential function, but with a fixed time constant $\tau = \tau_{beam}$, as determined from the CCC data. The fraction of the calculated amplitudes I_0 provided the calibration factor k in order to convert the IPM count rate to a current

$$\mathrm{I^{(IPM)}}(t) = \dot{N}^{(IPM)}(t) \times k = \dot{N}^{(IPM)}(t) \times \frac{I_0^{(CCC)}}{I_0^{(IPM)}}\ . \tag{6.9}$$

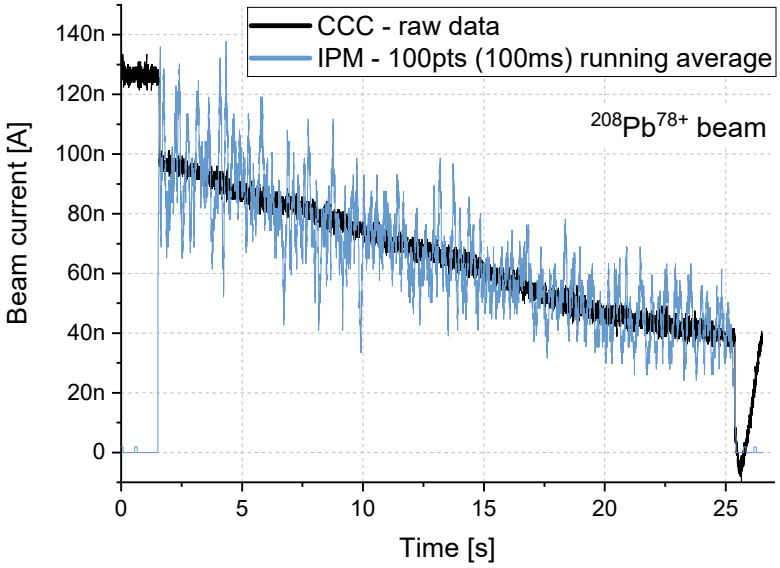

Figure 6.20: *Comparative measurement of a stored coasting* $^{208}Pb^{78+}$ *beam by the CCC (unfiltered, black), with* $R_f = 30\,\mathrm{k\Omega}$ *and* $GBP = 7.2\,\mathrm{GHz}$*, and by the horizontal IPM (averaged, blue). The liquefier was switched off.*

While this method may be improved, it led to an excellent correlation between the two data sets for beams with a constant energy and an exponential beam loss.

With conservative bias voltage settings for the MCP, the dark count rate of the IPM was negligible and any fluctuation of the beam signal was caused by the statistical interaction of the beam with the residual gas atoms. However, due to the operating principle of the IPM – with a strong dependence on the operating conditions and the ion species – it is impossible to assign a single universal measurement resolution. In principle, with enough integration time, the IPM can resolve individual ions stored in the ring. However, in this particular measurement configuration, the calculated standard deviation of the IPM data of the stored beam relative to the mean beam current (given by the exponential fit) was determined to be $\Delta I^{(\mathrm{IPM})}_{\mathrm{noise}} = 1.7\,\mu A_{\mathrm{rms}}$ with an acquisition bandwidth of 1 kHz.

To demonstrate the variable sensitivity of the IPM, Figure 6.20 shows a measurement of a $^{208}Pb^{78+}$ beam with a reduced maximum beam intensity below 100 nA. The small interaction cross section with the residual gas led to count rates of the IPM between 0 and 30 events/ms (within one integration window

of 1 ms). As a result, the standard deviation of the IPM relative to the mean beam current was 1.1 μA_{rms} compared to 2.6 nA_{rms} of the CCC.

In summary, the measurement campaign demonstrated that for typical beam conditions at CRYRING the current resolution of both the PCT and the IPM was strongly limited. The PCT was affected by a large noise level which led to a standard deviation of the measurement of 1.9 μA_{rms}. At low beam intensities, the effective current resolution of the IPM was limited by the small amount of secondary particles which were produced. At the same time, the CCC could provide a superior current resolution with the determined standard deviation of better than 3.2 nA_{rms}. In conclusion, it was shown that at mean beam intensities below 20 µA the CCC could provide a current resolution that was improved by three orders of magnitude compared to the competing standard methods for coasting beams discussed herein.

6.5.2 Bunched beam (ICT and BPMs)

There are two diagnostic systems which are commonly used to measure the beam intensity of bunched beams: the ICT and the processed sum signal of a BPM (CryRadio). Figure 6.21 shows a comparison of the measurements of the CCC and of the ICT for a $^2D^+$ beam injected from the local ion source. After the acceleration from an energy of 0.3 MeV/u to 5 MeV/u, the ions were stored as a bunched beam for close to 30 s.

At larger beam intensities, the current slew rate of the beam bunches during the first half of the acceleration exceeded the maximum slew rate of the CCC, which produced a distortion of the measured current signal. At the time of the measurement, there was no low-pass filter installed in the pick-up circuit of the CCC system to suppress this effect. Also the ICT system could not supply a meaningful measurement during the acceleration. It had been designed in a way such that it could only supply an accurate reading when the energy (and β) was constant (refer to bunch signal processor in Chapter 1). The offsets of the signals were corrected using the zero-current baseline after the dump.

Following the accelerator ramp both instruments detect the exponential beam loss of the stored ions. There is a small deviation between the two measurements which may be caused by an incorrect integration window for the bunch

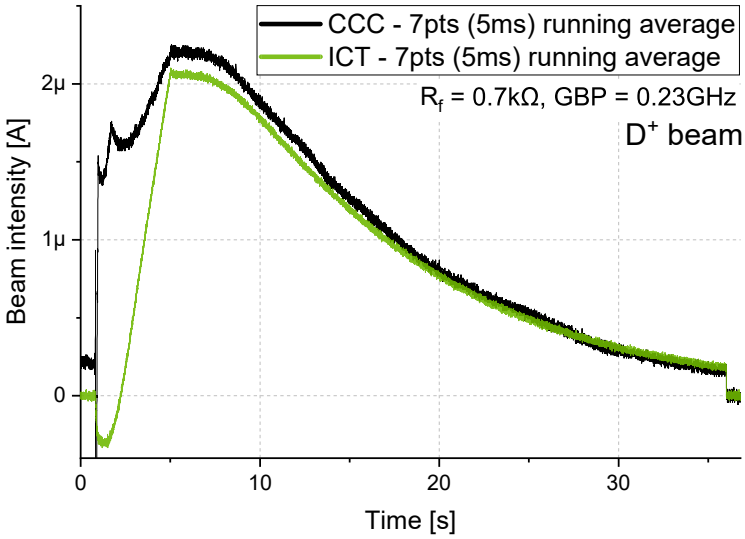

Figure 6.21: *Beam intensity of a stored bunched beam of* $^2D^+$ *measured by the CCC (black) and by the ICT (green). The calibration factor used for the ICT was* $10\,\mathrm{V} = 24\,\mathrm{MHz} = 10\,\mu\mathrm{A}$.

shape processor of the ICT. The typical current noise of the ICT, expressed as a standard deviation from the mean beam current, was measured to be in the order of $30\,\mathrm{nA_{rms}}$ with a bandwidth limited by the signal processing of 100 Hz. Therefore, the current resolution of the ICT at CRYRING was inferior to the one achieved by the CCC.

In contrast to the inductive signal of the ICT, capacitive signals (e.g. of the BPMs) generally require an external calibration to provide an absolute current signal. However, they had a lower noise associated to them. The sum-signal of the BPM was integrated with the same bunch processor which was used for the ICT to remove the signal baseline. Alternatively, the frequency component equivalent to the revolution frequency of the ions was extracted from the BPM signal using the super-heterodyne principle, which led to the low-noise CryRadio signal (refer to Ch. 1). Moreover, this approach allowed a current monitoring also during the acceleration. The signal output of both methods was then converted to a current with a linear calibration factor determined from the data of the CCC at the flat-top.

Figure 6.22 gives a comparison of the signal of the CCC and of the current measurements using the BPMs and CryRadio. The current noise of the BPM signal

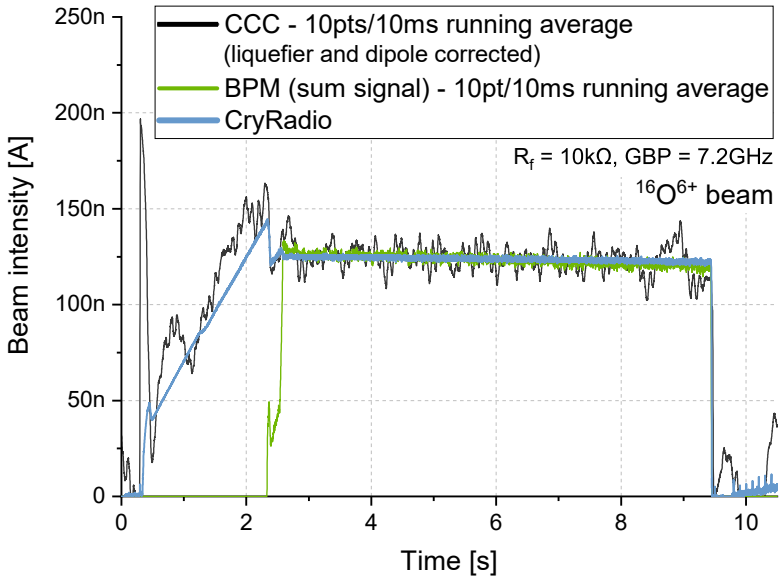

Figure 6.22: *Beam intensity of a stored beam of $^{16}O^{6+}$ at CRYRING measured by the CCC (black), the BPM (green) and by the CryRadio (blue). The output of the BPM and of the CryRadio were calibrated with the absolute current signal of the CCC.*

was much lower than of the CCC and values as low as 100 pA_{rms} were reported here [16]. The observed noise of CryRadio was even lower.

In conclusion, at CRYRING there exist excellent diagnostic tools to monitor the beam intensity of stored bunched beams with a current resolution which is similar or even better than what the CCC can provide at this moment. However, measurements by the BPM offer only an uncalibrated current signal and the CCC can potentially increase their measurement accuracy by providing a precise current calibration, taking into account the constantly changing ions species and beam parameters at CRYRING.

6.5.3 Schottky measurement

A competing method to obtain an uncalibrated current measurement at low intensities is the analysis of the frequency spectrum (so-called Schottky spectrum) of the bunched as well as unbunched stored beam. At CRYRING, the Schottky probe was used to track the beam intensity of only the bunched beam and then the signal from the Schottky offered no substantial advantage (in terms of current resolution) compared to the output of CryRadio. Figure 6.23 shows the

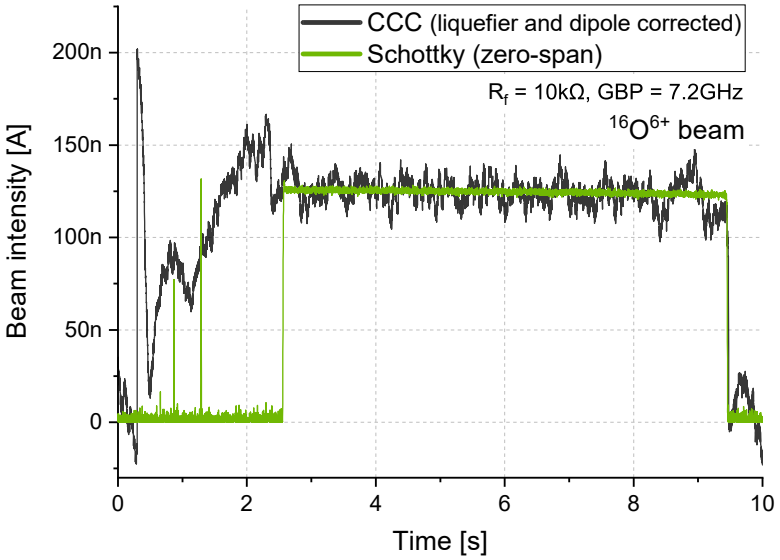

Figure 6.23: *A stored beam of $^{16}O^{6+}$ measured by the CCC (black) and by using the zero-span output of the Schottky (green). The output of the Schottky was calibrated with the absolute measurement of the CCC.*

Schottky signal of the same bunched $^{16}O^{6+}$ beam that was discussed previously. Once gain, the signal was calibrated using the signal data of the CCC throughout the flat-top.

However, the Schottky can provide a current measurement also for coasting, low-intensity beams. At the Antiproton Decelerator and at ELENA at CERN the Schottky signal is used routinely for bunched and coasting beam intensity monitoring of currents below 10 µA (see Sec. 1.2.3) [23, 24]. Even though they refined the Schottky analysis of the coasting beam throughout the years, a CCC monitor was installed in 2017 to improve the absolute accuracy of the current measurement.

6.6 Lifetime measurement

An important parameter for users of the CRYRING facility is the available integrated luminosity for a given ion species. Among many parameters specific to the detector setup, the integrated luminosity depends on the number of stored particles throughout the measurement time. In order to predict the expected number of ions throughout the accelerator cycle, the lifetime of the stored beam

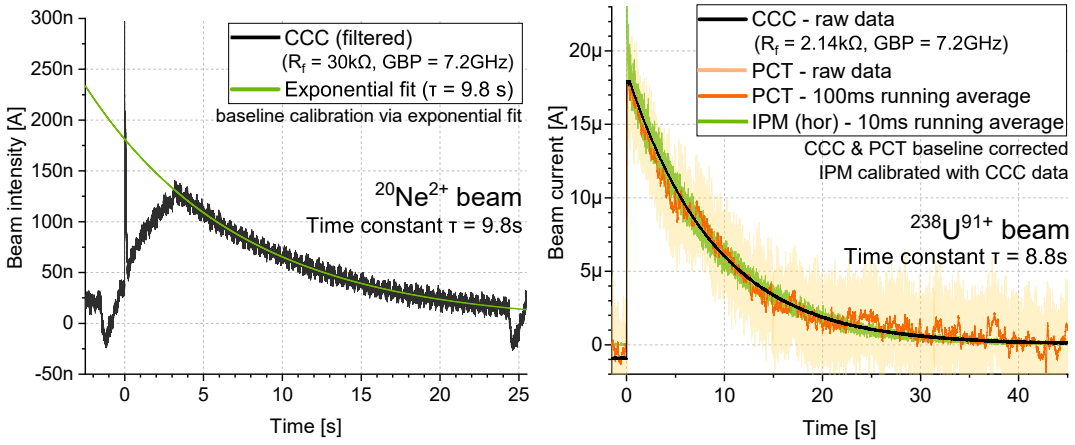

Figure 6.24: *Beam intensity of a stored bunched beam of $^{20}Ne^{2+}$ (left) from the local ion source and of $^{238}U^{91+}$ (right) injected from ESR. As a reference the signal from the PCT (orange) and from the IPM (green) are included on the right.*

can be calculated based on an estimate of the average vacuum pressure and the interaction cross sections with the rest gas. Alternatively, it can be measured for a given ion species for future reference using high-precision current data. In the following such a measurement is presented as an example for the possible applications of the CCC current monitor.

For the extraction of the lifetime an exponential beam loss according to $I(t) = I_0 \exp(-t/\tau)$ with a single time constant τ describing the beam loss was assumed. With a fit to the current measurement at the flat top, the time constant of the beam loss could be determined. Figure 6.24 shows the current data for an $^{20}\mathrm{Ne}^{2+}$ beam (left) and an $^{238}\mathrm{U}^{91+}$ beam (right). With the CCC, the storage time constants for these two beams were determined to be $\tau_{\mathrm{Ne}} = (9.81 \pm 0.03)\,\mathrm{s}$ and $\tau_{\mathrm{U}} = (8.770 \pm 0.001)\,\mathrm{s}$ respectively.

To sum up, with the CCC the beam commissioning process and the stored beam currents could be monitored and, towards the end of the beam-time, high resolution current data was made available to the operators and the experiments. The wide variations of beam parameters allowed a thorough testing of the setup in different operating conditions. In some cases, at injection the maximum slew rate of the SQUID FLL electronics was exceeded which highlighted an important limitation of the CCC setup which can be mitigated by tuning the coupling of the SQUID to the beam current. At other times with unbunched (coasting)

beam the CCC was the only measurement device that could provide a calibrated high-precision current measurement at intensities below 1 µA.

Summary and Outlook

The experimental program at the heavy-ion storage ring CRYRING@ESR at FAIR [13] is limited by the insufficient measurement capability to monitor the absolute beam intensity of weak coasting ion beams with intensities below 1 µA. The same is true for the experiments with exotic (e.g. radioactive) low-intensity beams at FAIR, where there is no stand-alone beam instrumentation which can provide a calibrated, non-interceptive current measurement. Existing instruments to monitor coasting beams in storage rings, like the Schottky monitor, need to be calibrated in dedicated machine beam-times using larger beam intensities and their current resolution with unbunched beam is strongly limited by stochastic noise [24].

The limitation can be overcome with the Cryogenic Current Comparator (CCC), which significantly extends the calibrated, non-destructive measurement range toward lower beam intensities. It is based on a DC Superconducting Quantum Interference Device (SQUID) for high-precision measurement of the magnetic field of the ion beam. The CCC consists of a complex superconducting shield against magnetic perturbations and the SQUID magnetometer which is connected to the superconducting pick-up coil via a flux transformer.

Preceding this work, at the Friedrich-Schiller-University Jena a CCC detector based on the established *radial* shield geometry [3] was adapted to the expected beam-line diameter and the beam conditions at FAIR [27]. However, the existing detector design has substantial weaknesses: First, the efficiency of the magnetic shield – with the large detector diameters of 200 mm which are required at FAIR – is rather low ($A_{radial} \leq 75\,\mathrm{dB}$) [43, 44]. This increases the impact of magnetic perturbations. Second, the small shielding factor makes it necessary to use a pick-up coil with a high-permeability core to guarantee a stable operation of the

CCC. The core has a significant impact on the overall current noise and thus limits the achievable current resolution [12]. Moreover, the strong inductive coupling of the SQUID to the beam current leads to large signal gradients (slew rates) at the detector, which can locally exceed the bandwidth of the SQUID readout [7]. Furthermore, the magnetostriction of the core was assumed to be responsible for the parasitic acoustic susceptibility (microphonic) of the CCC.

To mitigate these weaknesses, in this work a new coreless CCC detector was manufactured. The detector design is based on a novel *co-axial* shield geometry [10], which allows a significant increase of the available shielding factor. Due to the excellent shielding efficiency, it became feasible to remove the core and all associated noise contributions. The design was supported by extensive numerical simulations of the co-axial shield performed at TU Darmstadt, which confirmed the substantial improvement of the shielding factor ($A_{axial,\,est.} \approx 219\,\mathrm{dB}$) [11, 47]. Without the core, the coupling of the SQUID to the beam is rather small ($L_p \approx 50\,\mathrm{nH}$) and sets strong requirements towards the signal quality of the SQUID sensor. To achieve the maximum sensitivity, the Leibniz-Institute of Photonic Technology equipped the CCC with a high-precision 2-stage SQUID. In addition, the construction of the alternative shield geometry was done using pliable sheets of lead instead of rigid niobium. This allows for a quick and inexpensive manufacturing process.

The two competing detector systems were compared in detailed laboratory measurements. It was shown that an excellent shielding factor of

$$A_{axial} \geq 207\,\mathrm{dB}$$

could be achieved with the new co-axial design. Moreover, the beam current sensitivity or inverse mutual inductance $1/M_a$ – which is the current required to produce one magnetic flux quantum Φ_0 at the SQUID – was determined to be

$$\frac{1}{M_a^{(radial)}} \approx 100\,\mathrm{nA}/\Phi_0 \qquad \text{and} \qquad \frac{1}{M_a^{(axial)}} \approx 3.3\,\mu\mathrm{A}/\Phi_0\ .$$

The smaller amount of flux reaching the SQUID of the coreless CCC for a given beam current results in a larger slew rate limit. Even though the beam coupling was reduced substantially, a low noise level similar to the one of the core-based

CCC could be achieved. In particular at a frequency of 10 kHz, the measured white current noise density of both detectors was virtually identical at a level of slightly below $4\,\mathrm{pA_{rms}}/\sqrt{\mathrm{Hz}}$.

Despite all the potential advantages and promising laboratory results, it turned out that further investigations are necessary to lower the sensitivity of the axial design towards external perturbations, especially at low frequencies. The spikes of the current noise between 10 Hz to 100 Hz, created by mechanical and acoustic perturbations, were more pronounced in the coreless design, which points out a larger susceptibility against these external factors. In addition, the expected decrease of the current noise due to the removal of the core could not be observed. Instead, the large susceptibility to external perturbations increased the noise current spectral densities between 0.1 Hz and 100 Hz by a factor of 5 to 20.

Consequently, due to the better current resolution and due to the commitment to provide the best possible current measurement for the experiments at CRYRING@ESR, the well-established core-based CCC with radial shielding was selected to be tested with beam. The radial CCC was installed in a newly-designed cryogenic support system and – after a precise calibration – was operated with beam currents between 1 nA and 20 µA with various ion species (H, Ne, O, Pb, U) at the low-energy storage ring CRYRING@ESR.

The integration of the cryogenic system to the accelerator beam-line, the demands on the thermal and mechanical stability and the closed helium cycle made the design of the support system challenging. Together with the ILK gGmbH, a 70 l helium-bath beam-line cryostat with a gas-cooled thermal shield was realized. At GSI, the cryostat was combined with a commercial helium liquefier (Cryomech HeRL15) to extend the cryogenic operating time. However, the interaction between the liquefier and the cryostat created an excessive circulation of helium gas connected with an additional heat input, which limited its cryogenic operating time. In case the circulation was restricted, oscillations of the operating pressure were observed. Therefore, a nozzle was constructed to be mounted at the liquid helium transfer line from the liquefier to the helium container of the cryostat, to control the gas flow without introducing oscillations. At the moment, a thermal shield with a smaller gas flow resistance is investigated to stabilize the flow and to increase the cryogenic operating time.

In general, the SQUID is susceptible to external perturbations including mechanical vibrations, thermal and pressure fluctuations as well as electromagnetic interference [29]. In order to take advantage of its superior resolution, mechanical perturbations were reduced by mechanically decoupling the setup from the environment (diaphragm bellows, heavy sand-filled support). As part of the construction of the beam-line cryostat, finite-element simulations were carried out at TU Darmstadt [61] in order to determine its mechanical resonances. A stable operating temperature and pressure were supplied by the cryogenic support system. Electromagnetic perturbations were filtered by the metal walls of the cryostat. In this way, a noise current spectral density of

$$\sqrt{S_{\mathrm{CCC}}} = \frac{I_{\mathrm{rms}}}{\sqrt{\Delta f}} \approx 40\,\mathrm{pA_{rms}}/\sqrt{\mathrm{Hz}} \qquad \text{with} \qquad f \geq 50\,\mathrm{Hz}\ ,$$

was achieved at the beam-line. Taking into account the considerable amount of noise sources at CRYRING, the increase of the current noise – compared to the level at the test bench inside the rather noiseless, magnetically shielded room ($\sqrt{S_{\mathrm{CCC}}} = 4\,\mathrm{pA_{rms}}/\sqrt{\mathrm{Hz}}$) – could be kept to moderate values. The two most prominent noise contributions were identified and removed effectively: the ramped magnetic field of the neighboring dipole and the periodic signal from the commercial helium liquefier 1.44 Hz. A digital band-block filter and background subtraction were implemented so that in the majority of cases their contribution to the overall current noise was negligible.

Despite all efforts to reduce the influence of the operating environment, the performance of the SQUID (as given by the modulation depth) was reduced significantly once the CCC was mounted inside the beam-line cryostat. The transfer function ($|\partial V_{sq}/\partial \Phi_a|$) – which determines the slew rate limit and the noise performance of the SQUID – dropped by approximately 52 %, followed by another 35 % with the installation at CRYRING. It was impossible to identify a single perturbation source which was responsible for this deterioration. However, it is documented that radio-frequency electromagnetic interference produces identical effects [29, 70]. Nevertheless, after all noise mitigation efforts an excellent noise-limited current resolution of the CCC at CRYRING@ESR of

$$I_{\mathrm{rms}} \leq 3.2\,\mathrm{nA_{rms}}$$

at a bandwidth of 200 kHz was achieved. The typical drift of the zero-current baseline was below 30 pA/s. This corresponds to an increase of the current resolution by three orders of magnitude compared to the standard diagnostics tool for dc beam current measurements, the DC Current Transformer. Furthermore, the slew rate limit of the CCC is defined by the bandwidth of the flux-locked-loop (FLL) electronics and was determined to be

$$\dot{I}_{a,\max} \lesssim 400\,\mathrm{nA/\mu s}\ .$$

During the injection of larger current amplitudes from the local ion source or of cooled (strongly-bunched) ions from the Experimental Storage Ring (ESR), the slew rate of the signal exceeded the bandwidth of the FLL electronics and led to a current offset or to local artifacts in the measurement following the injection pulse. Subsequent, smaller changes of the beam current were tracked correctly. The absolute current calibration after such an incident could be restored successfully with an offset correction using the zero-current baseline after the beam was dumped. In order to increase the highest tolerable slew rate, a low-pass filter with a 3 dB-cutoff frequency of around 11.3 kHz was installed in parallel to the pick-up coil, which significantly reduced the slew rate of the signal at the SQUID. However, each resistor included in the filter introduces a Johnson-Nyquist thermal noise (in this case $31\,\mathrm{pA_{rms}}/\sqrt{\mathrm{Hz}}$ for $R = 2\,\Omega$) which decreases the current resolution of the CCC. To circumvent the additional current noise, the installation of two parallel SQUIDs which different measurement tasks (high sensitivity vs. large slew rate limit) is currently under investigation.

After commissioning, the CCC was compared to the intensity diagnostics at CRYRING (PCT, IPM, ICT, BPM, Schottky monitor) and, within this project, has proven to be a superior diagnostics tool for beam currents between 5 nA and 20 µA. There are still some open questions regarding the coupling of the microphonic current noise, the low-frequency noise of the coreless design and the operating time of the cryogenic system. Further investigations are in preparation as a follow up to this thesis. Overall, with this work a well-characterized CCC system is now available in order to enable high-precision intensity monitoring of unbunched beams at FAIR and to provide the basis for future high-quality research.

Zusammenfassung und Ausblick

Am ersten in Betrieb befindlichen Speicherring des FAIR Projekts, CRYRING@ESR [13], besteht im Rahmen des experimentellen Programms mit kontinuierlichen Ionenströmen geringer Intensität ein unmittelbarer Bedarf an der zerstörungsfreien Absolutmessung der Strahlintensität im Bereich unterhalb 1 µA. Existierende Instrumente (z.B. IPM oder Schottky Monitor) sind von Parametern des Strahls und des Restgases abhängig bzw. benötigen eine regelmäßige Kalibrierung im Zuge von dezidierten Strahlzeiten mit hohen Testströmen. Darüber hinaus ist bei Letzterem die Stromauflösung bei ungepulsten Strahlen stark durch stochastisches Rauschen begrenzt [24].

Mit dem kryogenen Stromkomparator (CCC) kann die Messgrenze für eine kalibrierte, zerstörungsfreie Messung der Strahlintensität deutlich nach unten erweitert werden. Dazu nutzt der CCC den aus der Metrologie bekannten supraleitenden Quanteninterferenzdetektor (SQUID), um das schwache Magnetfeld des Ionenstrahls mit höchster Präzision zu vermessen. Der CCC-Detektor besteht aus einem komplexen supraleitenden Schirm gegen magnetische Störeinflüsse sowie aus einem SQUID, der über einen Flusstransformator an die geschirmte, supraleitende Messspule gekoppelt ist.

Im Vorfeld dieser Arbeit wurde an der Friedrich-Schiller-Universität Jena ein CCC-Detektor – basierend auf dem etablierten *radialen* Schirmdesign [3] – an die Strahlrohrdurchmesser bei FAIR angepasst [27] und stand für die Anwendung am CRYRING@ESR zur Verfügung. Das etablierte Detektor-Design hat jedoch einige Schwächen: Zum einen ist der realisierbare Abschirmungsfaktor – mit den großen Detektordurchmessern von über 200 mm die bei FAIR benötigt werden – gering ($A_{radial} \leq 75\,\mathrm{dB}$) [43, 44]. Magnetische Störfelder haben dadurch einen bedeutenden Einfluss. Zum anderen ist es durch den niedrigen Schirmfaktor not-

wendig die Messspule mit einem magnetisch hochpermeablen Kernmaterial zu versehen, um einen stabilen CCC-Betrieb zu garantieren. Der verbaute hochpermeable Kern trägt jedoch deutlich zum Gesamtrauschen des CCCs bei und limitiert so die maximale Stromauflösung [12]. Darüber hinaus bringt der Kern noch weitere Nachteile mit sich: Die starke induktive Kopplung des SQUIDs an den Strahl führt zu hohen Anstiegsgeschwindigkeiten des Signals, die leicht die maximale Bandbreite der SQUID-Elektronik übersteigen können [7]. Zusätzlich wurde vermutet, dass die Magnetostriktion des Kerns zur störenden akustischen Empfindlichkeit (Mikrophonie) des Systems beiträgt.

Um diese Schwächen zu beseitigen, wurde im Zuge der vorliegenden Arbeit ein neuer kernloser CCC-Detektor für den Einsatz bei FAIR aufgebaut. Dieses CCC-Design basiert auf einer *axialen* Schildgeometrie [10] mit der ein bedeutend höherer Schirmfaktor erreicht werden konnte. Durch die exzellente Schirmung war es möglich den Kern und damit alle zugehörigen Störeinflüsse zu beseitigen. Die Konstruktion wurde durch ausführliche Simulationen des Abschirmfaktors an der TU Darmstadt unterstützt [11, 47], die eine bedeutende Verbesserung des magnetischen Abschirmfaktors bestätigten ($A_{axial,\,est.} \approx 219\,\mathrm{dB}$). Ohne den Kern ist die Kopplung des SQUIDs an den Strahl jedoch sehr gering ($L_p \approx 50\,\mathrm{nH}$) und stellt dadurch hohe Anforderungen an die Signalgüte des verwendeten SQUID Sensors. Um die höchstmögliche Messgenauigkeit zu erreichen, wurde der CCC deshalb durch das Leibniz-Institut für Phonotische Technologien mit einem hochpräzisen 2-stufigen SQUID [51] ausgerüstet. Auf mechanischer Seite ist das axiale Schirmdesign zudem aus einfach zu bearbeitenden Bleifolien anstatt aus massivem Niob gefertigt. Dadurch konnten die Produktionskosten reduziert und der Konstruktionsprozess stark beschleunigt werden.

Nach der Fertigstellung wurden beide Detektoren in Labormessungen verglichen. Dabei wurde der hervorragende Schirmfaktor des ko-axialen Designs von

$$A_{axial} \geq 207\,\mathrm{dB}$$

bestätigt. Zusätzlich wurde die Strahlstrom-Sensitivität $1/M_a$ beider Detektoren bestimmt

$$\frac{1}{M_a^{(radial)}} \approx 100\,\mathrm{nA}/\Phi_0 \qquad \text{und} \qquad \frac{1}{M_a^{(axial)}} \approx 3{,}2\,\mu\mathrm{A}/\Phi_0\ .$$

Diese Sensitivität beschreibt den nötigen Strahlstrom um einen Fluss in der Höhe eines magnetischen Flussquantums Φ_0 im jeweiligen SQUID zu erzeugen. Der kleinere Fluss des kernlosen CCC bei identischem Strahlstrom geht einher mit einer größeren Toleranz gegenüber hohen Anstiegsraten. Trotz der bedeutend kleineren induktiven Kopplung an den Strahl, konnte mit dem kernlosen CCC ein ähnlich niedriges Rauschniveau erreicht werden. Insbesondere bei Frequenzen rund um 10 kHz war das gemessene Rauschen in beiden CCCs auf nahezu demselben Niveau von etwas unter $4\,\mathrm{pA_{rms}}/\sqrt{\mathrm{Hz}}$. Ungeachtet des verbesserten magnetischen Schirmfaktors zeigte sich jedoch eine leicht erhöhte Sensitivität des kernlosen CCCs gegenüber externen Störeinflüssen, wie an den erhöhten Peaks des Stromrauschens zwischen 10 und 100 Hz deutlich erkennbar ist. Des weiteren konnte die erwartete Reduzierung des niederfrequenten Rauschens durch die Beseitigung des Kerns bisher nicht gezeigt werden. Die gemessene spektrale Rauschstrom-Dichte bei niedrigen Frequenzen zwischen 0,1 Hz und 100 Hz war stattdessen um einen Faktor von 5 bis 20 höher. Insgesamt zeigt der kernlose axiale CCC jedoch vielversprechende Eigenschaften. Es wurde aber ersichtlich, dass weitere Untersuchungen nötig sind, um den niederfrequenten Anteil des Stromrauschen zu reduzieren.

Aufgrund einer geringfügig besseren Stromauflösung, wurde schließlich der etablierte CCC mit radialem Schild und mit Ringkern für die Strahltests ausgewählt. Der radiale CCC wurde in einer neuentwickelten kryogenen Messplattform installiert, einer genauen Strom-Kalibrierung unterzogen und im Anschluss mit Strahlströmen zwischen 1 nA und 20 µA mit verschiedensten Ionensorten (H, Ne, O, Pb, U) am Speicherring CRYRING@ESR betrieben. Die nötige Integation der kryogenen Plattform in die Strahlführung des Beschleunigers, die Anforderungen an die thermische und mechanische Stabilität und der geschlossene Helium-Kreislauf machten die Auslegung der Messplatform zu einer großen Herausforderung. Gemeinsam mit dem Institut für Luft- und Kältetechnik gGmbH wurde ein 70 l Helium-Bad Kryostat mit integriertem Strahlrohr und einem gasgekühlten Hitzeschild aufgebaut. An der GSI wurde der Kryostat mit einem kommerziellen Helium-Verflüssiger (Cryomech HeRL15) kombiniert, um die kryogene Betriebszeit zu erhöhen. Im Zusammenspiel zwischen dem Verflüssiger und dem Kryostaten wurde eine übermäßige Gaszirkulation mit erhöhtem Wärmeeintrag beobachtet. Diese führte zu einer Reduktion der kryogenen Betriebszeit. Bei ei-

ner Drosselung der Zirkulation, kam es zu Druckoszillationen. Um den Gasfluss zu kontrollieren ohne dabei Oszillationen anzuregen, wurde ein Düsenaufsatz zur Montage zwischen Verflüssiger und Heliumbehälter des Kryostaten gefertigt und erste Versuche zeigten vielversprechende Ergebnisse.

Im Allgemeinen ist der SQUID anfällig gegenüber mechanischen, elektromagnetischen sowie thermischen Störeinflüssen [29]. Um die hohe Auflösung des SQUIDs auszunutzen, wurde der Aufbau am CRYRING mechanisch entkoppelt und Störfrequenzen wurden gedämpft. Die kryogene Messplattform garantierte eine konstante Temperatur des Heliumbades. Zudem schützte der Metallkäfig des Kryostaten den CCC gegen elektromagnetische Störungen. Damit wurde am CRYRING eine spektrale Rauschstromdichte von

$$\sqrt{S_{\mathrm{CCC}}} = \frac{I_{\mathrm{rms}}}{\sqrt{\Delta f}} \approx 40\,\mathrm{pA_{rms}}/\sqrt{\mathrm{Hz}} \quad \text{bei} \quad f \geq 50\,\mathrm{Hz}\ ,$$

gemessen. In Anbetracht der Rauschumgebung konnte die Steigerung des Rauschens im Vergleich zum Laborwert von $4\,\mathrm{pA_{rms}}/\sqrt{\mathrm{Hz}}$ gering gehalten werden. Der Einfluss des Magnetfelds des benachbarten Dipolmagneten sowie das periodische Störsignal des Helium-Verflüssigers bei 1,44 Hz wurden durch die Messplattform nicht gänzlich beseitigt. Daher wurden im Rahmen dieser Arbeit ein digitaler Bandblock-Filter und eine Hintergrundkorrektur eingeführt, sodass diese Störeinflusse nicht mehr signifikant zum Gesamtrauschen beitrugen.

Trotz allen Bemühungen die Schirmung gegenüber Störeinflüssen zu erhöhen, musste nach dem Einbau des CCCs in den Strahlführungs-Kryostaten ein Einbruch der Amplitude der Spannungsmodulation des SQUIDs festgestellt werden. In Folge wurde die Transferfunktion des SQUIDs ($|\partial V_{sq}/\partial \Phi_a|$) – die die maximale Anstiegsrate und das Rauschniveau des SQUIDs beeinflusst – um rund 52 % reduziert. Mit der Installation am CRYRING sank diese um weitere 35 %. Die genaue Ursache für diese Verschlechterung blieb unklar. In der Regel sind hochfrequente elektromagnetische Interferenzen dafür verantwortlich [29, 70]. Nichtsdestotrotz, konnte am CRYRING mit allen Abschirmmaßnahmen eine exzellente rauschlimitierte Stromauflösung des CCCs von

$$I_{\mathrm{rms}} \leq 3{,}2\,\mathrm{nA_{rms}}\ , \tag{6.10}$$

bei einer Signalbandbreite von 200 kHz gemessen werden. Der typische Drift der Nullstrom-Referenz war dabei kleiner als 30 pA/s. Das entspricht einer Verbesserung der Stromauflösung um drei Größenordnungen gegenüber dem DC Strahltransformator. Die maximale Änderungsrate des Strahlstroms die vom CCC korrekt gemessen wird, ist bestimmt durch die Bandbreite der Flussregelschleife des SQUIDs und lag bei

$$\dot{I}_{a,\max} \lesssim 400\,\mathrm{nA/\mu s}\ . \tag{6.11}$$

Während der Injektion von hohen Strömen aus der lokalen Ionenquelle am CRYRING und von gekühlten (stark komprimierten) Ionenbunchen vom Experimentier Speicherring (ESR) wurde die maximale Anstiegsrate (slew rate) der Elektronik überschritten, was zu Sprüngen oder zu lokalen Artefakten der Strommessung führte. Nachfolgende, typischerweise kleinere Änderungen des Strahlstroms wurden hingegen wieder richtig erfasst. Ein Sprung in der Strommessung konnte durch eine Kalibrierung anhand der Nullstromlinie nach der Zerstörung des Strahls korrigiert werden. Um die Schwelle für die größte messbare Anstiegsrate zu erhöhen, wurde parallel zur Messschleife ein Tiefpass-Filter mit einer 3 dB-Grenzfrequenz von rund 11,3 kHz installiert. Jeder zusätzliche ohmsche Widerstand eines solchen Filters erhöht jedoch mit seinem thermischen Rauschen (Johnson-Nyquist) das Gesamtrauschen des Systems (hier um $31\,\mathrm{pA_{rms}}/\sqrt{\mathrm{Hz}}$ mit $R = 2\,\Omega$). Um diese Beschränkung zu umgehen, ist ein CCC mit zwei parallelen SQUIDs mit je unterschiedlichen Messaufgaben (höchste Sensitivität und größte tolerable Anstiegsrate) geplant.

Nach der Inbetriebnahme wurde der CCC mit den im CRYRING@ESR vorhandenen Detektoren zur Intensitätsdiagnose (PCT, IPM, ICT, BPM, Schottky Monitor) verglichen. Anhand dieses Vergleichs konnte gezeigt werden, dass der CCC ein überlegenes Diagnoseinstrument für Strahlströme zwischen 5 nA und 20 µA ist. Es bleiben noch einige offene Fragen in Bezug auf die Kopplung des akustisch induzierten Stromrauschen, zum hohen niederfrequenten Rauschen des kernlosen CCCs und zu der autarken Standzeit der kryogenen Messplattform, die in nachfolgenden Arbeiten weiter untersucht werden müssen. Als Ergebnis dieser Arbeit steht nun jedoch ein vollständig charakterisierter CCC Intensitätsmonitor für die hochpräzise Stromüberwachung ungepulster Strahlen zur Verfügung, der die Basis weiterer Entwicklungen bei FAIR bildet.

Appendix

Cryogenic support system

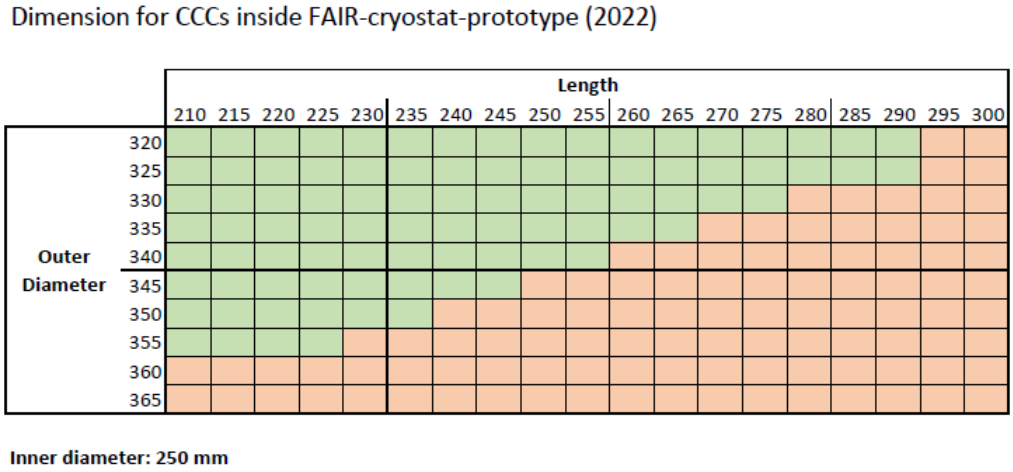

Figure A.1: *Available geometric dimensions for the installation of a CCC inside the FAIR CCC beam-line cryostat.*

Magnicon SQUID

The setup routine for the dc SQUID at cryogenic temperatures is the following: For more detailed instructions refer to the manual of the Magnicon XXF-1 electronics. An overview of the SQUID control software is given in Figure A.2.

1. The SQUID electronics is operated in direct-amplification mode (AMP mode) so that the voltage at the SQUID V_{sq} can be observed directly. The gain of the pre-amplifier of the Magnicon electronics is typically set to 2000. The output of the SQUID electronics V_{AMP} (Ch1) is connected to the oscilloscope (termination of 1 MΩ).

2. In order to obtain the flux-to-voltage modulation of the SQUID, the magnetic flux at the SQUID has to be changed. Vary the magnetic flux through the SQUID by several magnetic flux quanta by sending a drive current I_{Φ} either through the internal feedback coil of the SQUID or through the external calibration wire. Typically the internal generator of the Magnicon electronics is used to apply a triangular flux variation Phi_b with a frequency of 22 Hz. The electronics provides a reference signal with a peak-to-peak voltage of 1 V_{pp} with the same shape and phase of the applied flux. Connect the reference signal of the applied flux to the oscilloscope.

3. Display the two inputs to the oscilloscope in xy-mode with the input flux Phi_b on the x-axis and the output of the SQUID V_{AMP} on the y-axis. You should see a flat line – no change of the SQUID voltage with respect to the applied flux – at the oscilloscope. Now slowly increase the bias current I_b of the SQUID until the sinusoidal voltage modulation appears. Select I_b such that the slope of the modulation is at a maximum.

4. You can use the bias voltage V_b to correct for the resistance of the instrumentation wires and of the sensor and thus move the voltage modulation to the zero-voltage line to have them intersect where the transfer function $|\partial V_{sq}/\partial \Phi_b|$ is the largest. With the peak-to-peak value of the applied flux Phi_b and the voltage of the SQUID V_{sq} the transfer function and the mutual inductance M_f can be calculated from the voltage modulation.

5. Now the SQUID is ready to switch to the Flux-Locked-Loop (FLL) mode. Sometimes it is beneficial to lock on the declining slope which can be adjusted in the panel for the measurement settings.

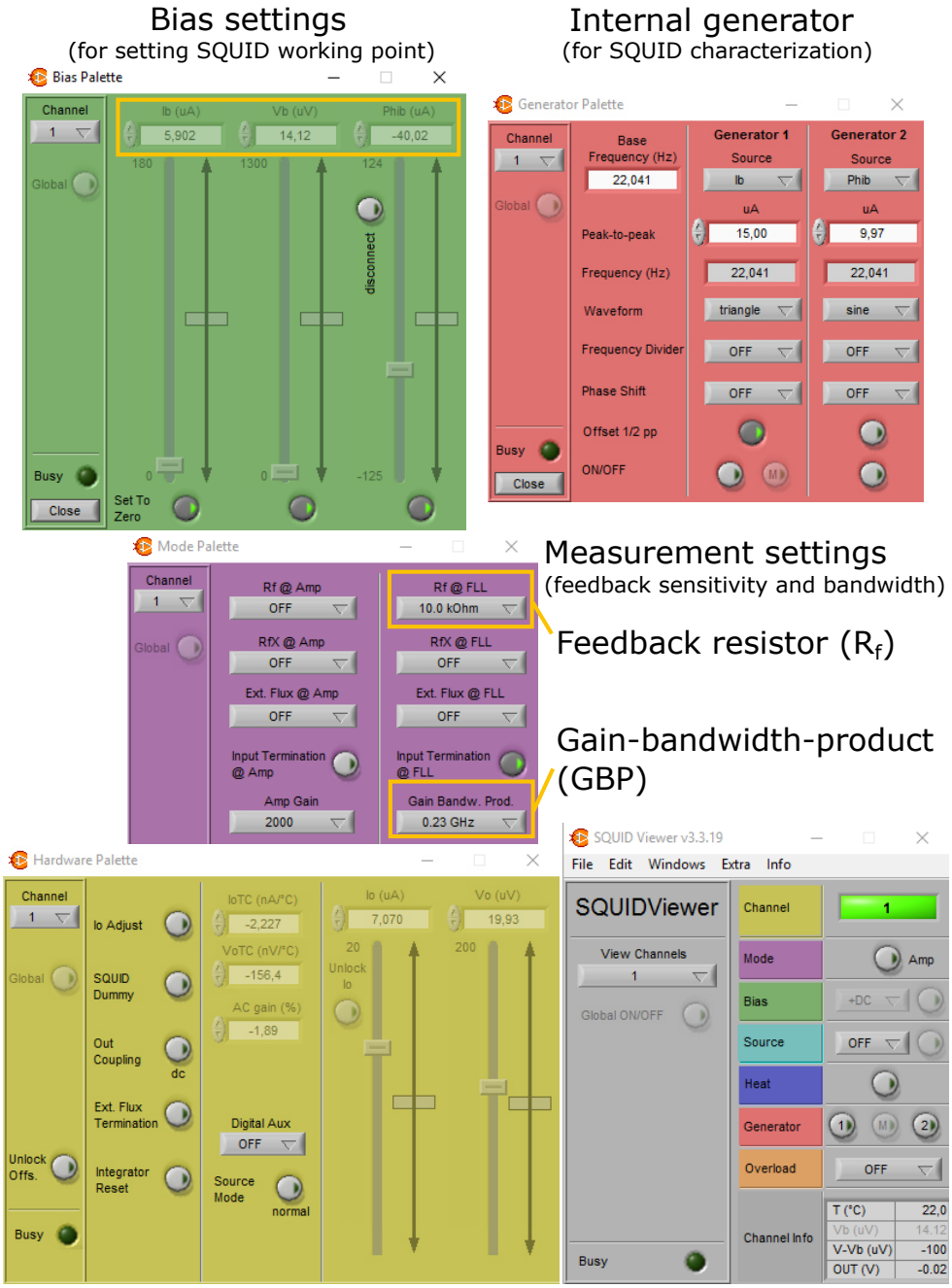

Figure A.2: *Overview of the control software (SQUID Viewer) by the Magnicon GmbH for the 1-stage dc SQUID that is installed in the CRY–rCCC.*

Data Sheet
1-stage Current Sensor C5XL1W

Sensor ID: C509_C41

date measured		2012.01.25
nominal input inductance Lin (nH)		1000
input coupling 1/Min (µA/Phi0)		0,29
feedback sensitivity 1/Mf (µA/Phi0)		40,5
maximum voltage swing ΔVmax (µV)		40,1
voltage swing @ working point ΔVw (µV)		32,81
transfer coefficient Vphi (µV/Phi0)		489,2
heater current in liquid Helium via ±V (mA)		70
heating time in liquid Helium via ±V (s)		0,1
bias current Ib (µA)		10
bias voltage Vb (µV)		16
setup file name		C509_C41.stp
flux noise (µPho/√Hz)	@ 50kHz	1,03166
	@ 10kHz	1,04294
	@ 1kHz	1,06576
	@ 100Hz	1,21884
	@ 10Hz	1,37335
	@ 1Hz	2,04892
	@ 0.1Hz	3,67301

All values obtained with XXF-1 SQUID electronics @ 4,2K.

Figure A.3: *Datasheet of the Magnicon 1-stage dc SQUID (model C5XL1W) that is installed in the CRY–rCCC.*

R_f[kΩ]	GBP[GHz]																		
	0.23	**0.27**	**0.3**	**0.38**	**0.47**	**0.55**	**0.66**	**0.82**	**1.04**	**1.28**	**1.5**	**1.8**	**2.25**	**2.8**	**3.3**	**4**	**5**	**6.2**	**7.2**
0.7	75	88	97	123	153	179	214	266	338	416*	487*	584*	731*	909*	1071*	1299*	1623*	2013*	2338*
0.75	70	82	91	115	142	167	200	248	315	388	455*	545*	682*	848*	1000*	1212*	1515*	1879*	2182*
0.91	57	67	75	95	117	137	165	205	260	320	375	450*	562*	699*	824*	999*	1249*	1548*	1798*
1	52	61	68	86	107	125	150	186	236	291	341	409*	511*	636*	750*	909*	1136*	1409*	1636*
2.14	24	29	32	40	50	58	70	87	110	136	159	191	239	297	350	425*	531*	658*	765*
2.31	23	27	30	37	46	54	65	81	102	126	148	177	221	275	325	394	492*	610*	708*
3	17	20	23	29	36	42	50	62	79	97	114	136	170	212	250	303	379	470*	545*
7	7	9	10	12	15	18	21	27	34	42	49	58	73	91	107	130	162	201	234
7.5	7	8	9	12	14	17	20	25	32	39	45	55	68	85	100	121	152	188	218
9.1	6	7	7	9	12	14	16	20	26	32	37	45	56	70	82	100	125	155	180
10	5	6	7	9	11	13	15	19	24	29	34	41	51	64	75	91	114	141	164
23.1	2	3	3	4	5	5	6	8	10	13	15	18	22	28	32	39	49	61	71
30	2	2	2	3	4	4	5	6	8	10	11	14	17	21	25	30	38	47	55
100	1	1	1	1	1	1	2	2	2	3	3	4	5	6	8	9	11	14	16

*The maximum slew rate without introducing additional current noise was limited to 400 nA/µs due to the loop delay of the FLL electronics.

Table A.1: *Estimated maximum slew rate $\dot{I}_a$ of the applied (beam) current in units of* $\mathrm{nA}/\mu\mathrm{s}$ *as a function of the feedback resistor R_f and the gain-bandwidth-product GBP which could be tracked by the CRY–rCCC at CRYRING. For the calculation the transfer factor of $V_\Phi = 100\,\mu\mathrm{V}/\Phi_0$ and a beam current sensitivity of $1/M_a = 100\,\mathrm{nA}/\Phi_0$ were used.*

List of Figures

1 GSI and FAIR accelerator complex 2

1.1 AC Current Transformer (schematic) 10
1.2 Beam Position Monitor at CRYRING (photo) 11
1.3 CryRadio – readout (schematic) 12
1.4 Faraday Cup (schematic) 13
1.5 DC Current Transformer (schematic) 15
1.6 Ionization Profile Monitor (schematic and photo) 18

2.1 Tilted-washboard potential U_J 27
2.2 DC SQUID (schematic) 29
2.3 SQUID modulation $V - \Phi$ 31
2.4 FLL electronics (schematic) 32
2.5 SQUID bandwidth limit 34
2.6 SQUID $V - \Phi$ modulation 35
2.7 CHARM – spectrum of irradiation 39

3.1 Cryogenic Current Comparator - principle 42
3.2 Cryogenic Current Comparator – radial geometry (schematic) . 43
3.3 Cryogenic Current Comparator - SQUID cartridge 44
3.4 Coupling transformer (basic) 45
3.5 Coupling transformer (with core) 47
3.6 Topology of superconducting shield 48
3.7 Inductance and flux noise of magnetic core 51

4.1 Radial shield topology – simulation of shielding factor 56
4.2 Axial shield topology – simulation of shielding factor 57

4.3 Test bench at University Jena 59
4.4 Radial design – CRY–rCCC (photo and schematic) 61
4.5 CRY–rCCC – construction (photo) 62
4.6 CRY–rCCC – transfer function 63
4.7 CRY–rCCC – modulation V_{sq} – Φ (internal generator, lab) . . . 65
4.8 CRY–rCCC – modulation V – Φ (calibration current) 67
4.9 CRY–rCCC – noise spectrum (lab) 69
4.10 Coreless axial design – CRY–aCCC (photo and schematic) . . . 71
4.11 CRY–aCCC – construction, soldering interface (photos) 72
4.12 CRY–aCCC – construction, pick-up (photos) 73
4.13 CRY–aCCC – transfer function & noise 76
4.14 CRY–aCCC – modulation V_{sq} – Φ 77
4.15 CRY–aCCC – noise spectrum (lab) 81
4.16 Comparison – spectral current noise density 84

5.1 Beam-line cryostat – 3D model 91
5.2 Helium chamber & thermal shield (photo) 92
5.3 Beam-line cryostat – installation (schematic and photo) 93
5.4 Beam-line cryostat – mechanical resonances 94
5.5 Beam tubes with insulator gap (photos) 96
5.6 Polyimide insulator of helium tube (schematic and photo) . . . 97
5.7 Closed helium cycle (schematic) 102
5.8 Temperature distribution and helium level 104
5.9 Helium pressure oscillation 105
5.10 Perturbations by helium liquefier 106

6.1 Beam diagnostics at CRYRING@ESR (schematic) 111
6.2 CCC readout – overview (schematic) 112
6.3 CCC readout – DAQ (schematic) 113
6.4 Calibration current – transfer factor 115
6.5 CRY–rCCC – calibration 116
6.6 CCC baseline drift & RMS noise – CRYRING 118
6.7 CCC at CRYRING@ESR (photo) 119
6.8 SQUID Φ–V modulation – CRYRING 120
6.9 CCC signal perturbation – dipole 121

6.10 Current noise density of full-bandwidth CCC at CRYRING . . . 123
6.11 Low current test signals – CRYRING 124
6.12 $^{2}D^{+}$ beam – 80 nA stored beam 127
6.13 $^{20}Ne^{3+}$ beam – first turns and stored beam 128
6.14 $^{2}D^{+}$ beam – 12 nA stored beam 130
6.15 $^{2}D^{+}$ beam – slew rate limit 131
6.16 Pick-up circuit with flux transformer and LP filter 133
6.17 Slew rate increase – low pass filter design 134
6.18 Current noise density of reduced-bandwidth CCC at CRYRING 135
6.19 $^{208}Pb^{78+}$ beam – diagnostics comparison (PCT) 137
6.20 $^{208}Pb^{78+}$ beam – diagnostics comparison (IPM) 138
6.21 $^{2}D^{+}$ beam – diagnostics comparison (ICT) 140
6.22 $^{16}O^{6+}$ beam – diagnostics comparison (CryRadio) 141
6.23 $^{16}O^{6+}$ beam – diagnostics comparison (Schottky) 142
6.24 $^{20}Ne^{2+}$ & $^{238}U^{91+}$ beam – stored beam lifetime 143
A.1 Beam-line cryostat – detector volume 157
A.2 SQUID control software CRY–rCCC 159
A.3 SQUID datasheet CRY–rCCC 160

List of Tables

1.1 Specifications of beam instrumentation at CRYRING@ESR . . . 20

2.1 SQUID irradiation dose at CHARM 38

3.1 Effects of high-permeability core on CCC performance 52

4.1 Specifications of CCC systems for CRYRING 86

5.1 Cryostat design requirements 89
5.2 Emissivity values for estimation of heat radiation 99
5.3 Estimated heat load of the beam-line cryostat 100

6.1 Properties of CRYRING@ESR 110
6.2 Calibration factors and measurement range of CRY–rCCC . . . 116
6.3 Ion species measured at CRYRING 126
A.1 Maximum slew rate for CRY–rCCC 161

Bibliography

[1] I.K. Harvey. A Precise Low Temperature dc Ratio Transformer. *Rev. Sci. Instrum.*, 43(11):1626–1629, November 1972. doi:10.1063/1.1685508.

[2] J. Clarke and A. Braginski, editors. *The SQUID Handbook: Fundamentals and Technology of SQUIDs and SQUID Systems, II.* Wiley-VCH Verlag, 2006. ISBN 9783527404087.

[3] K. Grohmann, D. Hechtfischer, and J. Jakschik. A cryodevice for induction monitoring of dc electron or ion beams with nano-ampere resolution. In *SQUID - Superconducting Quantum Interference Devices and their Applications*, pages 311–316. De Gruyter, December 1977. doi:10.1515/9783110887495-027.

[4] M. Kuchnir, J. McCarthy, and P. Rapidis. SQUID based beam current meter. *IEEE Trans. Magn.*, 21(2):997–999, March 1985. doi:10.1109/tmag.1985.1063601.

[5] A. Peters, W. Vodel, et al. A cryogenic current comparator for the absolute measurement of nA beams. In *AIP Conference Proceedings*, volume 451, 1998. doi:10.1063/1.56997.

[6] T. Tanabe, K. Chida, and K. Shinada. A cryogenic current-measuring device with nano-ampere resolution at the storage ring TARN II. *Nucl. Instr. Methods in Phys. Res. A*, 427(3):455–464, May 1999. doi:10.1016/S0168-9002(99)00058-3.

[7] M. Fernandes, R. Geithner, et al. Non-perturbative measurement of low-intensity charged particle beams. *Supercond. Sci. Technol.*, 30(1):015001, January 2016. doi:10.1088/0953-2048/30/1/015001.

[8] M. Fernandes. *SQUID based Cryogenic Current Comparator for Measuring Low-intensity Antiproton Beams*. Phd thesis, University of Liverpool, Liverpool, UK, June 2017.

[9] H.H. Gutbrod. International Facility for Antiproton and Ion Research (FAIR) at GSI, Darmstadt. *Nuclear Physics A*, 752:457–469, April 2005. doi:10.1016/j.nuclphysa.2005.02.137.

[10] V. Zakosarenko, M. Schmelz, et al. Coreless SQUID-based cryogenic current comparator for non-destructive intensity diagnostics of charged particle beams. *Supercond. Sci. Technol.*, 32(1):014002, January 2019. doi:10.1088/1361-6668/aaf206.

[11] N. Marsic, W.F.O. Müller, et al. Numerical analysis of a folded superconducting coaxial shield for cryogenic current comparators. *Nucl. Instrum. Methods Phys. Res. A*, 922:134–142, April 2019. doi:10.1016/j.nima.2018.12.063.

[12] R. Geithner, D. Heinert, et al. Low temperature permeability and current noise of ferromagnetic pickup coils. *Cryogenics*, 54:16–19, February 2013. doi:10.1016/j.cryogenics.2012.10.002.

[13] W. Geithner, Z. Andelkovic, et al. Status and outlook of the CRYRING@ESR project. *Hyperfine Interactions*, 238(1), January 2017. doi:10.1007/s10751-016-1383-5.

[14] F. Kurian. *Cryogenic Current Comparators for Precise Ion Beam Current Measurements*. Phd thesis, Goethe University, Frankfurt am Main, Germany, 2015.

[15] A. Reiter et al. Beam Instrumentation for CRYRING@ESR. In *Proc. 9th Int. Part. Acc. Conf. (IPAC2018), Vancouver, Canada*, June . doi:10.18429/JACoW-IPAC2018-WEPAK004.

[16] A. Paal, A. Simonsson, et al. Bunched beam current measurements with 100 pA rms resolution at CRYRING. In *Proc. 10th Europ. Part. Acc. Conf. (EPAC'06), Edinburgh, UK*, pages 1196–1198, .

[17] A. Paal and A. Simonsson. Bunched beam current measurements with 1 nA rms resolution at CRYRING using a BERGOZ Integrating Current Transformer (ICT). Technical report, Stockholm University, 2006.

[18] A. Reiter. Beam Instrumentation for CRYRING@ESR. Technical Report LOBI-CRYRING-2013-01, GSI, 2021.

[19] P. Forck. Lecture Notes on Beam Instrumentation and Diagnostics. Joint University Accelerator School, January 2011. Gesellschaft für Schwerionenforschung (GSI), Darmstadt, Germany.

[20] D. Spasojević, S. Bukvić, et al. Barkhausen noise: Elementary signals, power laws, and scaling relations. *Physical Review E*, 54(3):2531–2546, September 1996. doi:10.1103/physreve.54.2531.

[21] T. Hoffmann, H. Bräunig, and R. Haseitl. LASSIE: The Large Analogue Signal and Scaling Information Environment for FAIR. In *Proc. Int. Conf. on Acc. and Large Exp. Phys. Contr. Syst. (ICALEPCS'11), Grenoble, France*, pages 250–252, 2011.

[22] A. Paal, J. Dietrich, et al. Methods and instrumentation for measurement of low ion beam currents at cryring. In *Proc. 9th Europ. Part. Acc. Conf. (EPAC 2004), Lucerne, Switzerland*, pages 2748–2749, .

[23] M.E. Angoletta, V. Chohan, et al. The New Digital-Receiver-Based System for Antiproton Beam Diagnostics. In *Proc. 19th Part. Acc. Conf. (PAC'01), Chicago, USA*, pages 2371–2373, 2001.

[24] M.E. Angoletta, C. Carli, et al. Schottky based intensity measurements and errors due to statistical fluctuations. In *Proc. 8th Int. Part. Acc. Conf. (IPAC'17), Copenhagen, Denmark*, pages 385–388, . doi:10.18429/JACOW-IPAC2017-MOPAB112.

[25] Femto Messtechnik GmbH. *Datasheet of DHPCA-100 from Femto (DE-DHPCA-100_R13/LK,JMi/10OKT2019).* Berlin, Germany.

[26] M.E. Angoletta, M. Jaussi, and J. Molendijk. The new digital low-level rf system for CERN's Extra Low ENergy Antiproton machine. In *Proc. 10th*

Int. Part. Acc. Conf. (IPAC'19), Melbourne, Australia, pages 3962–3965, . doi:10.18429/JACOW-IPAC2019-THPRB069.

[27] V. Tympel, F. Kurian, et al. Cryogenic Current Comparators for 150 mm beamline diameter. In *Proc. 6th Int. Beam Instr. Conf. (IBIC'17), Grand Rapids, USA*. doi:10.18429/JACOW-IBIC2017-WEPCF07.

[28] F. London and H. London. The electromagnetic equations of the supraconductor. *Proc. R. Soc. A*, 149(866):71–88, March 1935. doi:10.1098/rspa.1935.0048.

[29] J. Clarke and A. Braginski, editors. *The SQUID Handbook: Fundamentals and Technology of SQUIDs and SQUID Systems, I.* Wiley-VCH Verlag, 2004. ISBN 9783527402298. doi:10.1002/3527603646.

[30] L.D. Landau and V.L. Ginzburg. On the theory of superconductivity. *Zh. Eksp. Teor. Fiz.*, 20(1064):546–568, 1950.

[31] J. Bardeen, L.N. Cooper, and J.R. Schrieffer. Theory of superconductivity. *Phys. Rev.*, 108(5):1175–1204, 1957. doi:10.1103/PhysRev.108.1175.

[32] D. Drung et al. *SQUID Sensors: Fundamentals, Fabrication and Applications*, volume 329 of *NATO Science Series E*. Springer Netherlands, 1996. ISBN 9789401063937.

[33] D. Drung, C. Assmann, et al. Highly sensitive and easy-to-use SQUID sensors. *IEEE Trans. Appl. Supercond.*, 17(2):699–704, June 2007. doi:10.1109/tasc.2007.897403.

[34] F.C. Wellstood, C. Urbina, and J. Clarke. Low-frequency noise in dc superconducting quantum interference devices below 1 K. *Appl. Phys. Lett.*, 50(12):772–774, 1987. doi:10.1063/1.98041.

[35] D. Drung. High-t_c and low-t_c dc SQUID electronics. *Supercond. Sci. and Technol.*, 16(12):1320–1336, October 2003. doi:10.1088/0953-2048/16/12/002.

[36] J. Mekki, M. Brugger, et al. CHARM: A mixed field facility at CERN for radiation tests in ground, atmospheric, space and accelerator representative environments. *IEEE Trans. Nucl. Sci.*, 63(4):2106–2114, August 2016. doi:10.1109/tns.2016.2528289.

[37] C. Cangialosi and S. Danzeca. Charm User Dosimetry Document for SQUID test. Technical report, CERN High Energy Accelerator Mixed-field (CHARM), 2018.

[38] L. Frunzio, R. Cristiano, and S. Pagano. Radiation hardness of josephson devices. *Jpn. J. of Appl. Phys.*, 37(2):40–45, January 1998. doi:10.7567/jjaps.37s2.40.

[39] C. Omet. Fluka calculations of radiation levels at FAIR (internal notes). 2018.

[40] K. Grohmann, H.D. Hahlbohm, et al. Field attenuation as the underlying principle of cryo-current comparators 2. ring cavity elements. *Cryogenics*, 16(10):601–605, October 1976. doi:10.1016/0011-2275(76)90192-2.

[41] R. Geithner. *Optimierung eines kryogenen Stromkomparators für den Einsatz als Strahlmonitor*. PhD thesis, Friedrich-Schiller-University Jena, 2013.

[42] K. Grohmann, H.D. Hahlbohm, et al. Field attenuation as the underlying principle of cryo current comparators. *Cryogenics*, 16(7):423–429, July 1976. doi:10.1016/0011-2275(76)90056-4.

[43] H. De Gersem, N. Marsic, et al. Finite-element simulation of the performance of a superconducting meander structure shielding for a cryogenic current comparator. *Nucl. Instrum. Methods Phys. Res. A*, 840:77–86, December 2016. doi:10.1016/j.nima.2016.10.003.

[44] N. Marsic, H. De Gersem, et al. Analytical and numerical performance analysis of a cryogenic current comparator. In *Proc. 8th Int. Part. Acc. Conf. (IPAC2017), Copenhagen, Denmark*, May . doi:10.18429/JACoW-IPAC2017-MOPAB037.

[45] V. Tympel, J. Golm, et al. The next generation of cryogenic current comparators for beam monitoring. In *Proc. 5th Int. Beam Instr. Conf. (IBIC'16), Barcelona, Spain*, pages 441–444, 2016. doi:10.18429/JACOW-IBIC2016-TUPG43.

[46] V. Tympel et al. Comparative Measurement and Characterisation of Three Cryogenic Current Comparators Based on Low-Temperature Superconductors. In *Proc. 7th Int. Beam Instr. Conf. (IBIC'18), Shanghai, China*, pages 126–129, January 2018. doi:10.18429/JACoW-IBIC2018-MOPC06.

[47] N. Marsic. Calculations for alternative shielding geometries/materials. BMBF collaboration meeting, April 2017.

[48] V. Tympel. Internal notes. 2018–2021.

[49] D. Drung, M. Götz, et al. Improving the stability of cryogenic current comparator setups. *Supercond. Sci. Technol.*, 22:114004, October 2009. doi:10.1088/0953-2048/22/11/114004.

[50] F. Ucar. Analysis and compensation of mechanical and magentic interference on the cryogenic current comparator (CCC). Master's thesis, TU Darmstadt, November 2020.

[51] V.P. Koshelets, A.N. Matlashov, et al. DC SQUID preamplifier for DC-SQUID magnetometer. *IEEE Trans. Magn.*, 25(2):1182–1185, March 1989. doi:10.1109/20.92501.

[52] T. Schönau, M. Schmelz, et al. SQUID-based setup for the absolute measurement of the Earth's magnetic field. *Supercond. Sci. Technol.*, 26(3): 035013, January 2013. doi:10.1088/0953-2048/26/3/035013.

[53] A. Kade, G. Trommler, et al. Final design review - cryostat for the cryogenic current comparator at CRYRING / FAIR. Technical report, Institute of Air Handling and Refrigeration gGmbH (ILK), March 2019.

[54] G. Chanin and J.P. Torre. Critical-field curve of superconducting lead. *Phys. Rev. B*, 5(11):4357–4364, June 1972. doi:10.1103/physrevb.5.4357.

[55] S. Casalbuoni, E.A. Knabbe, et al. Surface superconductivity in niobium for superconducting RF cavities. *Nucl. Instrum. Methods Phys. Res. A*, 538 (1-3):45–64, February 2005. doi:10.1016/j.nima.2004.09.003.

[56] J.W. Ekin. *Experimental Techniques for Low-Temperature Measurements: Cryostat Design, Material Properties and Superconductor Critical-Current Testing*. Oxford University Press, 2006. ISBN 9780198570547. doi:10.1093/acprof:oso/9780198570547.001.0001.

[57] C.H. Schroeder. Entwicklung eines Kryostaten für LHe-Temperatur zum Einbau eines supraleitenden Strahltransformators mit SQUID. Master's thesis, Fachhochschule Wiesbaden, January 1993.

[58] A. Lees, T. Koettig, et al. Design and optimisation of low heat load liquid helium cryostat to house Cryogenic Current Comparator in Antiproton Decelerator at CERN. *IOP Conf. Ser.: Mater. Sci. Eng.*, 171:012033, February 2017. doi:10.1088/1757-899x/171/1/012033.

[59] A. Lees, T. Koettig, et al. Cryogenic upgrade of the low heat load liquid helium cryostat used to house the Cryogenic Current Comparator in the Antiproton Decelerator at CERN. *IOP Conf. Ser.: Mater. Sci. Eng.*, 278: 012193, December 2017. doi:10.1088/1757-899x/278/1/012193.

[60] A. Onufrena, T. Koettig, et al. Design of a compact mesh-based high-effectiveness counter-flow heat exchanger and its integration in remote cooling systems. *Int. J. Heat Mass Transf.*, 183:122107, February 2022. doi:10.1016/j.ijheatmasstransfer.2021.122107.

[61] N. Marsic, H. De Gersem, and W.F.O. Müller. Cryogenic Current Comparator: mechanical vibrations of the cryostat. Technical report, TU Darmstadt, 2019.

[62] P. Kowina, M. Freimuth, et al. Pre-amplifier impedance matching for cryogenic BPMs. In *Proc. 10th Europ. Workshop on Beam Diagn. and Instr. for Part. Acc. (DIPAC'10)*, pages 347–349, Hamburg, Germany, 2011.

[63] E. D. Marquardt, J. P. Le, and Ray Radebaugh. Cryogenic material properties database. In *Cryocoolers 11*, pages 681–687. Springer, Boston, USA, 2002. ISBN 978-0-306-46567-3. doi:10.1007/0-306-47112-4_84.

[64] D. Flammann. Kryomechanische Berechnung und Simulation der SIS100 Dipolmagnet-Aufhängung. Bachelor's thesis, Hochschule Rhein-Main, January 2010.

[65] V. Parma. Cryostat Design. In *CERN Accelerator School: Superconductivity for Accelerators*, pages 353–399, Erice, Italy, 2014. doi:10.5170/CERN-2014-005.353.

[66] D. B. Mann. The thermodynamic properties of helium from 3 to 300 K between 0.5 and 100 atmospheres. Technical Report 154, National Bureau of Standards, January 1962.

[67] H. Frey and R. A. Haefer. *Tieftemperaturtechnologie*. VDI-Verlag, Düsseldorf, 1981. ISBN 978-3184005030.

[68] J.G. Weisend, editor. *Handbook of cryogenic engineering*. Taylor & Francis Inc, 1998. ISBN 1560323329.

[69] J. Iivanainen, A.J. Mäkinen, et al. A general method for computing thermal magnetic noise arising from thin conducting objects. *J. Appl. Phys.*, 130 (4):043901, July 2021. doi:10.1063/5.0050371.

[70] R.H. Koch, V. Foglietti, et al. Effects of radio frequency radiation on the dc SQUID. *Appl. Phys. Lett.*, 65(1):100–102, July 1994. doi:10.1063/1.113046.

[71] K. Abrahamsson, G. Andler, et al. CRYRING — a synchrotron, cooler and storage ring. *Nucl. Instrum. Methods Phys. Res. B*, 79(1-4):269–272, June 1993. doi:10.1016/0168-583x(93)95341-2.

[72] M. Lestinsky, V. Andrianov, et al. Physics book: CRYRING@ESR. *The European Physical Journal Special Topics*, 225(5):797–882, September 2016. doi:10.1140/epjst/e2016-02643-6.

[73] H. Danared, A. Källberg, and A. Simonsson. CRYRING at the LSR at FLAIR. *Hyperfine Interactions*, 194(1-3):129–135, August 2009. doi:10.1007/s10751-009-0040-7.

[74] E. Widmann. Low-energy antiprotons physics and the FLAIR facility. *Phys Scripta*, 2015(T166):014074, November 2015. doi:10.1088/0031-8949/2015/t166/014074.